AN EXPERIMENTAL INVESTIGATION OF ASPECT RATIO AND INCIDENCE ANGLE EFFECTS ON THE MEAN WAKE OF A SURFACE-MOUNTED FINITE-HEIGHT SQUARE PRISM

A Thesis Submitted to the College of Graduate Studies and Research in Partial Fulfilment of the Requirements for the Degree of Master of Science in the Department of Mechanical Engineering,
University of Saskatchewan
Saskatoon, Saskatchewan, Canada

By

Sanjith Unnikrishnan

PERMISSION TO USE

I agree that the Libraries of the University of Saskatchewan can make this thesis available for inspection. Permission for copying of this thesis in any manner, in whole or in part, for scholarly purposes may be granted by my supervisor, Prof. D. Sumner, the Head of the Department of Mechanical Engineering, or the Dean of the College of Graduate Studies and Research. It is understood that any copying or publication or use of this thesis, or parts thereof, for financial gain is prohibited without my written permission. Proper recognition shall be given to me and to the University of Saskatchewan in any scholarly use which may be made of any material in my thesis.

Requests for permission to copy or to make other use of material in this thesis, in whole or part, should be addressed to:

Head of the Department Mechanical Engineering
University of Saskatchewan
57 Campus Drive
Saskatoon, Saskatchewan, S7N 5A9
Canada

ABSTRACT

The flow around two-dimensional or infinite square prisms has been extensively studied. Fewer published studies have been carried out for the flow around surface-mounted finite-height square prisms, especially where the prism is oriented at a non-zero incidence angle. In the present study, the flow around surface-mounted finite-height square prisms of aspect ratios AR = 9, 7 and 5 was studied experimentally for a range of incidence angles, from $\alpha = 0°$ to 45°. The experiments were conducted in a low-speed wind tunnel at a Reynolds number of $Re = 3.7\times10^4$ and with a boundary layer thickness, relative to the prism width, of $\delta/D = 1.5$. Time-averaged velocity measurements in the wake were made using a seven-hole pressure probe. The wake measurements were carried out in two vertical planes, one parallel to the approach flow, and one normal to the approach flow. The data obtained were compared with previous results obtained for finite square prisms and finite cylinders.

For all aspect ratios, a symmetric counter-rotating pair of streamwise vortices representing the tip vortices is seen in the upper part of the wake at $x/D = 10$ for the orientation of $\alpha = 0°$. Also, small streamwise vorticity concentrations are seen at the outer edge of the wake close to the ground plane representing the horseshoe vortices. The base vortex structures were nearly absent for the square prism. The maximum length of the recirculation zone for a finite square prism is much higher than that of a finite cylinder. With an increase in aspect ratio from AR = 5 to AR = 9, at $\alpha = 0°$, the maximum length of the mean recirculation zone and the maximum downwash velocity increase. On the other hand, the width of the wake and the minimum value of the streamwise velocity component decrease with an increase in aspect ratio.

As α is varied from 0° to 45°, the mean wake shifts sideways in the direction of rotation of the prism, with the counterclockwise tip vortex moving higher above the ground plane and the clockwise tip vortex moving closer to the ground plane. The asymmetry in the wake is most pronounced at the critical incidence angle, which was between $\alpha = 10°$ and 15° in the experiments. The critical incidence angle corresponds to the smallest magnitude of the mean downwash velocity component, the largest value of the minimum mean streamwise velocity component, the maximum value of positive (counterclockwise) mean streamwise vorticity within the wake, and the minimum length of the mean recirculation zone. These properties of the wake were generally consistent for all three aspect ratios.

ACKNOWLEDGMENTS

First and foremost I wish to thank my supervisor, Prof. David Sumner. He has been supportive since the days I started my Master's degree. Thank you for giving me this research opportunity. The technical assistance of Mr. Dave Deustcher, Mr. Shawn Reinink and Engineering Shops are well acknowledged and appreciated. Many thanks to my advisory committee members, Prof. J.D. Bugg and Prof. D.J. Bergstrom, for their positive criticisms, useful comments and suggestions that helped improve my research. I want to acknowledge the support and encouragement received from my sister, Mom and Dad, and my friends that helped me in many ways to make my Master's program a success. Financial support in the form of a Research Assistantship from Prof. Sumner is acknowledged and appreciated. Finally, to Him who is able to do far more abundantly beyond all that we ask or think, according to the power that works within us, to Him be the glory forever and ever.

DEDICATION

Every challenging work needs self-efforts as well as guidance of elders especially those who are close to our heart.

My humble effort is dedicated to my sweet and loving

Father, **Mr. Sreedharan Unnikrishnan**

Mother, **Mrs. Anithakumari Unnikrishnan**
And
Sister, **Mrs. Soumya Binoy**

Whose affection, love, encouragement and prays of days and night make me able to get such success and honour,

Along with the Almighty God, for the strength and Knowledge he gave me for my research.

TABLE OF CONTENTS

NOMENCLATURE

English Symbols

AR	aspect ratio
C_D	mean drag force coefficient
C_L	mean lift force coefficient
D	width of the prism [mm]
d	projected width of prism [mm]
F_D	mean drag force [N]
F_L	mean lift force [N]
f	vortex shedding frequency [Hz]
H	height of the prism [mm] or boundary layer shape factor
L_{max}	maximum length of the mean recirculation zone [mm]
P_0	stagnation pressure [Pa]
P_∞	freestream static pressure [kPa]
q_∞	freestream dynamic pressure [Pa]
R	gas constant for air [J/(kg·K)]
Re	Reynolds number based on the width of the prism
Re_d	Reynolds number based on the projected width of the prism
St	Strouhal number
St_d	Strouhal number based on the projected width of the prism
St_w	Strouhal number based on prism width w
$St_{w'}$	Strouhal number based on wake width w'
T_∞	freestream temperature [°C]
U_∞	freestream velocity [m/s]
u	streamwise mean velocity component [m/s]
v	cross-stream mean velocity component [m/s]
w	wall-normal mean velocity component [m/s]
w'	wake width [mm]
x	streamwise coordinate [mm]
y	cross-stream coordinate [mm]

z wall-normal coordinate [mm]

Greek Symbols

α incidence angle [°]

δ boundary layer thickness [mm]

θ momentum thickness [mm]

μ_∞ freestream dynamic viscosity [$N \cdot s/m^2$]

ν_∞ freestream kinematic viscosity [m^2/s]

ρ_∞ freestream fluid density [kg/m^3]

ω_x mean streamwise vorticity component [s^{-1}]

CHAPTER 1. INTRODUCTION

1.1 Bluff-Body Aerodynamics

A body placed in a fluid flow experiences a drag force, which has two primary components: skin-friction drag and pressure drag. Skin-friction drag is formed as a result of friction between the fluid and the body. This results in the formation of boundary layers on the solid surfaces of the body. Skin-friction drag is strongly dependent on the Reynolds number. Skin-friction drag is important for attached flows or where no flow separation occurs and is a function of the surface area exposed to the flow. An aerofoil at low angle of attack is a good example of a streamlined body where the majority of the total drag force is contributed by the skin-friction drag. Pressure drag arises as a result of the pressure difference between the upstream and downstream sections of the body. It results in the formation of a wake downstream of the body and is usually less sensitive to Reynolds number compared to the skin-friction drag. Pressure drag is important for bodies associated with flow separation, such as bluff bodies, and is a function of the cross-sectional (frontal) area of the body. Examples of simple bluff-body shapes include cylinders, prisms, spheres, and flat plates normal to the approaching flow. At high Reynolds numbers, these bodies experience drag which is dominated by the pressure drag contribution. Figure 1.1 shows a schematic of flow around a streamlined body and a bluff body.

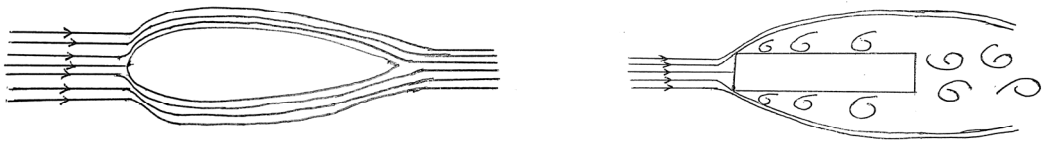

(a) (b)

Figure 1.1: Schematic of flow around a (a) streamlined body (aerofoil) and (b) bluff body (rectangular prism).

Apart from aerospace applications and a majority of transport vehicles, many of the fixed structures found in engineering applications are bluff bodies. Some of the engineering applications of bluff bodies include buildings, bridges, chimneys, cooling towers, underwater structures, oil storage tanks, etc. Thus, bluff body aerodynamics is an important research area in the field of wind engineering.

The flow around simple, two-dimensional bluff bodies, such as slender cylinders (a cylinder is a body with a circular cross-section) and square prisms (a square prism is a body with a square cross-section), has received much attention in the engineering literature. These slender bodies are often referred to as "infinite" cylinders and prisms since the body span is much greater than the width, and the effects of the ends of the body are minimal, allowing the flow to be considered two-dimensional. However, in many of the engineering applications involving bluff bodies, the body is of finite height and flow around the ends of the body strongly influences the overall flow field. The resulting flow field is three-dimensional. Flow around surface-mounted, finite-height bluff bodies, such as finite cylinders and finite square prisms, is more relevant to many engineering applications, such as the flow around buildings, chimneys, cooling towers, oil storage tanks, and electronic components on circuit boards. Despite its relevance to these applications, however, the flow around surface-mounted, finite-height bluff bodies has been less extensively studied compared to the flow around two-dimensional, "infinite" cylinders and prisms.

In the present thesis research, the flow around a surface-mounted, finite-height square prism is investigated; a schematic is shown Figure 1.2. The flow field is influenced by many parameters such as the prism's aspect ratio (AR = H/D, where H is the height of the prism and D is its width), incidence angle (α), Reynolds number (Re), and the relative thickness of the boundary layer on the surface or ground plane (δ/D). Here, the Reynolds number is based on the width of the prism, and is defined as $\mathrm{Re} = U_\infty D/\nu_\infty$, where U_∞ is the freestream velocity outside the boundary layer on the ground plane and ν_∞ is freestream kinematic viscosity. Few published studies of the flow around surface-mounted finite-height square prisms have systematically examined the effects of AR and α, and the present thesis research aims to address this gap in the literature. One recent but very preliminary study on the finite square prism by Ogunremi and Sumner (2015a) focused on the effects of incidence angle on the wake of a finite square prism of AR = 3, and the present thesis research may be considered a continuation or extension of this study, but for prisms of higher aspect ratio.

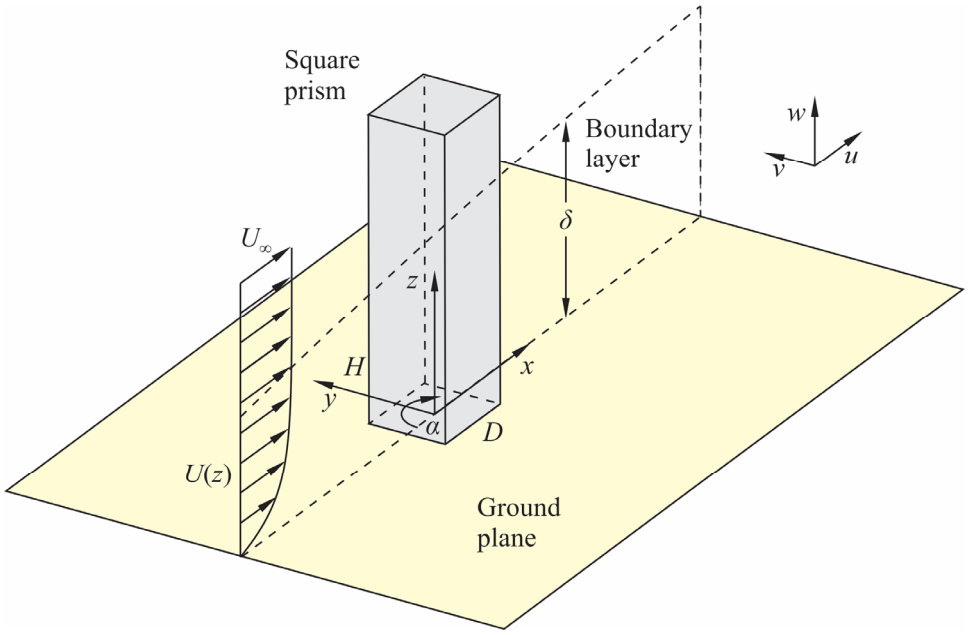

Figure 1.2: Schematic of flow around a surface-mounted, finite-height square prism, which is the subject of the present thesis research, where *x* is the streamwise coordinate direction, *y* is the cross-stream coordinate direction, *z* is the wall-normal (vertical) coordinate direction, *u* is the streamwise velocity component, *v* is the cross-stream velocity component, *w* is the wall-normal (vertical) velocity component, and *U*(*z*) is the mean velocity profile of the boundary layer. Figure created by D. Sumner (used with permission).

1.2 Objectives

The thesis research is focused on an experimental study of the flow around surface-mounted, finite-height square prisms. Of particular interest is the mean wake of the finite prism and how it is influenced by changes in incidence angle (α) and aspect ratio (AR). Wind tunnel experiments were conducted at Re = 3.7×10^4 for finite square prisms of AR = 9, 7, and 5 and for incidence angles ranging from α = 0° to 45°. These aspect ratios were chosen to ensure that at least one prism was below the critical aspect ratio and to enable comparison with previous studies (Sumner et al., 2004; Rostamy et al., 2012; McClean and Sumner, 2014; Ogunremi and Sumner, 2015a,b). The main objectives of the research are the following:

1. To measure the mean velocity field in vertical planes (normal to and parallel to the main flow direction) in the wake of finite square prisms of aspect ratios AR = 9, 7 and 5 using a seven-hole pressure probe, for incidence angles from α = 0° to 45°;

2. Using the above measurements, to investigate the effects of incidence angle (α) and aspect ratio (AR) on the mean wake, including the mean recirculation zone and the mean streamwise vortex structures;
3. To compare the mean wake of a finite square prism with that of a finite cylinder, using finite-cylinder results from the literature; and
4. To identify the mean wake flow pattern associated with the critical incidence angle of the finite square prism.

1.3 Outline of the Thesis

The thesis is divided into six chapters. Chapter 2 gives a review of previous research and background information on the flow around infinite and finite square prisms. The apparatus, instrumentation and experimental conditions used for the present research are described in Chapter 3. Chapters 4 and 5 are devoted towards the results and discussion of the present research. Chapter 4 focuses on the aspect ratio effects for the flow around the finite square prism at zero incidence angle ($\alpha = 0°$). The incidence angle effects on the flow around finite square prisms, for $\alpha = 0°$ to 45°, are then discussed in Chapter 5. A summary along with conclusions and recommendations for future work, are presented in Chapter 6. Appendix A contains permissions from publishers to reproduce some figures in the thesis.

CHAPTER 2. LITERATURE REVIEW

2.1 Introduction

In this chapter, a brief review of the literature is presented. The chapter is divided into two main sections: Section 2.2 summarizes the literature for the flow around an infinite (two-dimensional) square prism, and Section 2.3 summarizes the literature for the flow around a surface-mounted finite-height square prism.

2.2 Flow Around an Infinite Square Prism

The flow around an infinite or two-dimensional square prism (Figure 2.1) is of considerable importance because of the occurrence of prism-like structures in engineering applications. The body can be considered "infinite" and the flow can be considered "two-dimensional" when the end effects of the square prism can be neglected, i.e., its span or height (H) greatly exceeds its width (D).

Even though flow past an infinite square prism resembles that of flow past an infinite cylinder in many respects, such as the occurrence of vortex shedding in the wake, the flow separation and properties such as lift coefficient, drag coefficient, wake size and Strouhal number (dimensionless vortex shedding frequency) differ from those of the cylinder. Unlike the cylinder, the square prism has fixed separation points at the leading edge corners or trailing edge corners, depending on the Reynolds number (Dutta et al., 2008). For an infinite square prism at zero-incidence angle ($\alpha = 0°$), separation occurs at the upstream corners for $\mathrm{Re} \geq 175$ but occurs at the downstream corners for $\mathrm{Re} \leq 100$ (Sohankar et al., 1997).

The majority of the past studies of the flow around an infinite square prism were focused on aerodynamic forces (lift and drag), vortex shedding frequencies, and the time-average and instantaneous wake (Huang et al., 2010). As a result of the fixed separation points at the front of the prism, the mean drag force coefficient, C_D ($= F_D/(q_\infty DH)$, where F_D is the mean drag force and q_∞ is the freestream dynamic pressure), is relatively insensitive to Reynolds number at zero incidence angle. Also, studies in the past have revealed that the prism's Strouhal number ($\mathrm{St} = fD/U_\infty$, where f is the vortex shedding frequency) is insensitive to Reynolds number ranging from

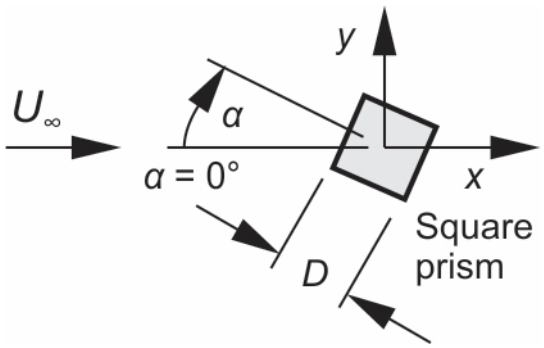

Figure 2.1: Schematic of the flow around a two-dimensional (infinite) square prism of side length or width, D, where x is the streamwise coordinate direction, y is the cross-stream coordinate direction, α is the incidence angle, and U_∞ is the freestream velocity. Figure created by D. Sumner (used with permission).

Re = 10^4 to 10^5 (McClean and Sumner, 2014). Figure 2.1 shows a schematic of flow over an infinite square prism where D is side length or width of the prism and α is the incidence angle.

As the prism is rotated there is a change in the projected dimension normal to the flow and the relative positions of the four corner edges of the prism. The resulting changes in flow behaviour with incidence include the shear layer differences originating from the two sides of the prism, the chance of reattachment of flow on the lower side of the prism and changes in the wake width, vortex formation length, and location of shear layer rollup (McClean and Sumner, 2014). These changes can be analyzed by measuring the mean aerodynamic forces, expressed as the mean drag coefficient, C_D, and the mean lift coefficient, C_L (defined similar to C_D), and the Strouhal number, St. Thus, the wake of a square prism is highly sensitive to its orientation with respect to the incoming flow.

In the literature, the majority of the experiments were carried out for flow around an infinite square prism at $\alpha = 0°$, where one of the faces of the prism is normal to the approaching flow. Some researchers have focused on the effects of incidence angle for infinite square prisms for incidence angles ranging from $\alpha = 0°$ to 45°. Within this range of angles, there exists a "critical incidence angle" at which minimum wake width occurs (Huang et al., 2010). The critical incidence angle also coincides with the minimum value of C_D, the maximum negative value of C_L (from Figure 2.1, negative values of the lift force are in the $-y$ direction), and the maximum value of St. The critical incidence angle lies between $\alpha = 10°$ and 30° depending on the experimental conditions (McClean and Sumner, 2014).

There have been several important experimental and numerical studies of the flow around an infinite square prism that have looked at incidence angle effects, and some of these studies are summarized below.

Obasaju (1979) studied the flow around a square prism for $\alpha = 0°$ to 45° at Re = 1×10^4 and identified a critical incidence angle of $\alpha = 13.5°$ where the maximum St occurred. Igarashi (1984) studied the flow characteristics over a larger range of Reynolds numbers, from Re = 3.85×10^3 to 7.7×10^4, and classified the flow patterns into four regimes based on the prism orientation; these flow patterns are presented later in Chapter 2. Norberg (1993) studied flow around square and rectangular prisms at incidence over an even wider range of Reynolds number, from Re = 400 to 3×10^4, using hot-wire anemometry to measure the vortex shedding frequencies. Sohankar et al. (1997) performed numerical simulations of flow past a square prism for low Reynolds numbers and a range of α, and identified the onset of vortex shedding occurs within a critical Reynolds number range of Re = 40 to 55. Dutta et al. (2003) studied the sensitivity of the wake behind a square prism for α = 0° to 45° for Re = 1,340, 4,990 and 9,980, using flow visualization experiments and through measurements of C_D, St and wake velocity fluctuations.

Lindquist and Vieira (2010) studied the relationship between St and α for α = 0° to 45°. Their experiments were conducted at relatively low Reynolds numbers compared to many other studies. Their work revealed that the maximum Strouhal number was obtained at a critical angle of incidence between 10° and 15° for a Reynolds number range between 100 and 1,000. Ozgoren (2006) studied the flow characteristics of a square prism using particle image velocimetry (PIV), also for relatively low Reynolds numbers, ranging between 550 to 3,400 for two orientations of α = 0° and 45°.

Dutta et al. (2008) investigated the flow around an infinite square prism experimentally using PIV, hot-wire anemometry and flow visualization at Re = 410 for different prism orientations ($\alpha = 0°$, 22.5°, 30° and 45°). Van Oudheusden et al. (2008) also used PIV to study the flow around a square prism at incidence, for α = 0°, 5°, 10° and 15° and Reynolds numbers of 4×10^3, 1×10^4 and 2×10^4.

Huang et al. (2010) studied the flow characteristics around a square prism and their influence on wake properties at Reynolds number between 3.9×10^4 and 9.4×10^4. The vortex shedding characteristics were measured by a single-wire hot-wire anemometer for Reynolds numbers between 5×10^3 and 1.2×10^5. A critical incidence angle of α = 15° was found to divide

the subcritical regime (i.e., for incidence angles below the critical incidence angle) and supercritical regime (i.e., for incidence angles above the critical incidence angle) with the occurrence of maximum Strouhal number. Yen and Yang (2012) investigated the effects of Reynolds number and incidence angle for the square prism flow fields at different turbulence intensities. The Reynolds number for their study ranged from 3×10^4 to 1×10^5. Flow fields were visualized using the surface oil flow visualization method.

2.2.1 Experimental and Numerical Approaches

Throughout the literature, researchers of the flow around an infinite square prism have used different techniques and instruments for their experiments. Vortex shedding frequencies have been recorded using hot-wire anemometry (e.g., Norberg (1993), Saha et al. (2000), Dutta et al. (2003), Hu et al. (2006), Dutta et al. (2008), Huang et al. (2010), Yen and Yang (2012)). Flow visualization techniques commonly used have included smoke visualization (e.g., Igarashi (1984), Dutta et al. (2003), Huang et al. (2010)), the surface oil flow technique (e.g., Huang et al. (2010), Yen and Yang (2012)), liquid dye injection (e.g., Lindquist and Vieira (2010)), laser-induced fluorescence (LIF) visualization (e.g., Luo et al. (2003)), PIV (e.g., van Oudheusden et al. (2005), Hu et al. (2006), Ozgoren (2006), Kurtulus et al. (2007), Dutta et al. (2008), van Oudheusden et al. (2008), Yen and Yang (2011)), and laser Doppler anemometry (LDA) (e.g., Lyn et al. (1995), Hu et al. (2006)). Numerical simulations of the flow around an infinite square prism have used direct numerical simulation (DNS) (e.g, Sau et al. (2003)) and large eddy simulation (LES) (e.g., Lee (1998), Oka and Ishihara (2009)).

2.2.2 Flow Visualization

To understand the nature of the flow field and vortex shedding characteristics, several researchers have carried out flow visualization experiments at different incidence angles for a variety of Reynolds numbers. Igarashi (1984) studied flow around an infinite square prism using a smoke wind tunnel at $Re = 1.1\times10^4$ for $\alpha = 0°$ to 45°. Similar studies were done by Huang et al. (2010) and Yen and Yang (2011). Dutta et al. (2004) visualized the wake of an infinite square prism at $Re = 275$ using a light sheet of a pulsed laser. Smoke visualization experiments carried out by Dutta et al. (2003) for higher Reynolds numbers showed similar flow separation patterns as that of lower Reynolds number flow. Huang et al. (2010) employed both smoke wire and surface

oil flow visualization to visualize both instantaneous and time-averaged flow patterns at Re = 2×10^4. In their study, the smoke-wire flow visualization technique was employed to visualize "instantaneous" flow patterns, while the surface-oil flow visualization method was used to study the time-averaged flow behaviour close to surface of the square prism.

Lindquist and Vieira (2010) carried out flow visualization experiments for an infinite square prism for a Reynolds numbers up to 1000 for $\alpha = 0°$ to 45°. A liquid dye injection flow visualization technique was employed. The mechanism of shear layer detachment and reattachment was clearly observed in their flow visualization images. At $\alpha = 0°$, the boundary layers detach from either side of the leading edges forming the von Kármán vortex street. As the incidence angle becomes greater than 0°, the left shear boundary layer detachment occurs at the trailing edge of the square prism, thereby changing the wake structure. It was observed that at an angle of $\alpha = 12.5°$, the wake width shows minimum value. The two shear layers strongly interact with each other due to the smaller wake width, which results in high vortex shedding frequency. This angle, of $\alpha = 12.5°$, corresponds to the critical incidence angle.

2.2.3 Mean Flow Patterns

From the flow visualization experiments carried out in the past, researchers proposed various flow patterns for the flow over an infinite square prism. Basically the flow patterns for an infinite square prism are classified into two overall types based on the prism orientation: perfect separation type and reattachment flow, where the boundary between the two flow patterns is the critical incidence angle. From the flow visualization experiments done by Igarashi (1984), four main flow patterns based on the incidence angle were identified (Figure 2.2), for Reynolds numbers ranging from Re = 3.85×10^3 to 7.7×10^4:

1. The "perfect separation (symmetric)" flow pattern at low incidence angles ($0° \leq \alpha \leq 5°$) (Figure 2.2a);
2. The "perfect separation type (asymmetric)" at incidence angles up to the critical incidence angle ($5° \leq \alpha \leq 13°$) (Figure 2.2b);
3. The "reattachment flow type" flow pattern for incidence angles ranging from 14° to $15° \leq \alpha \leq 35°$ (Figure 2.2c); and
4. The "wedge flow type" flow pattern at high incidence angles ($35° \leq \alpha \leq 45°$) (Figure 2.2d).

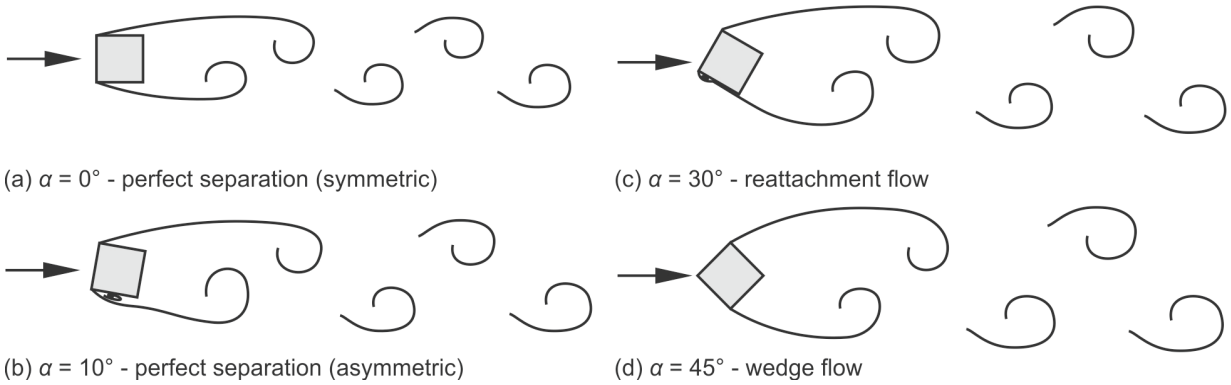

Figure 2.2: Examples of the main flow patterns for an infinite square prism: (a) "perfect separation (symmetric)" flow pattern (b) "perfect separation type (asymmetric)" flow pattern (c) "reattachment flow type" flow pattern (d) "wedge flow type" flow pattern. Figure created by D. Sumner (used with permission).

Mean streamline patterns from the numerical study by Oka and Ishihara (2009) for flow around an infinite square prism are shown in Figure 2.3. A perfect separation (symmetric) type flow is observed at $\alpha = 0°$ (Figure 2.3a) with no flow reattachment. Two large vortices are formed in the wake. At $\alpha = 14°$ (Figure 2.3b), reattachment of separated flow occurs at the lower face trailing edge of the square prism. A single large vortex is formed. The reattachment of the flow is more clear at $\alpha = 20°$ (Figure 2.3c) with the formation of a single large vortex in the wake region. The separation bubble area becomes smaller compared to that at $\alpha = 14°$. The wedge flow type pattern is seen at $\alpha = 45°$ (Figure 2.3d).

Huang et al. (2010) classified the flow topology (streamline patterns) into three regimes: the subcritical, supercritical and wedge flow as shown in Figure 2.4. The subcritical flow lies between $0° \leq \alpha \leq 15°$ where the boundary layer separates from the leading edge of the prism and does not reattach to the surface. There exist small "dual-ring bubbles" on the separated boundary layer region on the leading edges of the lateral faces. The reattachment of the separated boundary layer occurs in the supercritical regime which lies between $15° \leq \alpha \leq 45°$ with the formation of a recirculation bubble. The separated boundary layer on the lateral surface never reattaches to the surface and forms a wide recirculation bubble on the rear part of the surface. A symmetric wedge flow is observed for an incidence angle of 45° on both surfaces on the prism.

Yen and Yang (2012) classified the boundary layer flow modes by varying Re, α, and the turbulence intensity. At low turbulence intensity, α contributes the major factor to control

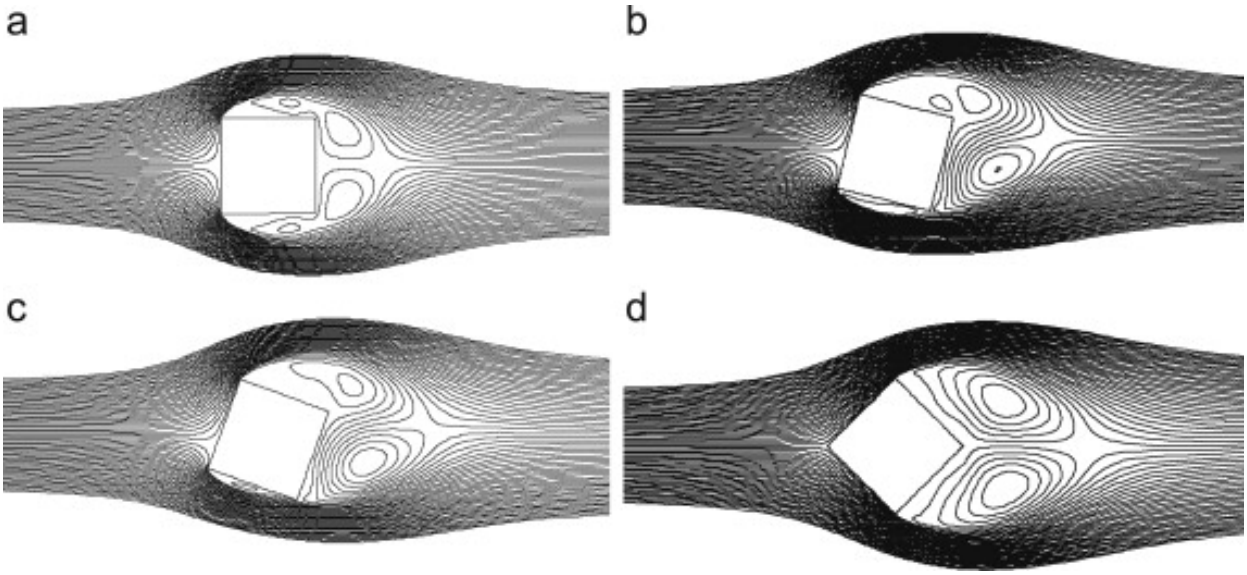

Figure 2.3: Variation of mean streamlines with angles of attack, from Oka and Ishihara (2009): (a) $\alpha = 0°$; (b) $\alpha = 14°$; (c) $\alpha = 20°$; (d) $\alpha = 45°$. Reprinted from Journal of Wind Engineering and Industrial Aerodynamics, Vol. 97, Oka, S. and Ishihara, T., Numerical study of aerodynamic characteristics of a square prism in a uniform flow, pp. 548-559, 2009, with permission from Elsevier.

boundary layer flow modes when α lies between 0° and 60°. The separation bubble mode lies in the range $0° \leq \alpha \leq 23°$; the separation mode lies in the range $23° \leq \alpha \leq 34°$; the leading edge separation mode exists for $34° \leq \alpha \leq 43°$, and the boundary layer attached mode exists for $\alpha \geq 43°$. When the turbulence intensity was increased to 0.70% and 0.78%, five boundary layer flow modes (instead of four) were obtained: "leading-edge bubble, separation bubble, separation, leading-edge separation, and boundary layer attached" (Yen and Yang, 2012).

2.2.4 Mean Lift Force Coefficient

The mean lift coefficient strongly depends on the prism's orientation (Figure 2.5). The mean lift coefficient is zero when the prism is at $\alpha = 0°$ but becomes negative (in the $-y$ direction, see Figure 2.1) with an increase in incidence angle. It reaches a minimum value (most negative value) at around $\alpha = 12.5°$ (depending on the study) which corresponds to the critical incidence angle. The minimum (most negative) lift coefficient occurs in the separation bubble mode (Yen and Yang, 2012). On further increasing the incidence angle, the lift coefficient increases (becomes less negative) and becomes positive at around $\alpha = 27.5°$; it remains positive until $\alpha = 45°$ when it

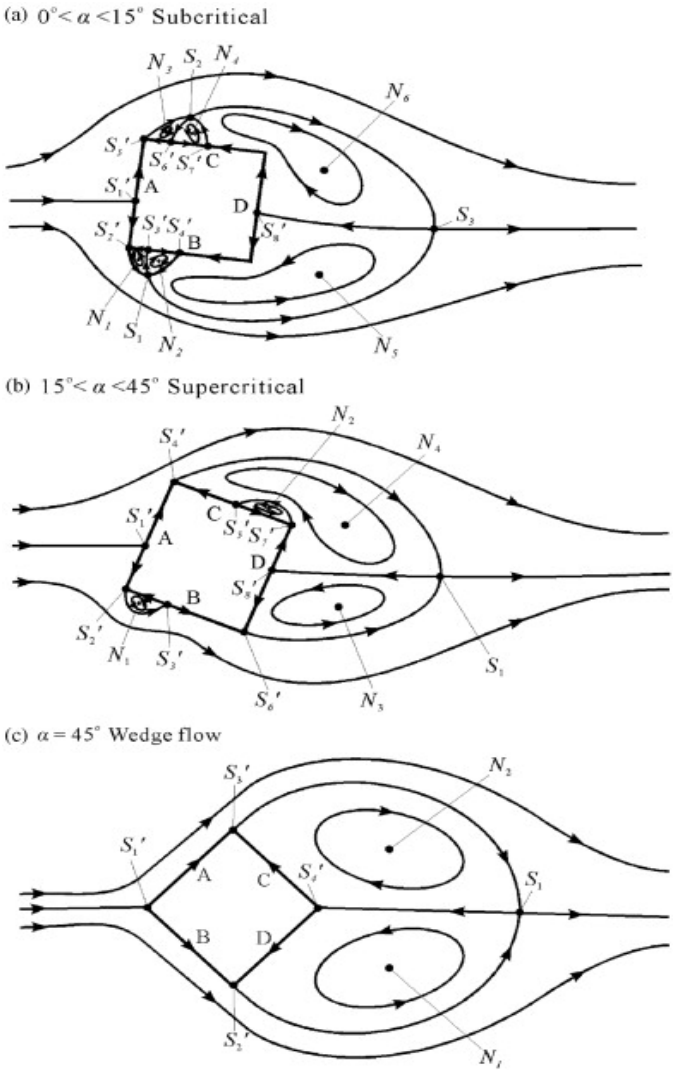

Figure 2.4: Two-dimensional topological flow patterns around an infinite square prism, from Huang et al. (2010). Reprinted from Journal of Fluids and Structures, Vol. 26, Huang, R.F., Lin, B.H., and Yen, S.C., Time-averaged topological flow patterns and their influence on vortex shedding of a square cylinder in crossflow at incidence, pp. 406-429, 2010, with permission from Elsevier.

returns to the zero lift value. This α region corresponds to the attached mode (McClean and Sumner, 2014).

2.2.5 Mean Drag Force Coefficient

Saha et al. (2000) reported the near constancy of the mean drag coefficient, C_D, with Reynolds number at zero incidence angle. This is because of the fixed separation points at the sharp corners of the square prism. Dutta et al. (2003) carried out time-averaged drag coefficient

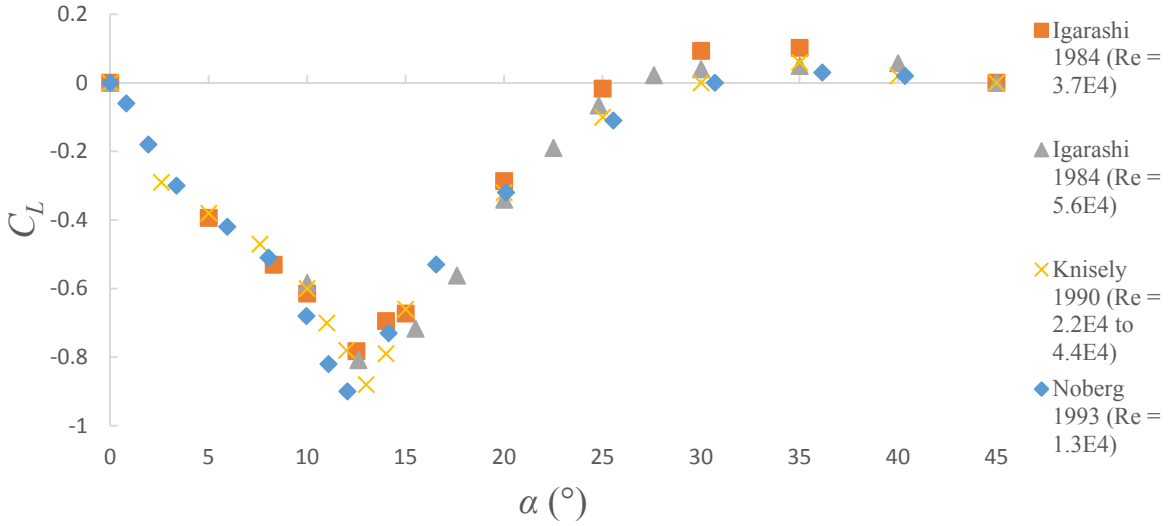

Figure 2.5: Variation of the mean lift coefficient against incidence angle for an infinite square prism.

measurements for an infinite square prism for three Reynolds numbers (1,340, 4,990 and 9,980). The drag coefficients obtained for the highest Reynolds number (Re = 9,980) and lowest Reynolds number (Re = 1,340) were C_D = 2.21 and 2.27, illustrating the high value of drag coefficient for the square prism compared to a cylinder.

The behaviour of the mean drag coefficient with incidence angle is shown in Figure 2.6. With an increase in incidence angle, the drag coefficient drops to a minimum value of C_D = 1.4 at around α = 13° which is around the critical incidence angle for Re = 5.6×10^4. After α = 15°, there is an increase in drag coefficient with α; it reaches the maximum value of C_D = 2.7 at the 45° configuration for Re = 5.6×10^4.

2.2.6 Strouhal Number

The vortex shedding frequency in the wake behind a square prism is normalized to give a non-dimensional parameter known as Strouhal number (St). Numerous experiments and numerical simulations have been carried out in the past on flow over an infinite square prism to study the effects of α and Re on the Strouhal number. Some correlations between Strouhal number and incidence angle as well as Strouhal number and Reynolds number are shown in Figures 2.7 and 2.8.

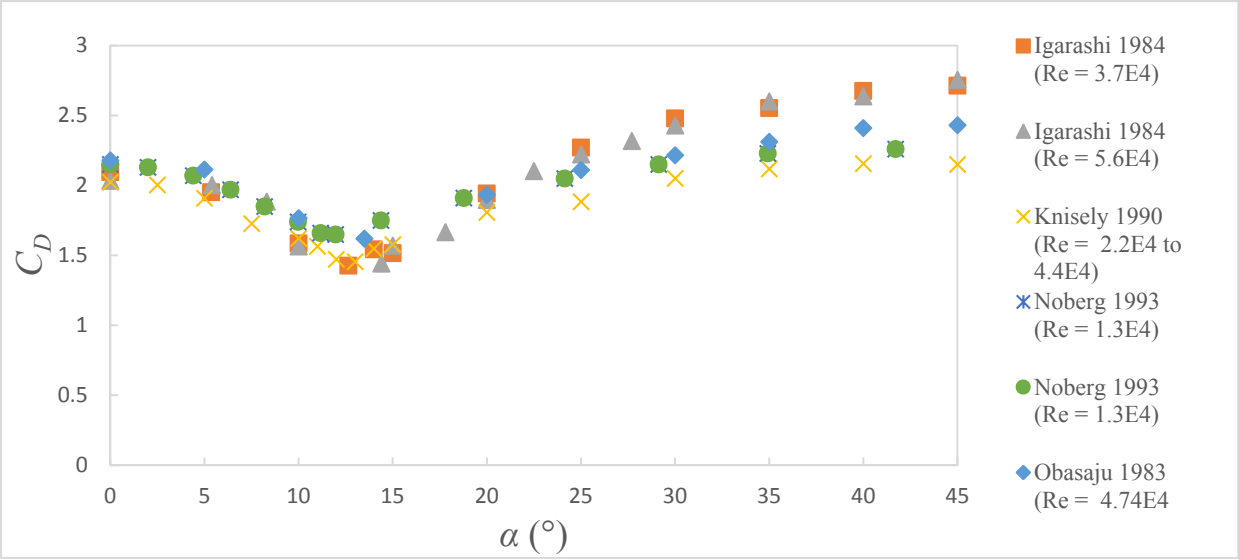

Figure 2.6: Variation of the mean drag coefficient against incidence angle for an infinite square prism.

In Figure 2.7, the projected width d of the square prism was used as a length scale for the Strouhal number (St_d). Figure 2.7a shows that St_d increases with an increase in α from $St_d = 0.13$ at $\alpha = 0°$ to a maximum value of $St_d = 0.2$ at $\alpha = 15°$ then decreases a little bit and gradually goes to $St_d = 0.18$ for $\alpha = 30°$ to 45°. The results in Figure 2.7a show that the Strouhal number attains a local maximum at the critical incidence angle (Huang et al., 2010), with a small Reynolds number sensitivity (Figure 2.7b). In Figure 2.8, where St is made dimensionless with the width of the prism, D, the critical incidence angle for the maximum St occurs near $\alpha = 15°$. The data in Figures 2.7 and 2.8 are for Reynolds numbers of the order of 10^4.

Sohankar et al. (1997) carried out numerical simulations on flow around an infinite-square prism to study the effects of incidence angle on the Strouhal number at low Reynolds numbers ($Re \leq 200$). It was observed that as the incidence angle is increased from $\alpha = 0°$, there is an increase in Strouhal number. At a critical incidence angle between $\alpha = 6°$ and 10°, the St value reached its maximum. The critical incidence angle range for their work was much lower than reported elsewhere (such as for higher Re, as shown in Figures 2.7 and 2.8). This can suggest a possible Reynolds number dependence on the critical incidence angle for low Reynolds number range flows.

Dutta et al. (2004) carried out an experimental analysis under a similar low Reynolds number range ($Re \leq 200$) and compared their results with the work of Sohankar et al. (1997). They

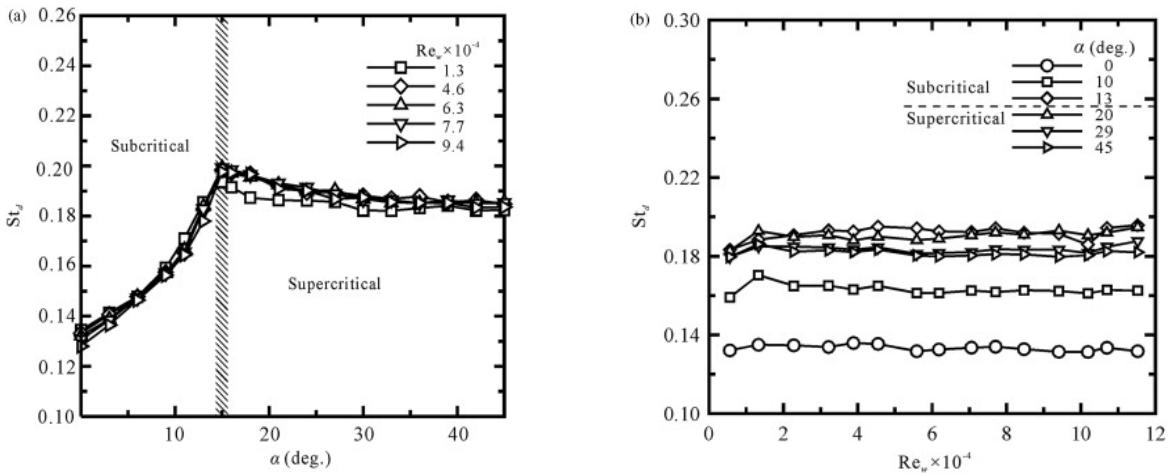

Figure 2.7: Strouhal number based on the projected width (d) of the infinite square prism (St_d), from Huang et al. (2010): (a) variation with incidence angle, (b) variation with Reynolds number based on the width (D) (designated as Re_w above). Reprinted from Journal of Fluids and Structures, Vol. 26, Huang, R.F., Lin, B.H., and Yen, S.C., Time-averaged topological flow patterns and their influence on vortex shedding of a square cylinder in crossflow at incidence, pp. 406-429, 2010, with permission from Elsevier.

identified a critical incidence angle of α = 22.5°, which was much higher than the low Re simulation results of Sohankar et al. (1997) and the high Re experimental results shown in Figures 2.7 and 2.8. The Strouhal number obtained at low Reynolds number (Re ≤ 200) was in the range of St = 0.126 to 0.154 and at higher Reynolds number in the range of St = 0.141 to 0.143. Dutta et al. (2008) also investigated the flow around an infinite square prism using PIV for two aspect ratios (AR = 16 and 28) at Re = 410. A similar trend in Strouhal number data was obtained with the maximum St at α = 22.5°. These low Re simulations and experiments suggest a Re dependence for the critical incidence angle.

The Strouhal number variation with increase in incidence angle is related to an increase in the projected dimension of the cylinder with respect to incoming flow. The width between the two shear layers directly influences the vortex shedding frequency. Therefore an increase in incidence angle increases the distance between the two free shear layers and results in reduced interaction between them resulting in a drop in Strouhal number. This happens when α is beyond the critical incidence angle. Also, there is a possibility that the separating shear layer from one side draws the neighbouring vortex from the opposite shear towards it, leading to an increase in Strouhal number. Thus a maximum St value occurs at a critical incidence angle due to the combined effect of

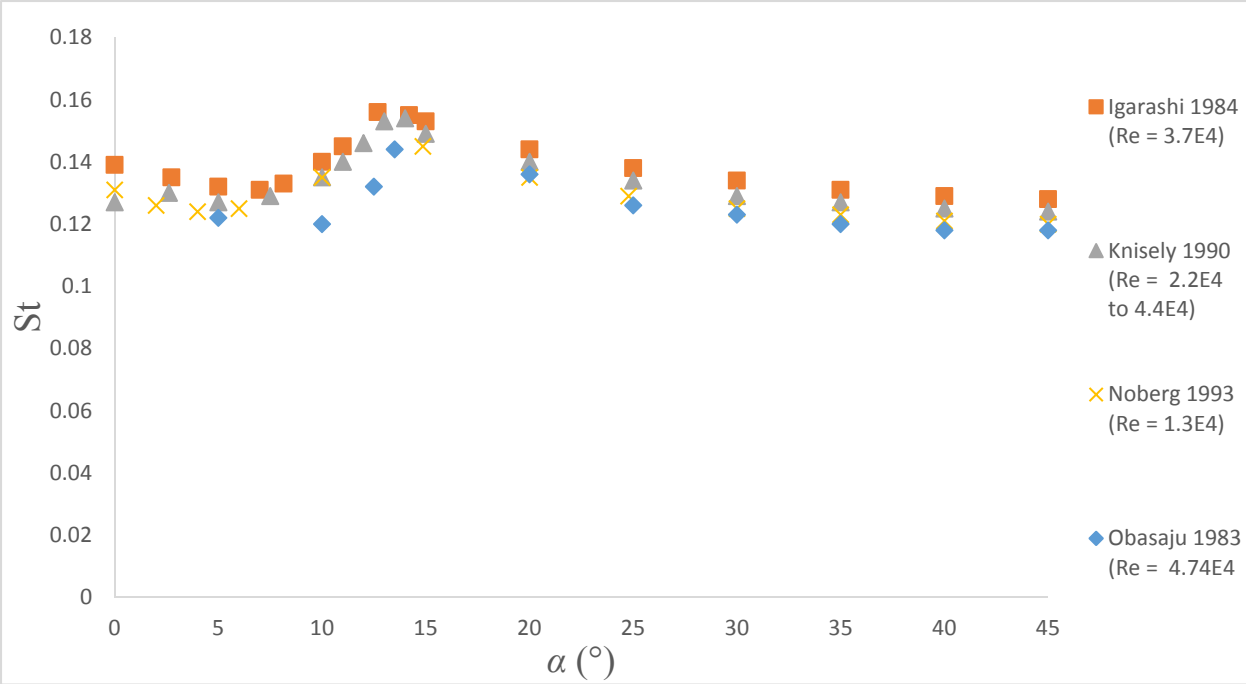

Figure 2.8: Variation of the Strouhal number against incidence angle for an infinite square prism.

increased projected dimension and shorter vortex rollup distance (Dutta et al., 2008). It is noted that the variation in Strouhal number data from one experiment to another is greater compared to the variation in the drag coefficient data.

2.3 Flow Around a Finite Square Prism

There are fewer studies in the literature on the flow over a surface-mounted finite-height square prism compared to an infinite square prism. The flow around a finite square prism depends on many factors such as AR, α, δ/D, and Re. A schematic of the flow field was presented earlier in Figure 1.2.

One of the earliest studies of flow over sharp-edged finite-height bluff bodies was done by Baines (1963). His study was focused on the pressure distribution and wind loads acting on buildings, including a finite square prism of AR = 8. He clearly identified the flow patterns on these bodies from pressure distribution data.

Sarode et al. (1981), Sakamoto and Arie (1983), Sakamoto and Oiwake (1984), Sakamoto (1985), Sattari et al. (2010), and McClean and Sumner (2014) focused on the study of aspect ratio effects on the forces and vortex shedding for a finite square prism. The aspect ratio of the square prism ranged from AR = 0.5 to 11 in these studies.

Rostamy et al. (2012) carried out PIV velocity field measurements for square prisms of AR = 3, 5, 7 and 9. Their study was focused on the end effects of the square prism on the mean flow pattern. Other PIV studies were conducted by Wang and Zhou (2009), who proposed a three-dimensional flow model for a finite square prism (based on prisms of AR = 3 to 7), which was distinct from previously proposed models, and Bourgeois et al. (2011), who studied the phase-averaged vortex structures in the wake of a finite-height square prism of AR = 4.

Boundary layer thickness (δ/D) effects were studied by Sakamoto and Arie (1983), Sakamoto and Oiwake (1984) and Sakamoto (1985), but were limited to lower aspect ratios (AR = 1 to 5). Sakamoto (1985) measured mean aerodynamic force coefficients and Strouhal numbers for prisms of AR = 1 to 5 at Re = 3.3×10^4 to 1.65×10^5. The incidence angle was varied from α = 0° to 45° with an increment of 2.5°.

Most of the studies of a finite square prism have been focused on an incidence angle of α = 0°. The few studies which have considered the effects of incidence angle include work done by Sarode et al. (1981), Sakamoto (1985), McClean and Sumner (2014) and Ogunremi and Sumner (2015a). Sarode et al. (1981) measured the mean aerodynamic force coefficients for a surface-mounted finite square prisms of AR = 1.14 to 10 at Re = 2.2×10^4. The incidence angle was varied from α = 0° to 45°. It was observed that aspect ratio and incidence angle have significant effects on the mean lift coefficient. The incidence angle effects on the mean drag coefficient were prominent for only high aspect ratio square prisms.

McClean and Sumner (2014) studied the mean aerodynamic forces and vortex shedding for finite square prisms of AR = 3, 5, 7, 9 and 11 at Re = 7.3×10^4. The relative boundary layer thickness on the ground plane was δ/D = 1.5 for an incidence angle ranging from α = 0° to 45°. The mean drag coefficient and Strouhal number for the finite prism were less sensitive to changes in incidence angle than that of infinite square prisms. The critical incidence angle, corresponding to minimum mean drag coefficient, minimum mean lift coefficient and maximum Strouhal number, was found to be in the range of α = 15° to 18°. The critical aspect ratio was found to be between AR = 3 and AR = 5. It was observed that the wake for prisms less than this critical aspect ratio showed an absence of, or significantly weakened, Kármán vortex shedding.

The recent study by Ogunremi and Sumner (2015a) focused on the wake region of a surface-mounted finite-height square prism of AR = 3 at Re = 3.7×10^4. The ratio of the boundary layer thickness on the ground plane to the width of the prism was δ/D = 1.5. The incidence angle

varied from $\alpha = 0°$ to 45°. In these experiments, a seven-hole pressure probe was used to measure the mean velocity and vorticity fields in the wake. A similar experimental set-up and measurement instrumentation will be used in the present thesis research project.

2.3.1 Experimental and Numerical Approaches

Throughout the literature, researchers have used different techniques and instruments for their study of the flow around surface-mounted finite-height square prisms. The experimental studies were carried out in a wind tunnel or water tunnel depending on the experimental requirements. Vortex shedding frequencies were recorded using hot-wire anemometry (e.g., Wang and Zhou (2009), McClean and Sumner (2014)). PIV has been used by Wang et al. (2006), Wang and Zhou (2009), Sattari et al. (2010, 2012), Bourgeois et al. (2011, 2012), Rostamy et al. (2012), Hosseini et al. (2013), and El Hassan et al. (2015). Numerical simulations of the flow include direct numerical simulation (DNS) (e.g., Sau et al. (2003)) and large eddy simulation (LES) (e.g., Einian et al. (2009, 2010, 2011).

2.3.2 Flow Visualization

To understand the nature of flow and vortex shedding characteristics, it is important to conduct flow visualization experiments under different flow conditions. Flow visualization experiments by Wang and Zhou (2009), carried out at heights of $z/D = 3.5$ and 1 (as measured from the ground plane) for a finite square prism of AR = 7 identified the formation of both antisymmetric and symmetrical spanwise vortices.

2.3.3 Mean Flow Structure

To understand the flow behavior of a finite square prism, it is often important to identify the mean velocity vectors and streamlines of flow in different planes. In the past, the measurements were taken in planes because of the limitations of making three-dimensional instantaneous measurements. Wang and Zhou (2009) carried out PIV measurements in multiple horizontal and vertical planes. Rostamy et al. (2012) carried out PIV velocity field measurements for square prisms of AR = 3, 5, 7 and 9. These experiments were carried out at a Reynolds number of $Re = 4.2\times10^4$ for three vertical planes parallel to the mean flow direction at $y/D = 0$. Ogunremi and

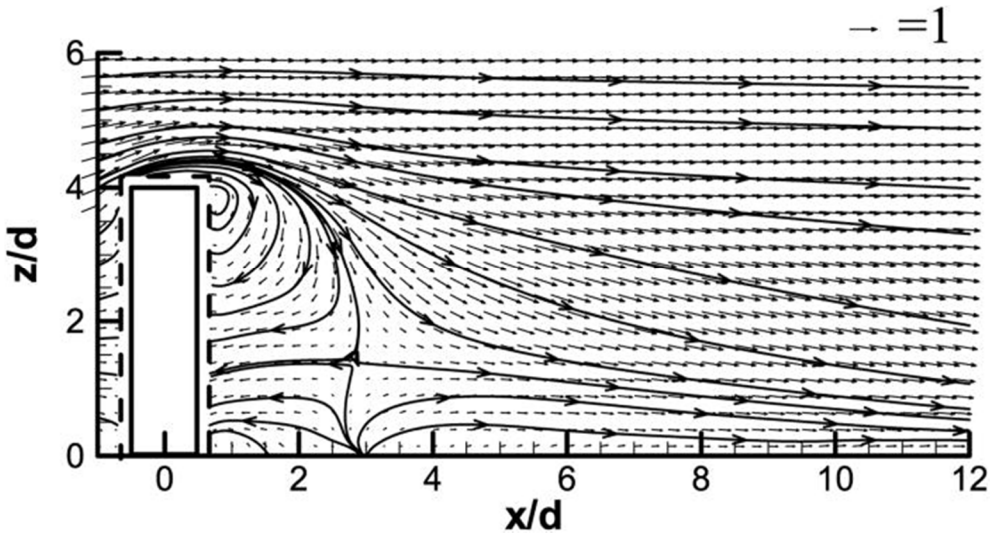

Figure 2.9: Mean streamlines and velocity vectors on the symmetry plane, $y/D = 0$ for a finite square prism of AR = 4, from Bourgeois et al. (2011). Note that in this figure, lowercase *d* is the width of the prism. Reprinted from Physics of Fluids, Vol. 23, Bourgeois, J.A., Sattari, P., and Martinuzzi, R.J., Alternate half-loop shedding in the turbulent wake of a finite surface-mounted square cylinder with a thin boundary layer, 095101 (15 pp.), 2011, with the permission of AIP Publishing.

Sumner (2015a) performed time-averaged measurements with a seven-hole pressure probe in both vertical and horizontal planes; the same approach is used for the current research.

Figure 2.9 shows an example of the mean flow streamlines in a vertical plane along the plane of symmetry, $y/D = 0$. A part of the flow, which separates at the leading edge of the prism, does not reattach at the tip of the prism. A strong "downwash" flow (downward-directed flow velocity) occurs immediately downstream of the free end of the prism in the near wake. The downwash flow is directed towards the ground and returns upstream to stagnate at the rear part of the prism. Also, a portion of the approaching flow closer to the prism-wall junction is directed towards the ground and returns upstream. The interaction between the downstream and upstream flow creates a region of flow known as a recirculation zone (Rostamy et al., 2012).

Measurements in the horizontal plane (*x*-*y*) give a clear idea about the extension of recirculation zone. Figure 2.10 shows the mid-height ($z/H = 0.5$) recirculation zone for a prism of AR = 4 in the *x*-*y* plane. A symmetric pair of counter-rotating vortices is seen on either side of the prism.

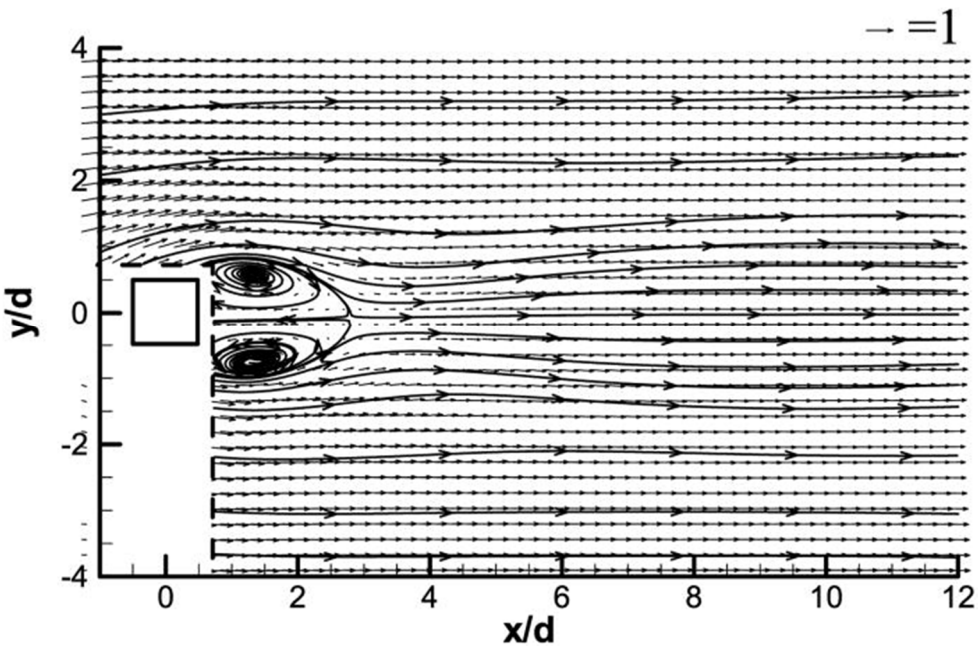

Figure 2.10: Mean sectional streamlines and velocity vectors showing the recirculation zone at $z/H = 0.5$, for a finite square prism of AR = 4, from Bourgeois et al. (2011). Note that in this figure, lowercase *d* is the width of the prism. Reprinted from Physics of Fluids, Vol. 23, Bourgeois, J.A., Sattari, P., and Martinuzzi, R.J., Alternate half-loop shedding in the turbulent wake of a finite surface-mounted square cylinder with a thin boundary layer, 095101 (15 pp.), 2011, with the permission of AIP Publishing.

Velocity vector measurements in the *y*-*z* plane give a good understanding about formation of vortices in the wake region. Figure 2.11 shows the mean velocity vectors of a finite square prism of AR = 4 at $x/D = 5$. A pair of symmetric counter-rotating vortices is seen at the mid-height region. These are the tip vortices, which originate from the free end of the square prism. The effect of "upwash" flow (upward-directed flow velocity) is much less compared to that of downwash flow.

2.3.4 Physical Model of the Flow

Based on the flow visualization and mean streamwise measurements, various models for the flow around a finite square prism were proposed. A model proposed by Wang and Zhou (2009) was based on the arch-type symmetric vortex structure behind a finite square prism. The experiments were carried out in the near wake of finite-height square prisms of AR = 3 to 7 at Re = 9300. Figure 2.12 presents the flow structure of a finite square prism with spanwise vortices

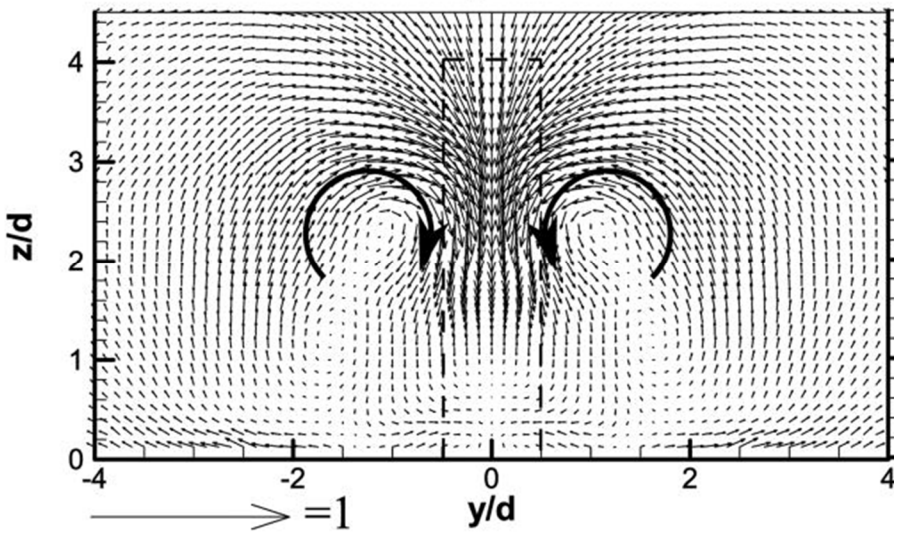

Figure 2.11: Mean velocity vectors (from reconstructed three-dimensional velocity field) at $x/D = 5$, for a finite square prism of AR = 4, from Bourgeois et al. (2011). Note that in this figure, lowercase *d* is the width of the prism. Reprinted from Physics of Fluids, Vol. 23, Bourgeois, J.A., Sattari, P., and Martinuzzi, R.J., Alternate half-loop shedding in the turbulent wake of a finite surface-mounted square cylinder with a thin boundary layer, 095101 (15 pp.), 2011, with the permission of AIP Publishing.

symmetrically arranged. In this model, spanwise vortices from both sides of the prism are connected with each other near the free end to form an arch-type vortex. This arch-type vortex structure consists of two legs within the wall boundary layer and join each other near the prism's free end. Under the influence of the free-end downwash flow and boundary layer over the wall, both the upper and lower parts of the arch-type structures are inclined upstream. For a prism whose aspect ratio is greater than critical aspect ratio, vortex shedding changes from symmetrical arch-type to antisymmetric Kármán type.

Figure 2.13 shows another schematic of the flow around a surface-mounted finite-height square prism whose aspect ratio is greater than the critical aspect ratio, from McClean and Sumner (2014). The model shows two pairs of time-averaged counter-rotating streamwise vortex pairs in the wake: the tip vortex pair in the upper part of the wake and the base vortex pair in the lower part of the wake. The tip vortex pair is responsible for downwash (downward-directed velocity) on the wake centerline in the upper part of the wake. The base vortex pair is responsible for upwash (upward-directed velocity) on the wake centerline close to the ground plane. The prism is sufficiently slender to allow periodic, alternating Kármán vortex shedding to occur from the

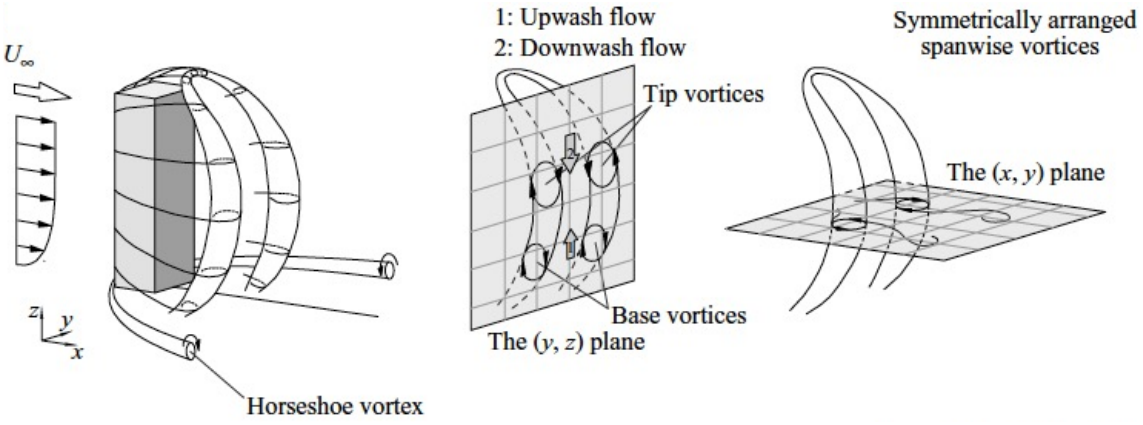

Figure 2.12: Model of the flow structure around a surface-mounted finite-height square prism, from Wang and Zhou (2009). Reprinted from Journal of Fluid Mechanics, Vol. 638, Wang, H.F., and Zhou, Y., The finite-length square cylinder near wake, pp. 453-490, 2009, with the permission of Cambridge University Press.

sides of the prism. A horseshoe vortex forms upstream of the prism on the ground plane, as the boundary layer interacts with the prism. Flow separates from the leading edge corners of the sides and free end of the prism. Above the free end, within the region of separated flow, there is weakly recirculating flow.

2.3.5 Effect of Aspect Ratio on the Mean Flow Pattern

The key feature of a finite square prism that differentiates it from an infinite square prism is the flow separation from the top leading edge (the free end) of the prism and its influence on the flow in the immediate wake region behind the prism. Rostamy et al. (2012) carried out PIV velocity measurements for finite square prisms of AR = 3, 5, 7 and 9 for Re = 4.3×10^4. They clearly identified the effects of aspect ratio on the reverse flow and its interaction with the separated flow and the overall flow behavior for a finite-square prism.

Figure 2.14 shows the flow patterns of finite square prisms of different aspect ratios. For all aspect ratios, it is evident that no reattachment of flow occurs at the free end of the prism. A part of the flow separated from the top becomes attached at the rear side of the prism. A very strong downwash flow can be clearly identified for all the aspect ratio prisms. A majority of the downwash flow in the recirculation zone interacts with the upwash flow and reattaches to the back

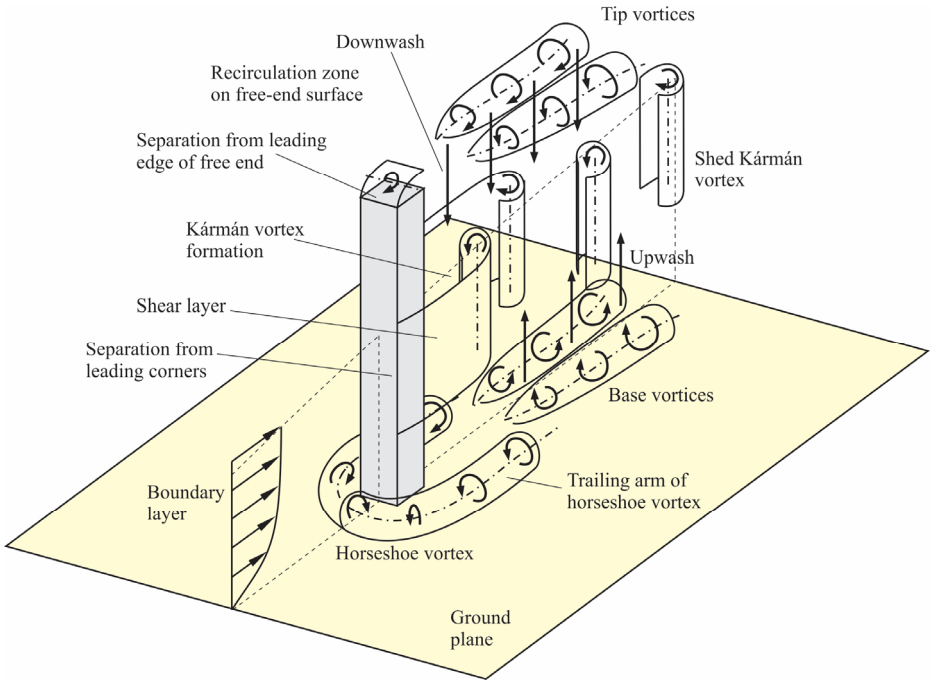

Figure 2.13: Schematic of the flow around a surface-mounted finite-height square prism partially immersed in a flat-plate boundary layer at zero incidence angle, with an aspect ratio greater than critical aspect ratio, from McClean and Sumner (2014). Figure created by D. Sumner (used with permission).

of the prism. There exists a saddle point where the velocity of the flow becomes zero. The saddle point represent the point of intersection of the upwash and downwash flow.

Another difference is the presence of a vortex behind the prism close to the ground plane, which is observed for the more slender prisms of AR = 7 and 9 (Figures 2.14a,b) but is weaker or nearly absent for AR = 5 and 3 (Figures 2.14c,d). The distinct flow behavior for AR = 3 (Figure 2.14d) suggests that a critical aspect ratio lies between AR = 3 and AR = 5 for their experimental conditions, below which the wake has a different structure.

2.3.6 Effect of Incidence Angle on Mean Flow Pattern

For a square prism, as the incidence angle (α) is increased from 0° to 45°, changes occur in the mean drag coefficient, mean lift coefficient and Strouhal number. These changes are associated with the change in the mean flow patterns about the prism. As discussed earlier in this chapter, few studies have focused on the incidence-angle effects of the finite square prism (e.g.,

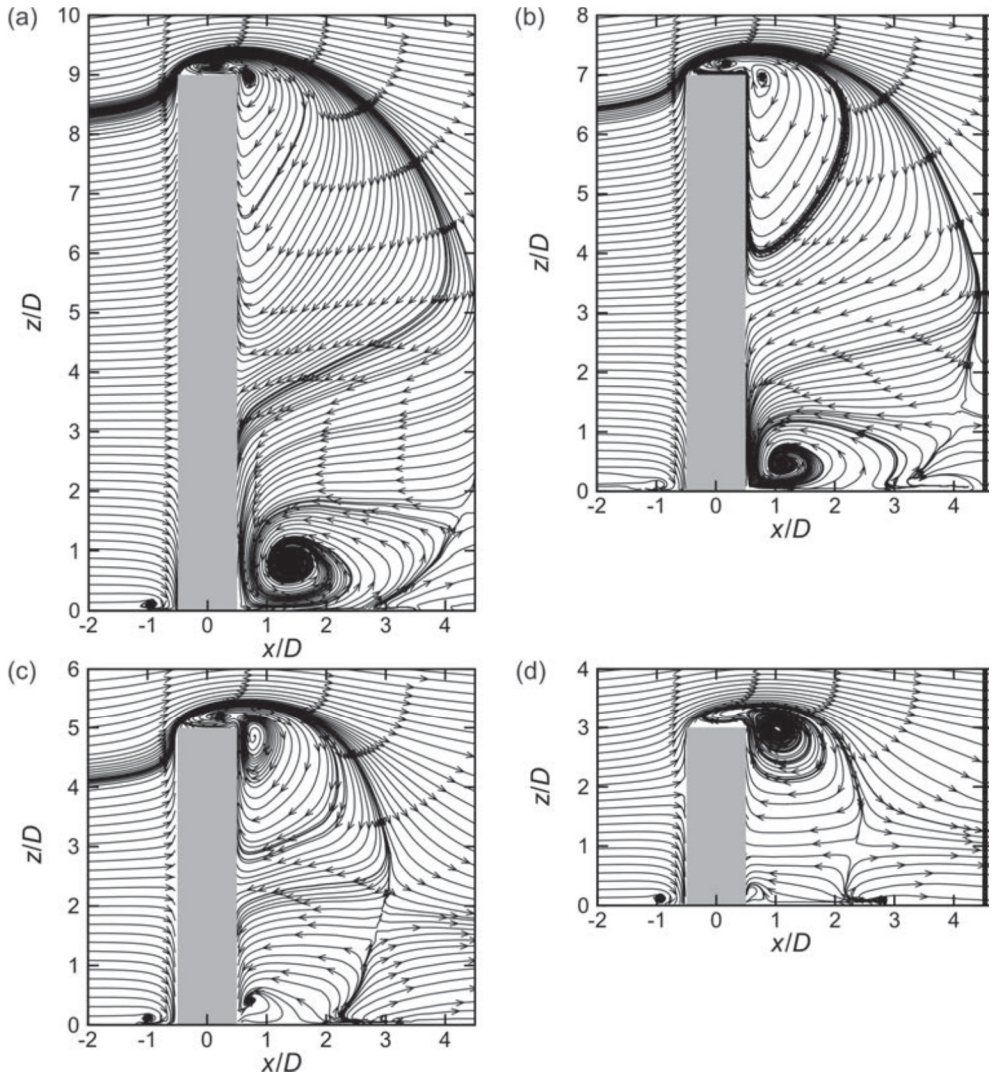

Figure 2.14: Mean streamlines in a vertical plane on the wake centerline ($y/D = 0$, the symmetry plane) for finite square prisms of (a) AR = 9, (b) AR = 7, (c) AR = 5, and (d) AR = 3, from Rostamy et al. (2012). Figure created by D. Sumner (used with permission).

Sarode at al. (1981), Sakamoto (1985), McClean and Sumner (2014), Ogunremi and Sumner (2015a)); rather, most studies have been carried out at $\alpha = 0°$.

Okuda and Taniike (1993) studied the effect of incidence angle (α = 0° to 45°) and boundary layer thickness ($\delta/H < 1$ and $\delta/H > 1$) on the pressure distribution and flow field around a surface-mounted finite square prism of AR = 4. This is one of the few studies to consider incidence angle effects on the flow field.

Ogunremi and Sumner (2015a) studied the effect of incidence angle on the mean wake of a finite square prism of AR = 3. Wake velocity measurements were carried out in two vertical

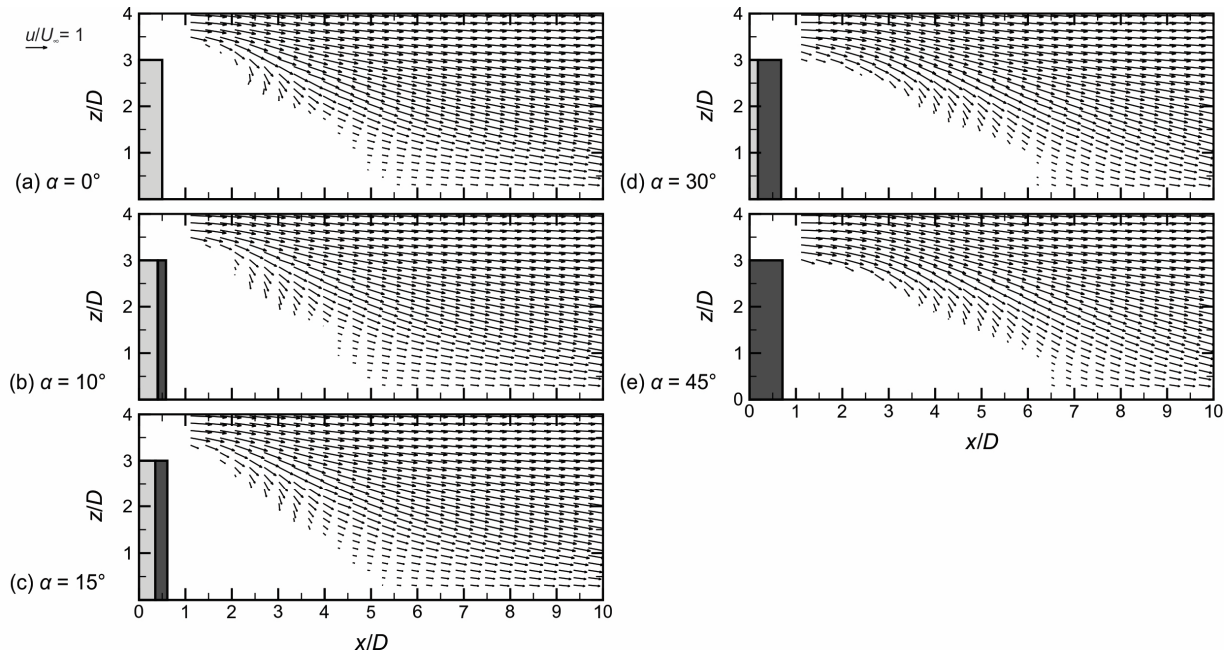

Figure 2.15: Mean velocity vectors (streamwise, u, and vertical, w, components shown) downstream of a finite square prism of AR = 3 in a vertical (x-z) plane on the centerline of the wind tunnel test section (y/D = 0): (a) α = 0°, (b) α = 10°, (c) α = 15°, (d) α = 30°, and (e) α = 45°, from Ogunremi and Sumner (2015a). Figure created by D. Sumner (used with permission).

planes at a distance of 10D from the centre of the prism using a seven-hole probe. Mean velocity measurements along the vertical central plane are shown in Figure 2.15. The mean recirculation zone extends downstream to a maximum of x/D = 5.5 close to ground plane and vertically up to 3.5D above the prism, α = 0° (Figure 2.15a). When the prism is rotated (α = 10°, Figure 2.15b), there is a small shrinkage in recirculation zone. The shortest recirculation appears at the critical incidence angle that lies between α = 12° to 16° (Figure 2.15c). At α = 30° and 45° (Figures 2.15d,e), there is a progressive lengthening of the recirculation zone to x/D = 6 to x/D = 6.5. The wake becomes thicker with the increase in α.

Figure 2.16 shows the mean velocity vectors downstream of a finite square prism in the y-z plane for various prism orientations. At α = 0° (Figure 2.16a) there exists a pair of symmetric counter-rotating vortices in the wake region of the square prism. As the prism is rotated, there occurs an asymmetry in the mean wake. There exists a critical incidence angle at which the wake exhibits the highest degree of lateral asymmetry. The asymmetry becomes stronger at α = 10° and α = 15° (Figures 2.16c,d) which coincides with the critical incidence angle. The counter-clockwise vortex, which occurs at the wider side (right-hand side, +y direction) of the wake, shifts upwards

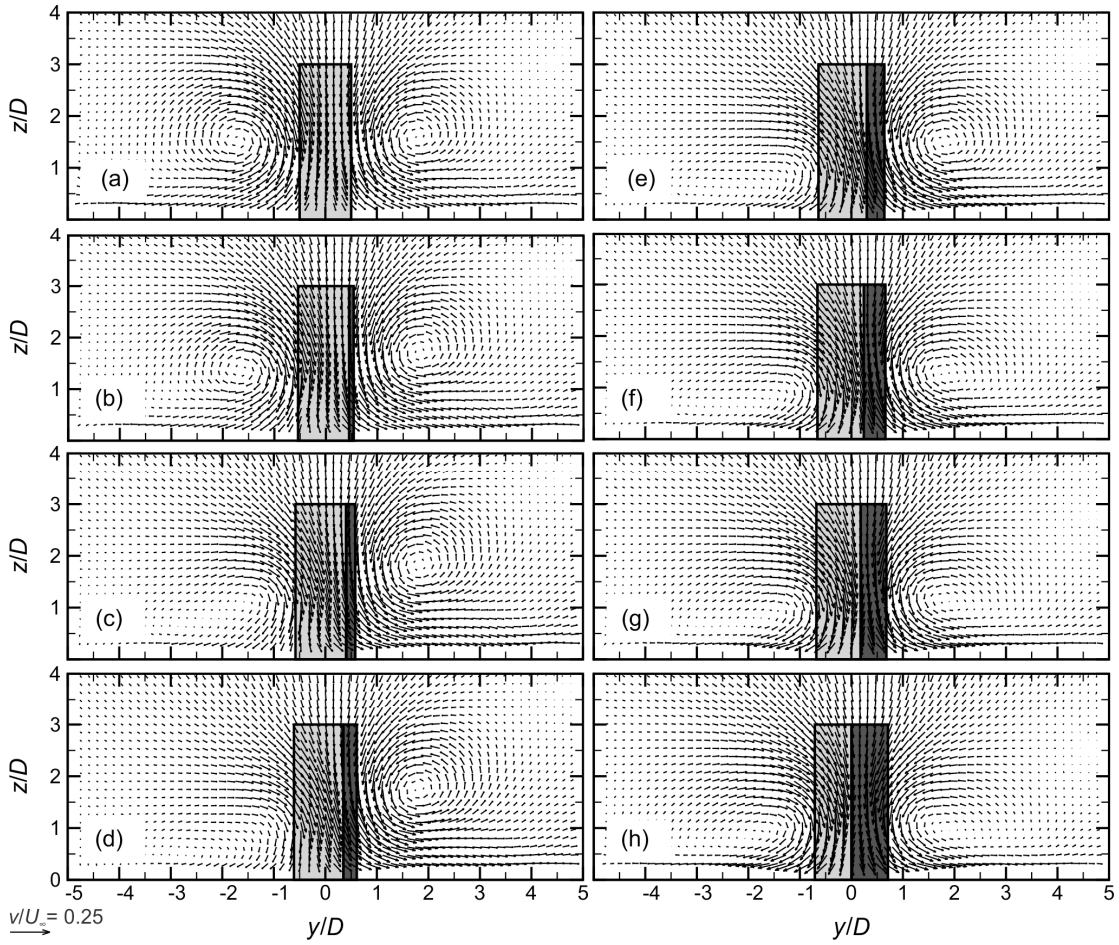

Figure 2.16: Mean velocity vectors (cross-stream, v, and vertical, w, components shown) downstream of the finite square prism of AR =3 in a vertical (y-z) plane at x/D = 10, from the experiments of Ogunremi and Sumner (2015a): (a) α = 0°, (b) α = 5°, (c) α = 10°, (d) α = 15°, (e) α = 20°, (f) α = 25°, (g) α = 30°, (h) α = 45°. Figure created by D. Sumner (used with permission).

from the ground plane with the increase in incidence angle. The clockwise vortex which occurs on the narrower side (left-hand side, $-y$ direction) of the wake moves closer to the ground plane with the increase in incidence angle. At α = 45° (Figure 2.16h) the tip vortex pair moves closer to the ground plane and becomes symmetric.

2.3.7 Mean Drag Force Coefficient

Sarode et al. (1981) measured the mean aerodynamic force coefficients for surface-mounted finite-height square prisms of AR = 1.14 to 10 at Re = 2.2×10^4. The incidence angle was varied from α = 0° to 45°. It was observed that with the decrease in aspect ratio (from AR = 10 to

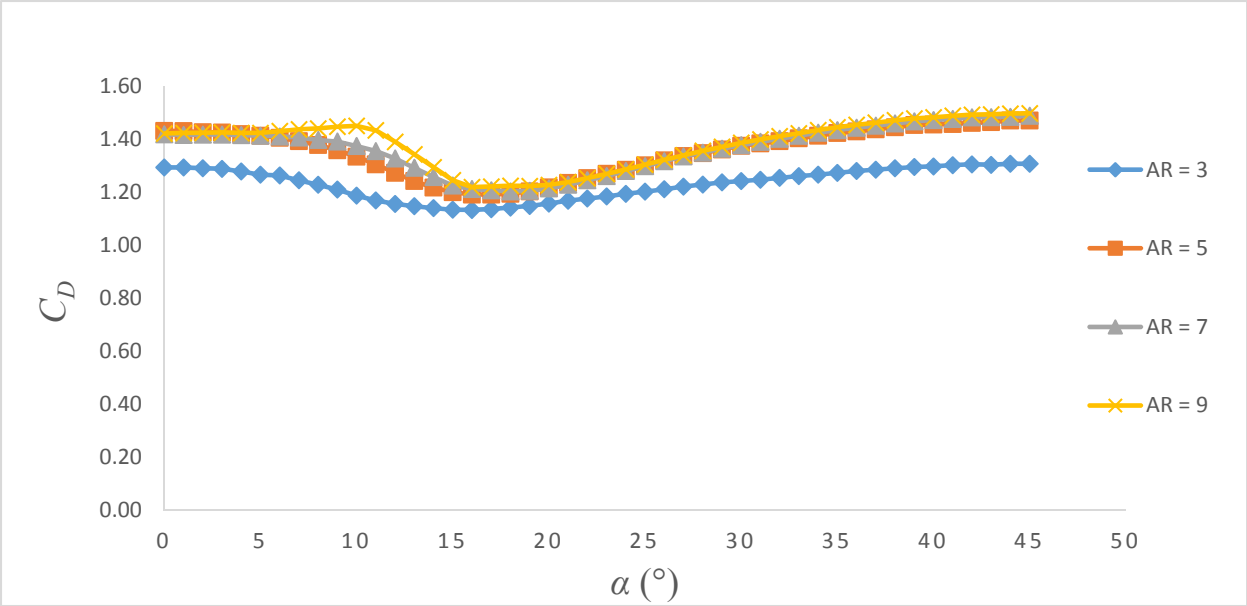

Figure 2.17: Mean drag coefficient (C_D) against incidence angle (α) for finite square prisms of aspect ratio AR = 3 to 9, from McClean and Sumner (2014).

AR = 1.14), the mean drag coefficient reduced for all incidence angles. The incidence angle effects on C_D were greatest for high-aspect-ratio prisms, AR = 6.36 and 10. The incidence angle effects were less pronounced for low aspect ratio prisms, AR = 1.14 to 3.64.

Another important study on the incidence angle effects for a surface-mounted finite-height prism was done by Sakamoto (1985). The aspect ratios ranged from AR = 1 to 5 at Re = 3.3×10^4 to 1.65×10^5. His finding was similar to that of Sarode et al. (1981) with the drag coefficient reducing as the aspect ratio was reduced from AR = 5 to 1. The incidence angle effects were more pronounced at high aspect ratio (AR = 5) and were the lowest at AR = 1. Also, there was a reduction in critical incidence angle from α = 17.5° at AR = 5 to α = 12.5° at AR = 1.

McClean and Sumner (2014) studied the effects of aspect ratio and incidence angle for square prisms of AR = 3, 5, 7, 9 and 11 at incidence angle ranging from 0° to 45°. Figure 2.17 shows the variation of C_D with incidence angle for finite square prisms. The drag coefficient for a finite square prism is much lower than that of an infinite square prism (see results presented earlier in Figure 2.6). The lower value of C_D for finite square prisms can be explained in terms of the strong downwash and three-dimensionality in the flow. The maximum value of C_D was observed at α = 45° for a finite square prism. The experiments of McClean and Sumner (2014) show a distinct behaviour at AR = 3, for which the mean drag coefficients were least, and incidence angle

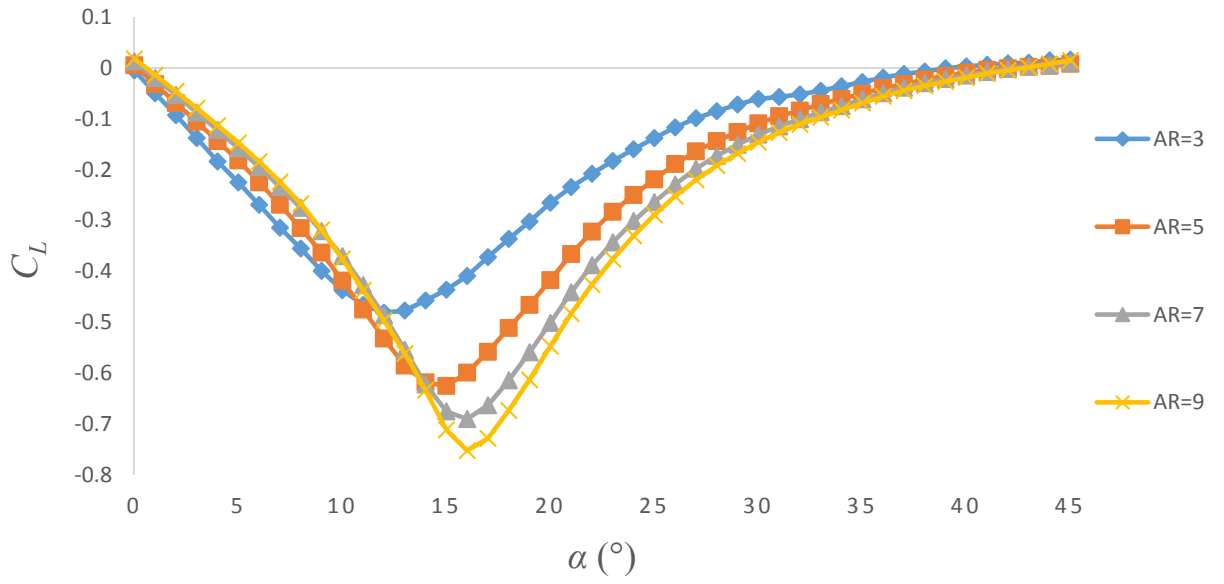

Figure 2.18: Mean lift coefficient (C_L) against incidence angle (α) for finite square prisms of aspect ratio AR = 3 to 9, from McClean and Sumner (2014).

effects were least pronounced, suggesting that AR = 3 lies below the critical aspect ratio for their experimental conditions.

2.3.8 Mean Lift Force Coefficient

There is a strong influence of aspect ratio and incidence angle on the mean lift coefficients for a square prism. Figure 2.18 shows the variation of mean lift coefficient with α. The data were plotted based on the width of the prism. Sarode et al. (1981) observed that with the decrease in aspect ratio (AR = 10 to 1.14), the mean lift coefficient was reduced for all incidence angles. For all aspect ratios, there was a strong variation of C_L with incidence angle.

With the increase in incidence angle from α = 0° to 27.5° (Figure 2.18), the mean lift coefficient remains negative indicating the force is directed in the negative-y direction. The minimum lift coefficient (maximum lift coefficient magnitude) lies between α = 12° to 15° depending on the experimental conditions. Between α = 27.5° to 45°, a small positive lift force is obtained for the infinite square prism. For the McClean and Sumner (2014) experiments (Figure 2.20), the critical incidence angles were obtained between α = 12° to 16°. The lowest value of C_L for AR = 3 indicates that the prism lies below the critical aspect ratio for their experimental conditions. Also, the value of C_L remains negative for all incidence angles, in contrast to results

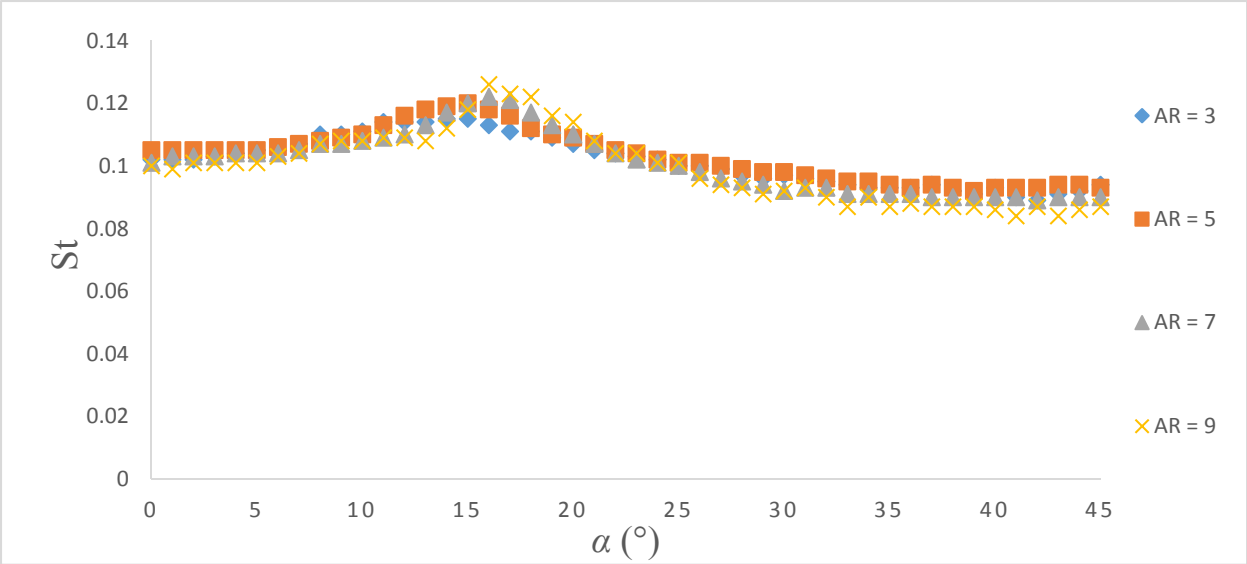

Figure 2.19: Strouhal number at the mid-height position in the wake for finite square prisms of AR = 3 to 9, from McClean and Sumner (2014).

for an infinite square prism, shown earlier in Figure 2.5, where the lift coefficient attains a small positive value at high incidence angles.

2.3.9 Strouhal Number

Sakamoto et al. (1983) studied the effects of AR and the boundary layer characteristics on the vortex shedding frequency for rectangular prisms and cylinders, for AR = 1 to 8. It was observed that the Strouhal number increases with an increase in aspect ratio of the prism. Also, a different behavior at AR = 2 suggested that the critical aspect ratio of the prism was AR = 2 for their experimental conditions. As the aspect ratio of the prisms was decreased, the strength of the vortex shedding from the prism decreased.

Some St data obtained at the mid-height positions for finite square prisms, from McClean and Sumner (2014), are plotted in Figure 2.19. With the increase in α, the Strouhal number also increases and reaches a maximum value for both infinite and finite square prisms. The infinite prism data were plotted earlier in Figures 2.7 and 2.8. For the results in Figure 2.19, the critical incidence angle lies between 15° to 17° where the maximum St value occurs. The lowest value of St was obtained at an incidence of 45°. For all incidence angles, the St value is lower than that of an infinite square prism (see Figure 2.98).

CHAPTER 3. EXPERIMENTAL APPARATUS AND INSTRUMENTATION

3.1 Introduction

This chapter contains a description of the test facility, experimental apparatus, and measurement instrumentation used in the thesis research. The experiments were conducted in a low-speed wind tunnel, which is described in Section 3.2. The square prism models are described in Section 3.3. The measurement instrumentation, including the results of an uncertainty analysis, are presented in Sections 3.4 and 3.5

3.2 Low-Speed Wind Tunnel

All of the experiments were carried out in the low-speed closed-return wind tunnel located in the Department of Mechanical Engineering at the University of Saskatchewan. A schematic of the wind tunnel is shown in Figure 3.1.

A variable-pitch blade fan is used to drive the airflow in the tunnel. The airstream passes through a closed tube where it then enters two sets of turning vanes located at the first two corners of the wind tunnel. The airstream from the turning vanes is directed towards the turbulence reduction screens which reduce the turbulence intensity in the airflow. The airflow then passes through a low-speed settling chamber. Finally, the airflow is accelerated through a contraction and into the test section. The side walls of the test section are made of Plexiglas which helps in visualization of the experiments. Downstream of the test section, the flow expands through a diffuser and passes through two more corners (with turning vanes) before reaching the fan.

The test section (Figure 3.2) has dimensions of 0.91 m (height) × 1.13 m (width) × 1.96 m (length). Airflow velocities of up to 50 m/s can be obtained in the test section. In the present experiments, a freestream velocity of U_∞ = 20 m/s was used. The streamwise turbulence intensity of the airflow in the test section is less than 0.6% at U_∞ = 20 m/s. The test section is equipped with a computer controlled turntable that is used for rotating the test models (square prisms). On top of the turntable is mounted a six-component force balance. The models themselves were attached to force balance. The force balance (which was not used in this research) and the model were then rotated together on the turntable, which is controlled by a stepping motor. An aluminum

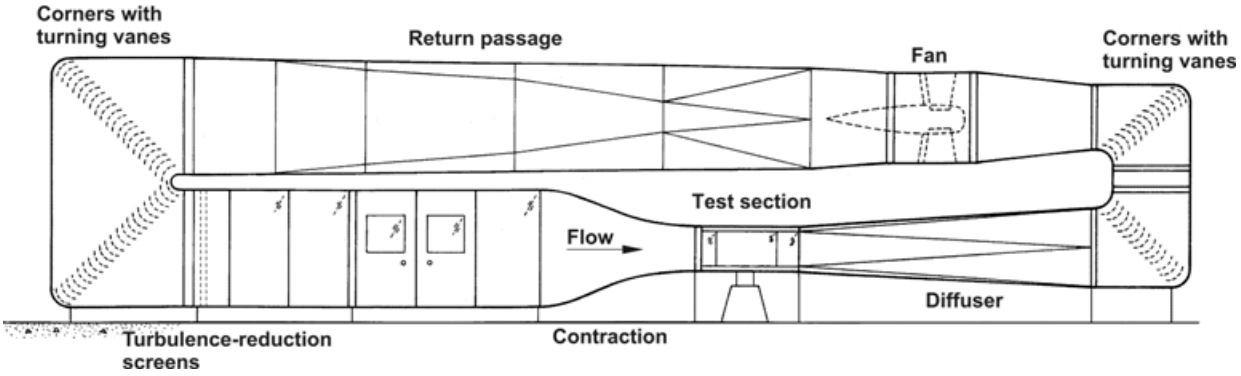

Figure 3.1: Schematic of the low-speed wind tunnel at the University of Saskatchewan, Department of Mechanical Engineering, which was used for the present experiments.

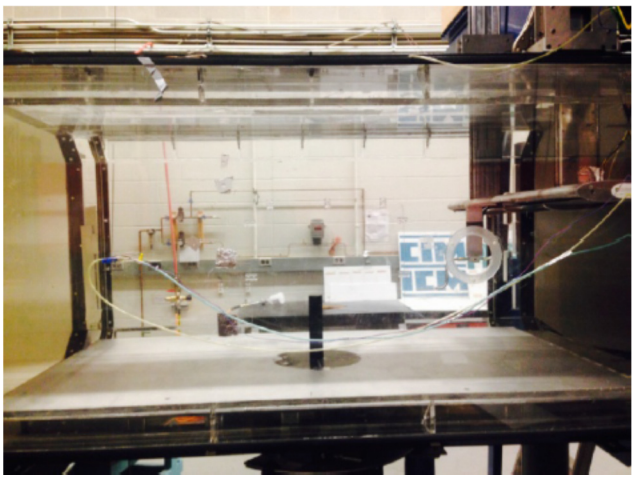

Figure 3.2: Photograph of the wind tunnel test section, flow from left to right, showing the prism, Pitot-static probe, traversing wing, and seven-hole probe.

ground plane was installed on the floor of the wind tunnel test section. In the present experiments, the square prism was mounted normal to the ground plane at a location 900 mm downstream of the ground plane's leading edge. The test section also contains a computer-controlled traversing system, which is used to position measurement probes inside the test section.

3.3 Square Prism Models

Finite square prisms, shown in Figure 3.3, of width $D = 31.5$ mm and heights ranging from $H = 157.5$ mm (for AR = 5) to 283.5 mm (for AR = 9), with smooth surfaces and sharp edges, were tested. The same prisms were used in earlier experimental work conducted at the University

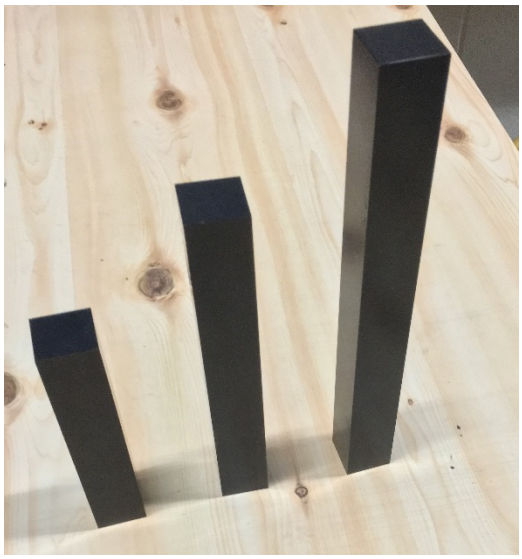

Figure 3.3: The finite square prism models used in the experiments (AR = 5, 7, 9).

of Saskatchewan and reported in Rostamy et al. (2012), McClean and Sumner (2014), and Ogunremi and Sumner (2015a,b). The square prisms were anodized flat black for the particle image velocimetry (PIV) experiments of Rostamy et al. (2012). The prisms were oriented at incidence angles of α = 0°, 5°, 10°, 15°, 20°, 25°, 30° and 45° with the help of the turntable. The estimated uncertainty of the turntable's angular position was ±0.5°.

3.4 Instrumentation

A United Sensor 3.2-mm diameter Pitot-static probe (with a built-in thermocouple), a Datametrics Barocel Type 600 absolute pressure transducer (Model 600A-1000T-513-H21X-4), and a Datametrics Barocel Type 590 differential pressure transducer (Model 590D-10W-2QB-VIX-4D) (with a thermal base) were used to measure the freestream static pressure, P_∞, freestream dynamic pressure, q_∞, and freestream air temperature, T_∞. These instruments are shown in Figure 3.4. The Pitot-static probe (Figure 3.4c) was mounted on the side wall of the test section at a distance of 400 mm from contraction exit and at a height of 340 mm above the ground plane. The probe was carefully aligned with the freestream.

The data acquisition system included a National Instruments PCIe-6259 16-bit data acquisition board, a personal computer and LabVIEW software (Figure 3.5). Data were typically sampled at a rate of 1 kHz, and time-averaged over a sampling period of 10 to 20 s.

The density of air (ρ_∞) was calculated using the ideal gas equation, given by

(a) (b)

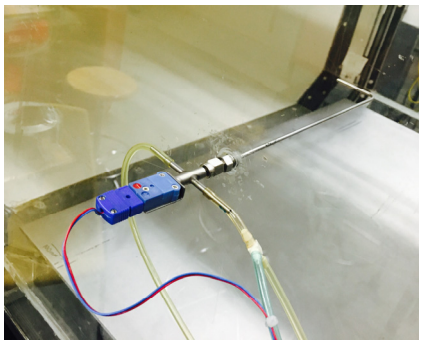

(c)

Figure 3.4: Instrumentation for measuring the freestream conditions: (a) Datametrics Barocel Type 600 absolute pressure transducer, (b) Datametrics Barocel Type 590 differential pressure transducer, and (c) United Sensor 3.2-mm diameter Pitot-static probe.

$$\rho_\infty = P_\infty/(RT_\infty), \tag{3.1}$$

where R is the gas constant for air (R = 287 J/(kg·K)). The dynamic viscosity of the air (μ_∞) was calculated using the Sutherland correlation, given by White (2003),

$$\mu_\infty = \mu_0 \left(\frac{T}{T_0}\right)^{3/2} \left(\frac{T_0+S}{T+S}\right), \tag{3.2}$$

where μ_0 = 1.71×10^{-5} Ns/m^2, T_0 = 273 K, and S = 110.4 K. Using the dynamic viscosity, the kinematic viscosity of the air (ν_∞) can be calculated by

$$\nu_\infty = \mu_\infty / \rho_\infty. \tag{3.3}$$

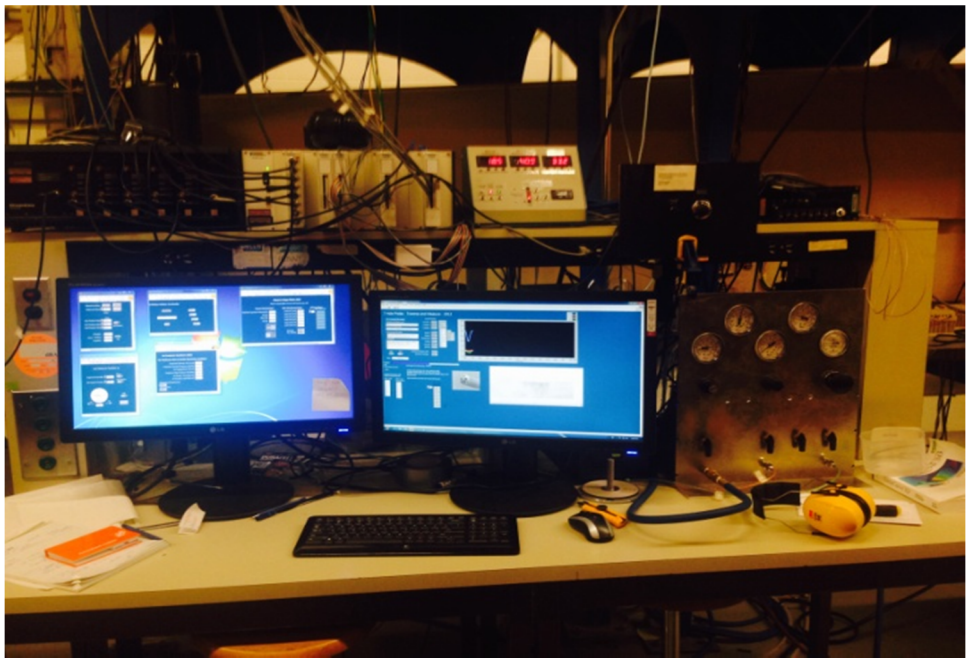

Figure 3.5: Computer, data acquisition system components, and LabVIEW "virtual instruments" used for the wind tunnel experiments.

3.4.1 Flow Conditions

The experiments were conducted at a freestream velocity of $U_\infty = 20$ m/s, giving a Reynolds number of $Re = 3.7\times10^4$. A fully developed flat-plate turbulent boundary layer was formed on the ground plane at the location of the square prism. The boundary layer data for the current experiments are presented in Table 3.1. The boundary layer's mean velocity profile (Figure 3.6) at the location of the prism gives a relative thickness of $\delta/D = 1.5$ at $U_\infty = 20$ m/s. The boundary layer was not tripped but was allowed to form naturally from the leading edge of the ground plane.

The time-averaged velocity field in the wake of the square prism was measured using a seven-hole pressure probe. This probe has been used in several previous research programs at the University of Saskatchewan, with results reported in Sumner et al. (2004), Adaramola et al. (2010), and Ogunremi and Sumner (2015a,b). The seven-hole probe measures the time-averaged velocity vector (corresponding to mean velocity components u, v, and w, oriented in the x, y, and z directions, respectively). The seven-hole probe used in the present study (Figures 3.7a,b) was manufactured by Engineering Shops at the University of Saskatchewan. The probe is conical in shape with a cone angle of 30° and a diameter of 3.45 mm. It is comprised of seven, closely packed

1-mm diameter stainless steel tubes, fitted into an outer stainless steel sleeve. The probe can measure the three velocity components of flow at flow angles up to 70° from the probe axis.

Table 3.1: Summary of boundary layer measurements on the ground plane for finite square prism experiments, U_∞ = 20 m/s (Rostamy (2012)).

Location, x/D	Boundary layer thickness, δ (mm)	Displacement thickness, δ^* (mm)	Momentum thickness, θ (mm)	Shape factor, $H = \delta^*/\theta$	Reynolds number based on x, Re_x	Reynolds number based on θ, Re_θ	δ/θ
0	51	5.7	4.6	1.3	1.6×10^6	5.9×10^6	1.6
5	54	6.1	4.9	1.2	1.6×10^6	6.6×10^6	1.7
10	56	6.3	5.0	1.2	1.9×10^6	6.8×10^6	1.8

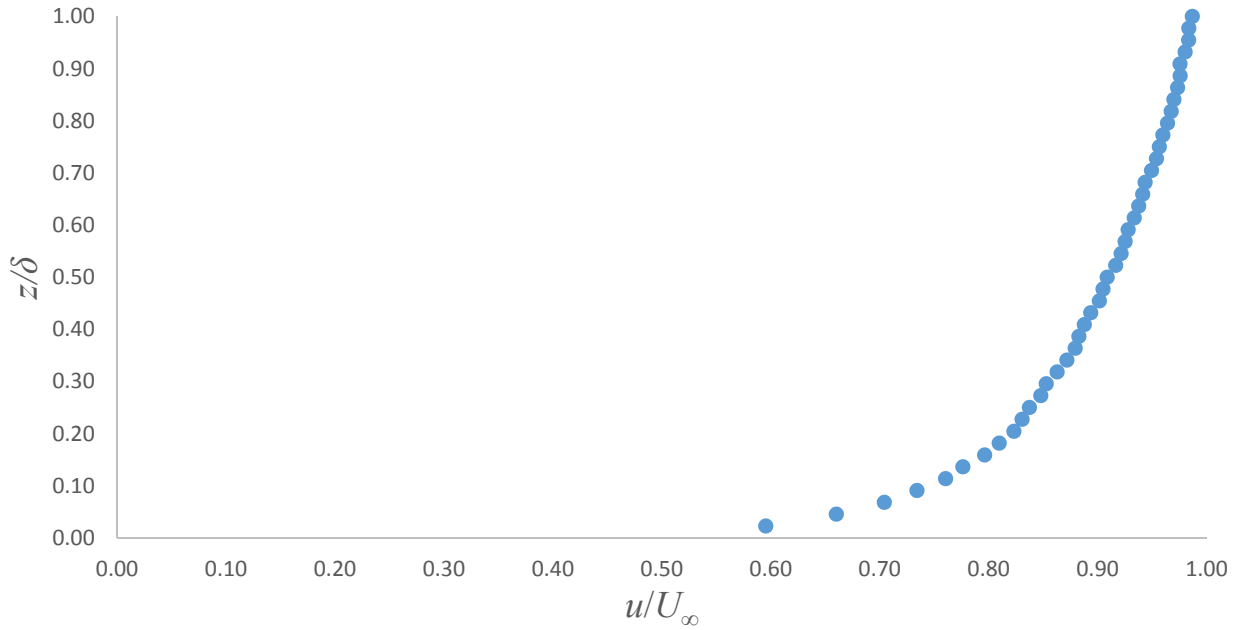

Figure 3.6: The ground plane boundary layer mean velocity profile for a freestream velocity of U_∞ = 20m/s at x/D = 0, where x is the location of the prism.

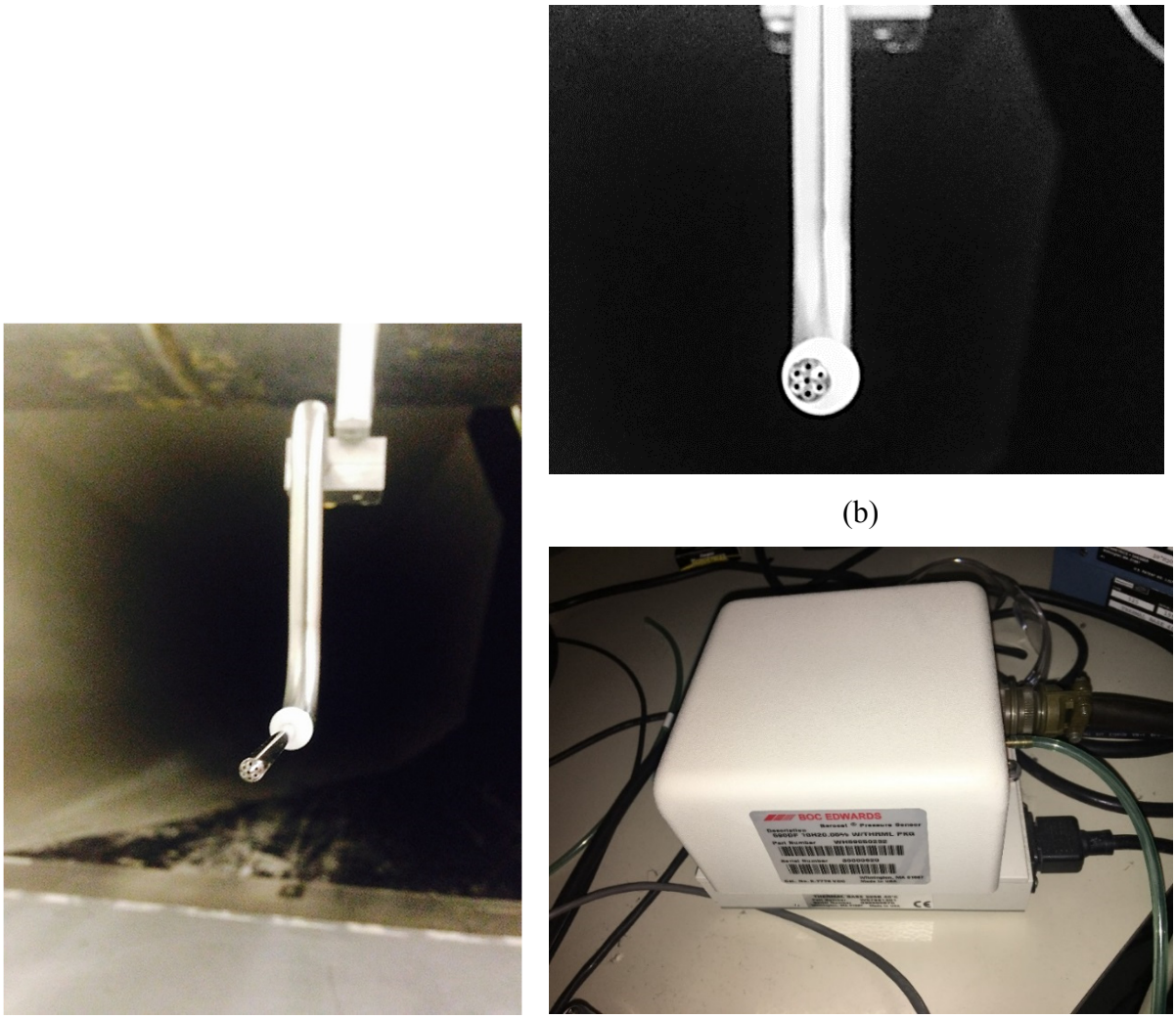

(a) (b) (c)

Figure 3.7: Photographs showing (a) the seven-hole probe mounted in the wind tunnel's traversing wing, (b) a close-up of the seven-hole probe, and (c) the BOC Edwards Model 590DF differential pressure transducer.

The seven pressures are measured with a Scanivalve ZOC171P/8Px pressure scanner shown in Figure 3.8. The Scanivalve ZOC17 (Zero, Operate, Calibrate) measures individual pressures from the seven-hole probe. The calibration valve automatically calibrates the ZOC17 pressure sensors online i.e., during the measurement. A BOC Edwards Model 590DF differential pressure transducer (Figure 3.7c) provides an accurate reference pressure for online calibration checks of the ZOC17's pressure transducers. For the present experiments, a calibration check was done at every 200 mm of vertical travel of the probe. Figure 3.9 shows the pressure control panel used for calibrating and operating the ZOC17 unit.

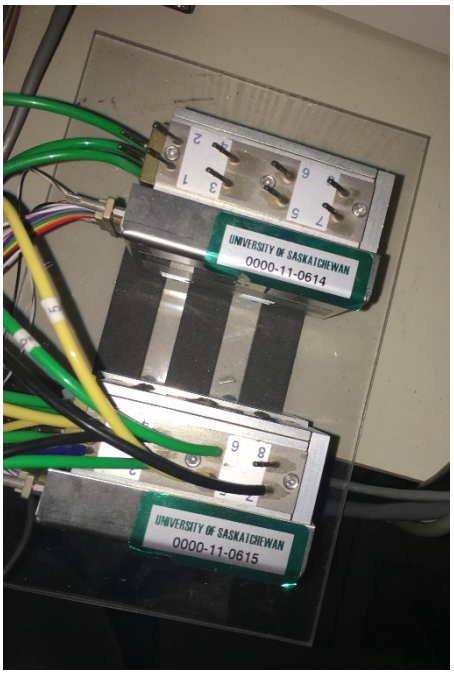

Figure 3.8: Photograph of the ZOC17 pressure scanner connected to the seven-hole probe for measurements.

A direct-interpolation calibration data reduction method was used for the seven-hole probe, as described by Sumner (2002). The calibration grid spacing had an angular range of ±72.9° in pitch angle and yaw angle with an angular increment of 8.1°. The data reduction method uses the seven measured pressures from the probe to calculate the pitch angle, yaw angle, dynamic pressure coefficient, and static pressure coefficient, from which the three velocity components, u, v, and w, are calculated. Further information on the data reduction method can be found in Sumner (2002).

3.5 Uncertainty Analysis

The instruments used in the experiments, such as the pressure transducers, data acquisition system, seven-hole probe, Pitot-static probe, and thermocouple, along with the test environment itself, all have errors associated with them. These errors influence the measurements made in the experiments.

For a Pitot-static probe, which was used to measure the freestream conditions, the main sources of error that would be important in the present experiments include yaw and pitch angle errors, turbulence intensity errors, and Reynolds number effects (Bryer and Pankhurst, 1971). The angular error was considered to be very small since the probe was carefully aligned with the

Figure 3.9: Pressure control panel for calibrating the ZOC17 pressure scanner.

freestream. The freestream was also of low turbulence intensity (0.6% streamwise turbulence intensity at U_∞ = 20 m/s), and therefore the error due to elevated turbulence is expected to be very small. Reynolds number effects are also very small: at U_∞ = 20 m/s, the probe Reynolds number (based on the probe external diameter of 3.2 mm) was 3900, while significant Reynolds number effects would be expected only at probe Reynolds numbers of approximately 300 or lower (Bryer and Pankhurst, 1971).

The main sources of error in the freestream conditions were therefore related to the pressure transducers. The freestream absolute static pressure (P_∞) was measured with the Datametrics Barocel Type 600 absolute pressure transducer, with a full scale of 1000 Torr = 133.3 kPa, which has a reported accuracy of ±0.15% of reading and a repeatability of ±0.01% of full scale (Datametrics, 1982a). The freestream dynamic pressure (q_∞) was measured with the Datametrics Barocel Type 590 differential pressure transducer (with a thermal base) with a full scale of 10 inches H_2O, which has an accuracy of ±0.05% of reading + 0.001% of full scale and a repeatability of ±0.01% of reading + 0.005% of full scale (Datametrics, 1982b). The seven-hole probe pressures were measured with the Scanivalve ZOC17 pressure scanner; each transducer has a full scale of 10 inches H_2O and a reported accuracy of ±0.20% of full scale (Scanivalve 2014). Other errors

are introduced by the pressure calibration curves, but these are considered to be small compared to the individual accuracies of the instruments.

The type K thermocouple used to measure the freestream temperature, which was embedded inside the Pitot-static probe, was estimated to have an error of ±0.1°C.

The data acquisition errors were considered to be very small, since the analog-to-digital converter was 16-bit and the voltage input ranges were maximized for all readings using appropriate gains.

Wind tunnel blockage was very small for all of the prism models. The largest prism, of AR = 9, had a solid blockage ratio (the ratio of frontal area to the cross-sectional area of the test section) of approximately 0.9%, which means blockage effects are insignificant (Barlow et al., 1999).

Probe positioning error, using the automated traversing system, was estimated to be ±0.5 mm. For the largest measurement grids (for the prism of AR = 9), the size of the measurement grid (using a 5-mm grid spacing) was more than 3700 points. It was observed following these experiments, after repeated movements in the x, y, and/or z directions that the probe could be returned to its original position or datum with an error of less than 1 mm.

From the above discussion, and using typical values for the freestream conditions, representative uncertainty values can be estimated using the root-sum-square approach to account for multiple sources of error (e.g., Figliola and Beasley (2011)). These results are presented in Table 3.2. Based on the analysis and the results in Table 3.2, it is reasonable to assume that the measurements of the freestream conditions have uncertainties of less than 1%.

For the seven-hole probe measurements, Sumner et al. (2004) estimated the total velocity magnitude uncertainty to be less than 5%, for similar wake velocity measurements as in the present thesis, and flow angle errors of less than 3°.

Table 3.2: Summary of uncertainty analysis.

Measurement	Typical Value	Accuracy	Repeatability	Total Error	% Error
P_∞	96.0 kPa	0.144 kPa	0.013 kPa	0.290 kPa	0.3%
q_∞	225.0 Pa	0.113 Pa 0.025 Pa	0.023 Pa 0.124 Pa	0.342 Pa	0.15%
T_∞	25.0°C			0.1°C	0.4%

Variable	Calculated Value	Total Error	% Error
ρ_∞	1.136 kg/m^3	0.00684 kg/m^3	0.6%
μ_∞	1.841×10^{-5} Ns/m^2	1×10^{-7} Ns/m^2	0.5%
U_∞	19.90 m/s	0.0668 m/s	0.3%

CHAPTER 4. EFFECTS OF ASPECT RATIO AT ZERO INCIDENCE ANGLE

4.1 Introduction

In this chapter, the effects of aspect ratio are discussed for finite prisms oriented at an incidence angle of $\alpha = 0°$, i.e., where the prism face is oriented normal to the incident flow. The time-averaged wake velocity measurements were taken in two vertical planes, oriented in the streamwise direction (*x*-*z* plane) and the cross-stream direction (the *y*-*z* plane), for surface-mounted finite square prisms of AR = 9, 7 and 5. The measurements in the *x*-*z* plane (Section 4.2), corresponding to the vertical symmetry plane ($y/D = 0$) and parallel to the incident flow, give a clear idea of the maximum extent of the mean recirculation zone. The measurements in the *y*-*z* plane (Section 4.3) were made at $x/D = 10$ and normal to the incident flow show clearly the mean streamwise vortex structures in the wake region. The measurements were made at $x/D = 10$ to ensure that they were outside the mean recirculation zone. The grid spacing in the *x*-*z* plane was 10 mm in the *x* direction and 5 mm in the *z* direction. The grid spacing in the *y*-*z* plane was 5 mm in both directions.

The results are compared with data from Sumner et al. (2004) obtained for surface-mounted finite cylinders. It is worth mentioning that the experiments of Sumner et al. (2004) were carried out at a Reynolds number of $Re = 6\times10^4$ with a boundary layer thickness-to-diameter ratio of $\delta/D = 2.6$, while the present experiments were carried out at a slightly lower Reynolds number of $Re = 3.7\times10^4$ and slightly thinner boundary layer of $\delta/D = 1.5$.

4.2 Flow in the Vertical Plane Parallel to the Incident Flow (*x*-*z* Plane)

The time-averaged wake velocity fields of the finite square prisms, made in the vertical symmetry plane on the centreline of the wind tunnel test section, are shown in Figure 4.1. The velocity field (velocity components *u* and *w*) is made dimensionless with the freestream velocity, U_∞. Upstream of the prism (not seen in Figure 4.1) for all three aspect ratios, part of the approach flow moves up and separates from the leading edge of the free end. No reattachment occurs on the free end. The other part of the approach flow, closer to the ground plane, moves downwards

near the prism and recirculates upstream in the prism-wall junction region. This region contains the horseshoe vortex (identified later in Figure 4.4).

Downwash (downward-directed velocity) occurs directly behind the free end and persists in the streamwise direction in the upper part of the wake. For the square prism of AR = 9 (Figure 4.1a), the downwash extends up to 8.4*D* towards the ground plane from the free end. In contrast, for a finite cylinder of AR = 9 (Figure 4.1d), the downwash extends only up to 5*D* below the free end. Near the ground plane, there is no evidence of upwash (upward-directed velocity) for all three square prisms, but a small upwash is clearly seen for the finite cylinders (Figures 4.1d,e,f).

There exists a region of high-angled and reversing flow immediately behind the prism which corresponds to the mean recirculation zone. This flow typically exceeds the angular range of the seven-hole probe, or, because it is reversing, cannot be measured by the seven-hole probe. Hence, the recirculation zone is shown in Figure 4.1 as the region where there is an absence of velocity vectors; the angular range of the seven-hole probe is estimated to be ±70° (Sumner, 2002). From the results in Figure 4.1, it can be seen that the maximum streamwise extent of the mean recirculation zone increases with the increase in aspect ratio; this trend is the same for both the finite prism and the finite cylinder.

Figure 4.2 shows how the maximum length of the recirculation zone (L_{max}/D) depends on the square prism's aspect ratio. Here, the maximum length of this zone is defined as the maximum streamwise location where the streamwise velocity component is zero. For AR = 5, the mean recirculation zone extends downstream to a maximum of 6.3*D*. For AR = 7 and 9, the recirculation zone extends to 7.5*D* and 8.4*D*, respectively. The streamwise extent of the recirculation zone also varies along the height of the finite square prism. The length of the recirculation zone decreases when moving from the ground plane to the free end of the square prism. This indicates that the effect of downwash is maximum near the free end of the prism and reduces when moving towards the the ground plane. Data for the finite cylinder from Sumner et al. (2004) are also shown in Figure 4.2, which show that the finite-cylinder recirculation zones are shorter than those of the finite square prism.

Finite Square Prism

Finite Cylinder

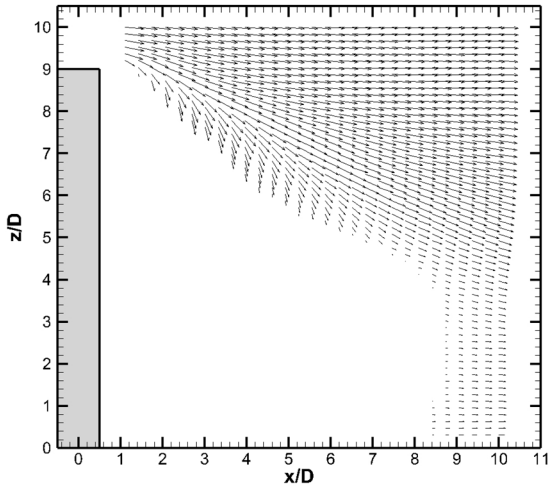

(a) AR = 9

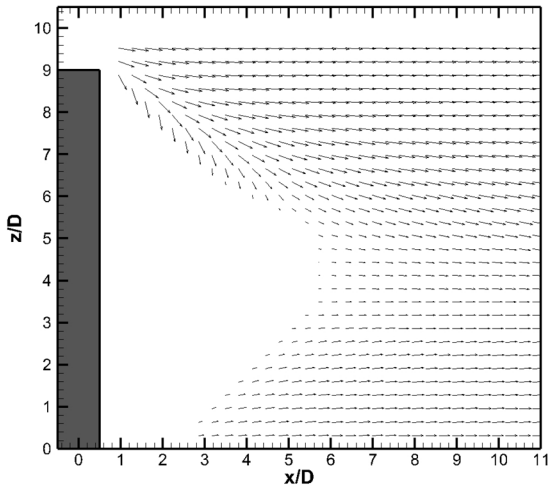

(d) AR = 9

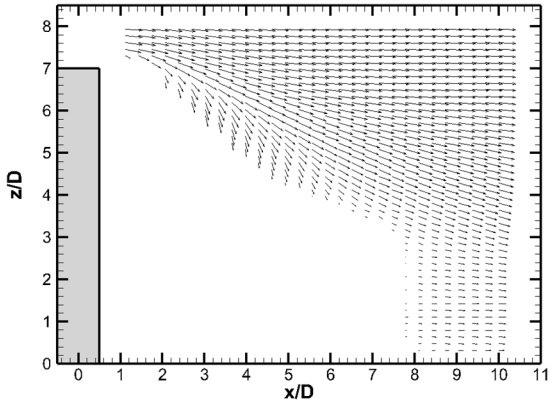

(b) AR = 7

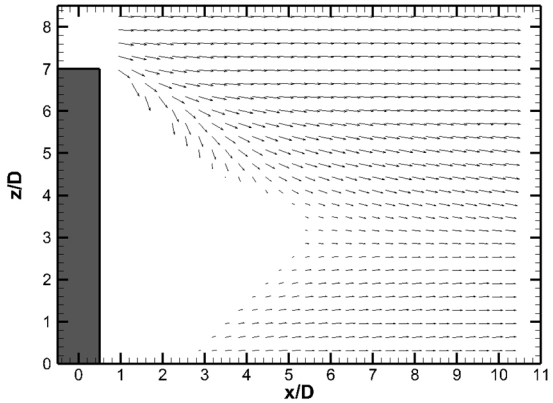

(e) AR = 7

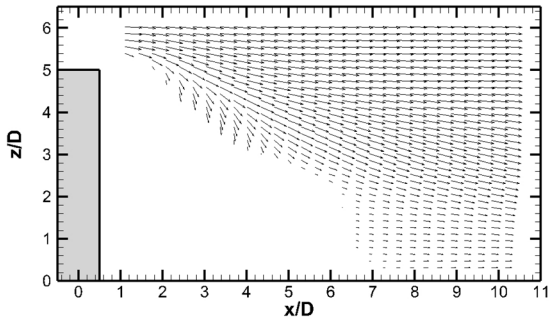

(c) AR = 5

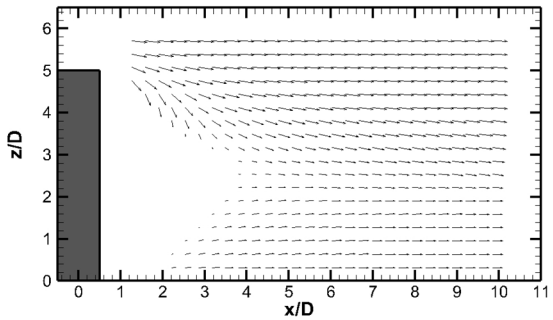

(f) AR = 5

Figure 4.1: Time-averaged velocity field (velocity components u and w) along the wake centreline ($y/D = 0$) for finite square prisms of (a) AR = 9, (b) AR = 7 and (c) AR = 5 at $\alpha = 0°$ (from the present experiments, $Re = 3.7\times10^4$) and finite cylinders of (d) AR = 9, (e) AR = 7, and (f) AR = 5 (from Sumner et al. (2004), $Re = 6\times10^4$).

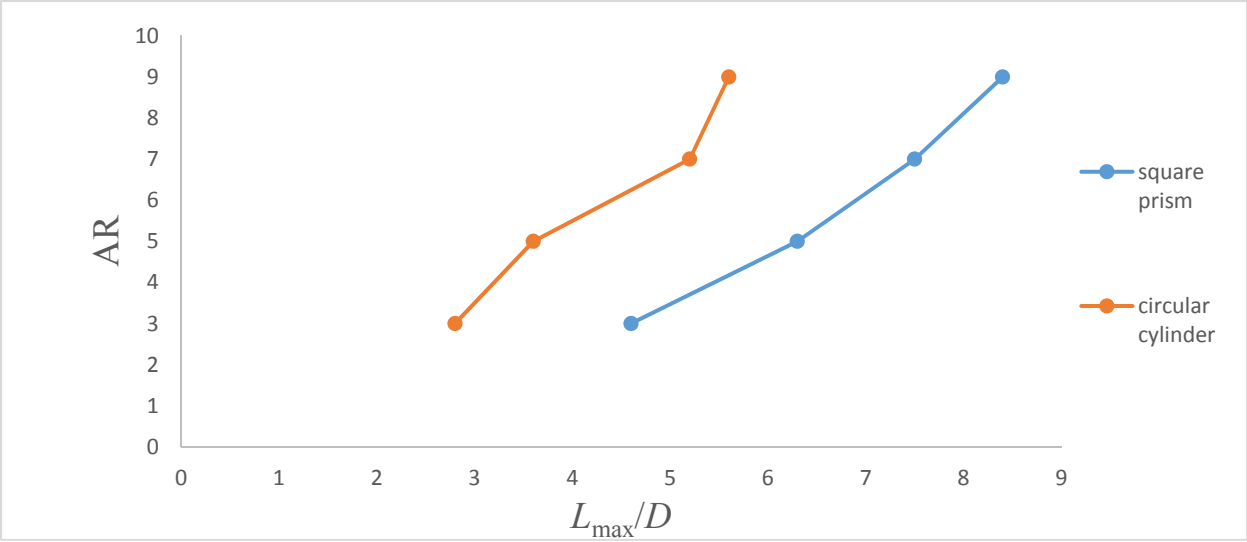

Figure 4.2: Maximum streamwise length of the recirculation zone (L_{max}/D) for the finite square prism at $\alpha = 0°$ (present experiments) and finite cylinder (from Sumner et al. (2004)). Finite square prism data for AR = 3 are taken from Ogunremi and Sumner (2015a).

4.3 Flow in the Vertical Plane Normal to the Incident Flow (*y*-*z* Plane)

Time-averaged cross-stream velocity fields, in the *y*-*z* plane (showing velocity components *v* and *w*), at a distance of $x/D = 10$, are shown in Figure 4.3, alongside similar velocity fields for a finite cylinder from Sumner et al. (2004). For both the prism and the cylinder, the recirculating flow in the upper part of the wake on either side of the centreline shows the nominal locations of the time-averaged streamwise tip vortices. The tip vortices consist of a pair of counter-rotating vortices in the upper part of the wake region. This counter-rotating vortex pair exists in a symmetric arrangement for all the aspect ratios at $\alpha = 0°$. The counter-rotating vortex pair induces strong downwash (downward-directed velocity) on the wake centreline that reaches the ground plane. The centre of the vortex pair appears to be slightly closer to the ground plane for the finite square prism compared to the finite cylinder.

For the square prism of AR = 9 (Figure 4.3a), the velocity vector field shows stronger downwash behind the square prism and below the tip compared to the prisms of AR = 7 and 5 (Figures 4.3b,c). The downwash weakens along the axis of the prism towards the ground plane and the remaining flow is directed towards the downstream direction. The corresponding time-averaged streamwise vorticity fields for the finite square prisms of AR = 9, 7 and 5 at $x/D = 10$, as well as the finite cylinders from Sumner et al. (2004), are shown in Figure 4.4, where the

streamwise vorticity is expressed in dimensionless form as $\omega_x D/U_\infty$. A symmetric counter-rotating pair of streamwise vortices, representing the tip vortices, is seen in the upper part of the wake for all aspect ratios and for both the prism and the cylinder. The vorticity concentrations representing the tip vortices are reasonably circular in shape and remain as two distinct structures.

The tip vortex structures are more circular for the finite square prism of AR = 5 (Figure 4.4c). Unlike the finite cylinders, however, the base vortex structures are nearly absent at x/D = 10 in the lower part of the wake for the square prisms. The base vortex structures are responsible for the upwash flow. The present experiments clearly identify that there is no significant upwash for the finite square prism at x/D = 10, which is consistent with the absence of base vortices. However, Sumner et al. (2004) identified that the base and tip vortices weaken with the increase in distance downstream from the cylinder. The present experiments were carried out at a distance of 10D from the centre of the prism for the y-z plane. It is possible, therefore, that the base vortices of the square prism may have weakened and diffused by x/D = 10; additional experiments closer to the prism may confirm the existence of the base vortices.

Additionally, smaller vorticity concentrations are seen at the outer edges of the square prism wake close to the ground plane, which may represent the trailing arms of the horseshoe vortex system originating upstream from the prism within the boundary layer. These horseshoe vortices are not seen in the finite cylinder data obtained by Sumner et al. (2004). Their absence may be caused by the size of their measurement plane, which did not extend as close to the ground plane for the finite cylinder experiments. Also, the horseshoe vortex is known to be weaker for a cylinder compared to a prism, and the horseshoe vortex arms from the cylinder may have diffused or weakened by x/D = 10.

The centres of the tip vortices are observed to be near the mid-height of the prism. Thus, the location of the vortex centre is a function of the aspect ratio of the prism and is approximately equal to 0.56H. Also, the centres of the horseshoe vortex pairs move closer towards the prism with the increase in aspect ratio from AR = 5 to 9.

Finite Square Prism

Finite Cylinder

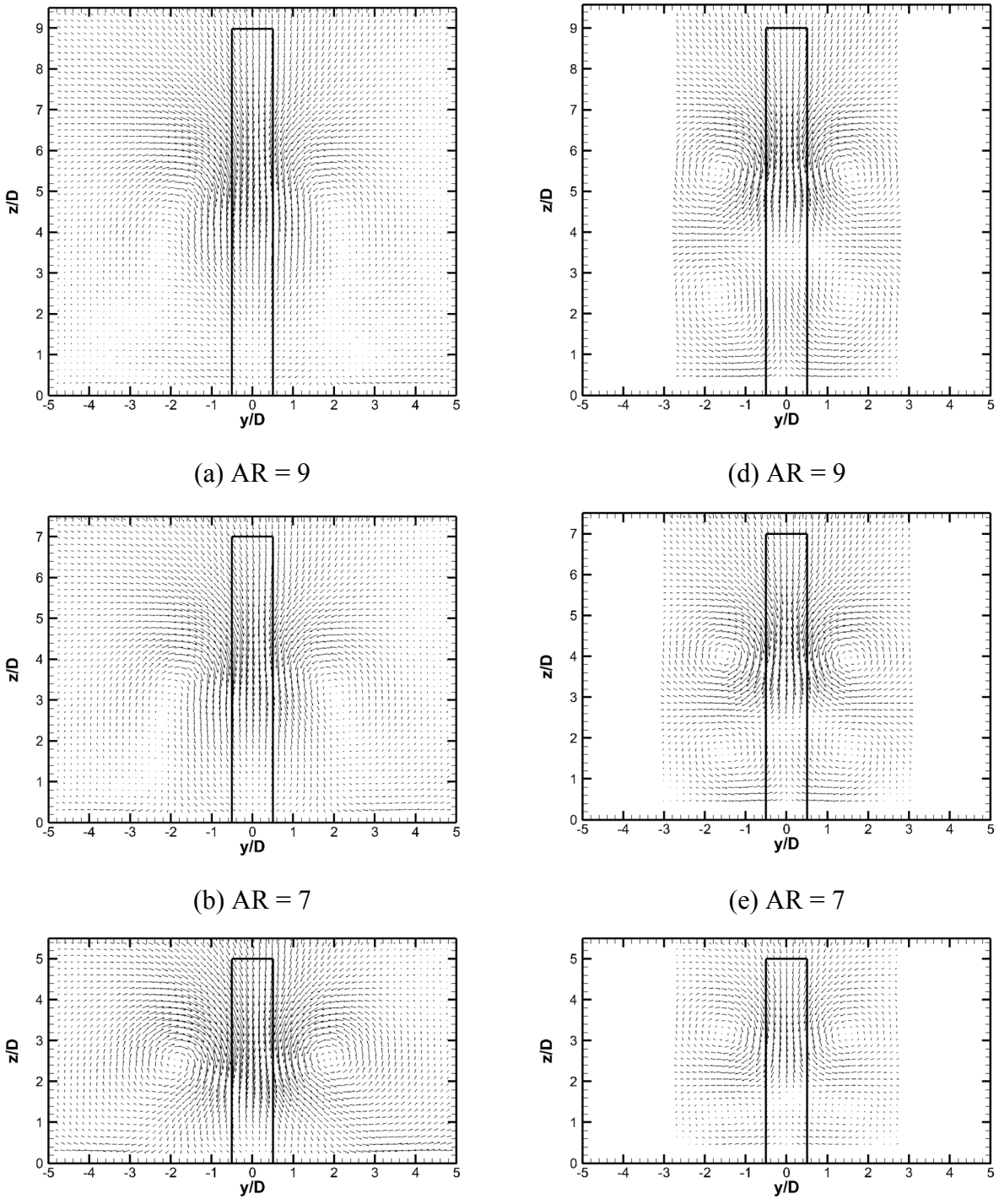

(a) AR = 9

(d) AR = 9

(b) AR = 7

(e) AR = 7

(c) AR = 5

(f) AR = 5

Figure 4.3: Time-averaged velocity field (velocity components v and w) in the cross-stream vertical plane at $x/D = 10$ for finite square prisms of (a) AR = 9, (b) AR = 7 and (c) AR = 5 at $\alpha = 0°$ (from the present experiments, $Re = 3.7\times10^4$), and finite cylinders of (d) AR = 9, (e) AR = 7, and (f) AR = 5 (from Sumner et al. (2004), $Re = 6\times10^4$).

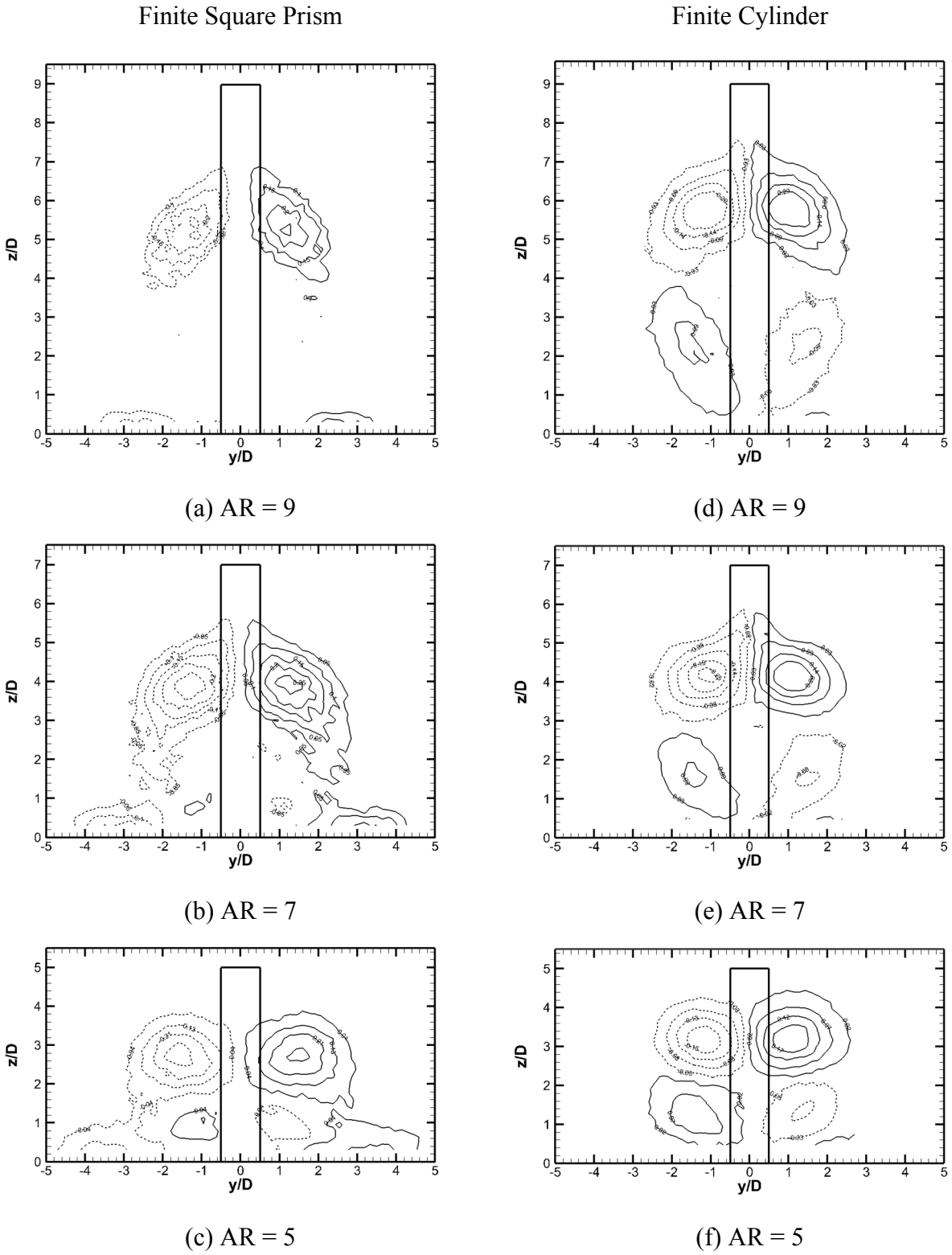

Figure 4.4: Time-averaged streamwise vorticity field (contours of $\omega_x D/U_\infty$) in the cross-stream vertical plane at $x/D = 10$ for finite square prisms of (a) AR = 9, (b) AR = 7 and (c) AR = 5 at $\alpha = 0°$ (from the present experiments, Re = 3.7×10^4) and finite cylinders of (d) AR = 9, (e) AR = 7, and (f) AR = 5 (from Sumner et al. (2004), Re = 6×10^4). Solid contour lines represent positive (CCW) vorticity, dashed contour lines represent negative (CW) vorticity.

4.3.1 Streamwise Mean Velocity

Contours of the mean streamwise velocity component (u/U_∞) at $x/D = 10$ for finite-square prisms at zero incidence angle ($\alpha = 0°$) are shown in Figure 4.5, alongside similar velocity fields for finite cylinders from Sumner et al. (2004). These contours can be used to judge the width and vertical extent of the mean wake behind the prism. The maximum width of the wake was calculated at mid-height of the prism where the streamwise velocity component u/U_∞ reaches 0.95.

For all these aspect ratios (AR = 9, 7 and 5), the wake exhibits symmetry at $\alpha = 0°$ for both square prisms and cylinders. The maximum width of the wake increases with a reduction in AR, increasing from approximately 5.2D for AR = 9 (Figure 4.5a), to 6D for AR = 7 (Figure 4.5b), and to 6.8D for AR = 5 (Figure 4.5c).

The minimum streamwise velocity encountered in the wake, $(u/U_\infty)_{min}$, decreases with an increase in aspect ratio, i.e., from $(u/U_\infty)_{min} = 0.53$ for the prism of AR = 3 (from the results of Ogunremi and Sumner (2015a)), to $(u/U_\infty)_{min} = 0.35$ for the prism of AR = 5, to $(u/U_\infty)_{min} = 0.32$ for the prism of AR = 7, and to $(u/U_\infty)_{min} = 0.27$ for the prism of AR = 9. The maximum thickness of the wake (based on the vertical extent of the $u/U_\infty = 0.95$ contour) relative to the prism height, increases as the aspect ratio is lowered, increasing from 0.7H for AR = 9 (Figure 4.5a) to 0.8H for both AR = 7 (Figure 4.5b) and AR = 5 (Figure 4.5c). A similar trend is seen for the finite cylinder wake in Figures 4.5d,e,f.

The magnitude of $(u/U_\infty)_{min}$ can be related to the mean drag coefficient acting on the square prism (see the data in Figure 2.19). For finite square prisms of different aspect ratio (AR = 3, 5, 7 and 9), the lowest mean drag force coefficient (C_D) was 1.29 (AR = 3) which corresponds also to the maximum value of $(u/U_\infty)_{min}$. Also there is a significant increase in the drag coefficient value from $C_D = 1.29$ (AR = 3) to $C_D = 1.43$ (AR = 5). Similarly, the magnitude of $(u/U_\infty)_{min}$ also exhibits a reduction from 0.53 (AR = 3) to 0.35 (AR = 5).

4.3.2 Cross-stream Mean Velocity

Time-averaged cross-stream velocity fields (v/U_∞) in the cross-stream (y-z) plane for finite square prisms at zero incidence angle ($\alpha = 0°$) are shown as contour plots in Figure 4.6. The results obtained are compared with the data obtained from Sumner at al. (2004) for finite circular cylinders. For all three square prisms (Figures 4.6a,b,c), the flow is entrained towards the wake centerline in the upper part of the wake. Only for the prism of AR = 5 (Figure 4.6c) is there

appreciable flow moving away from the centreline in the lower part of the wake. For the cylinders (Figures 4.6d,e,f), however, the entrainment occurs towards the wake centerline in two different zones, which correspond to the tip vortex region and the base vortex region.

4.3.3 Wall-normal Mean Velocity

Time-averaged wall-normal velocity fields (w/U_∞) in the cross-stream (y-z) plane of the finite square prisms, along with data obtained from Sumner et al. (2004) for finite cylinders, are shown as contour plots in Figure 4.7. All of the data were obtained at $x/D = 10$. For all three square prisms (Figures 4.7a,b,c), there exists a strong region of downwash velocity on the wake centreline. No significant upwash is seen for the prisms. In contrast, for the finite cylinders (Figures 4.7d,e,f), a small region of upwash is located near the ground plane.

Finite Square Prism

Finite Cylinder

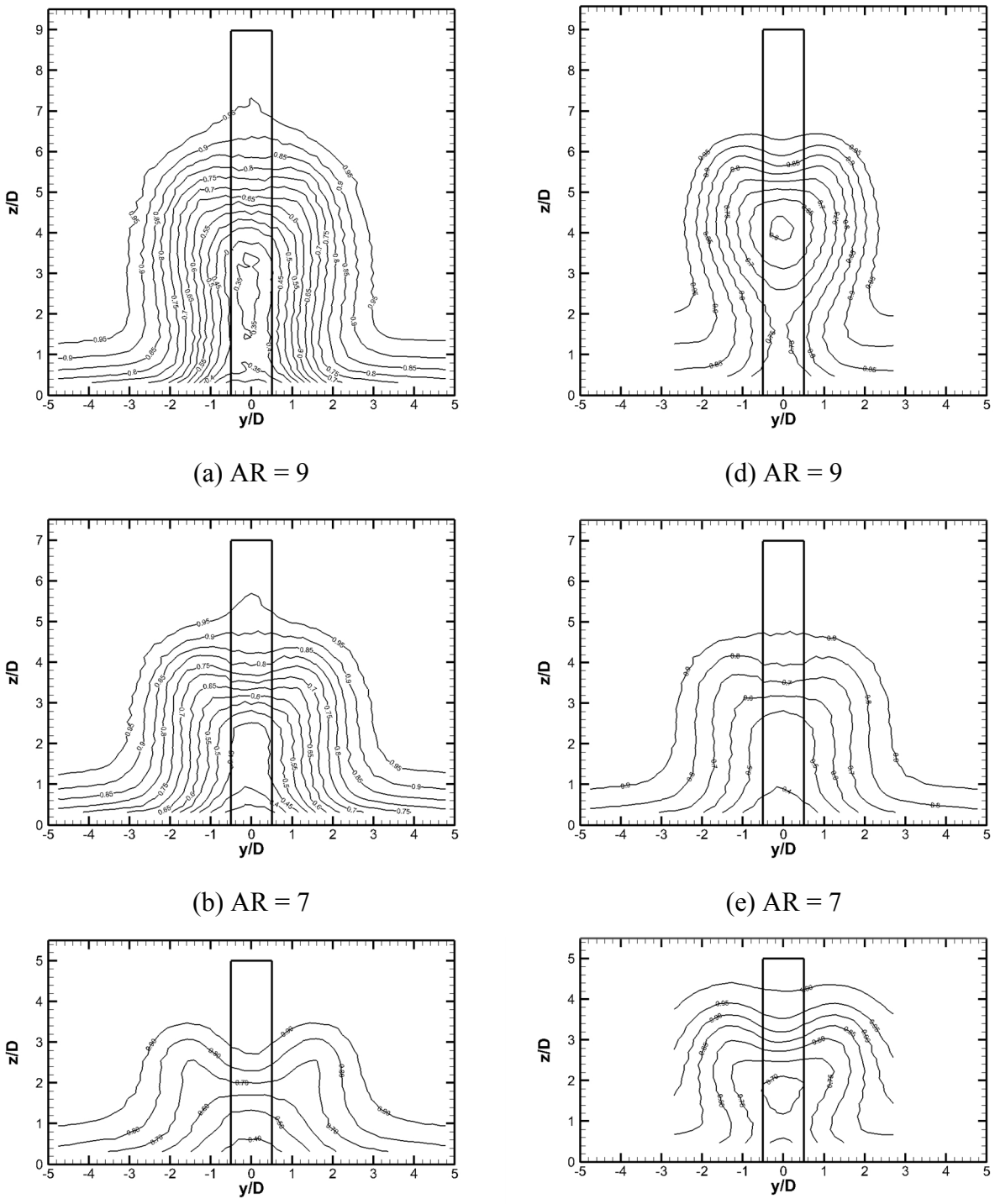

(a) AR = 9

(d) AR = 9

(b) AR = 7

(e) AR = 7

(c) AR = 5

(f) AR = 5

Figure 4.5: Streamwise mean velocity contours in the wake of finite square prisms of (a) AR = 9, (b) AR = 7 and (c) AR = 5 at α = 0° (from the present experiments, Re = 3.7×10^4) and finite cylinders of (d) AR = 9, (e) AR = 7, and (f) AR = 5 (from Sumner et al. (2004), Re = 6×10^4).

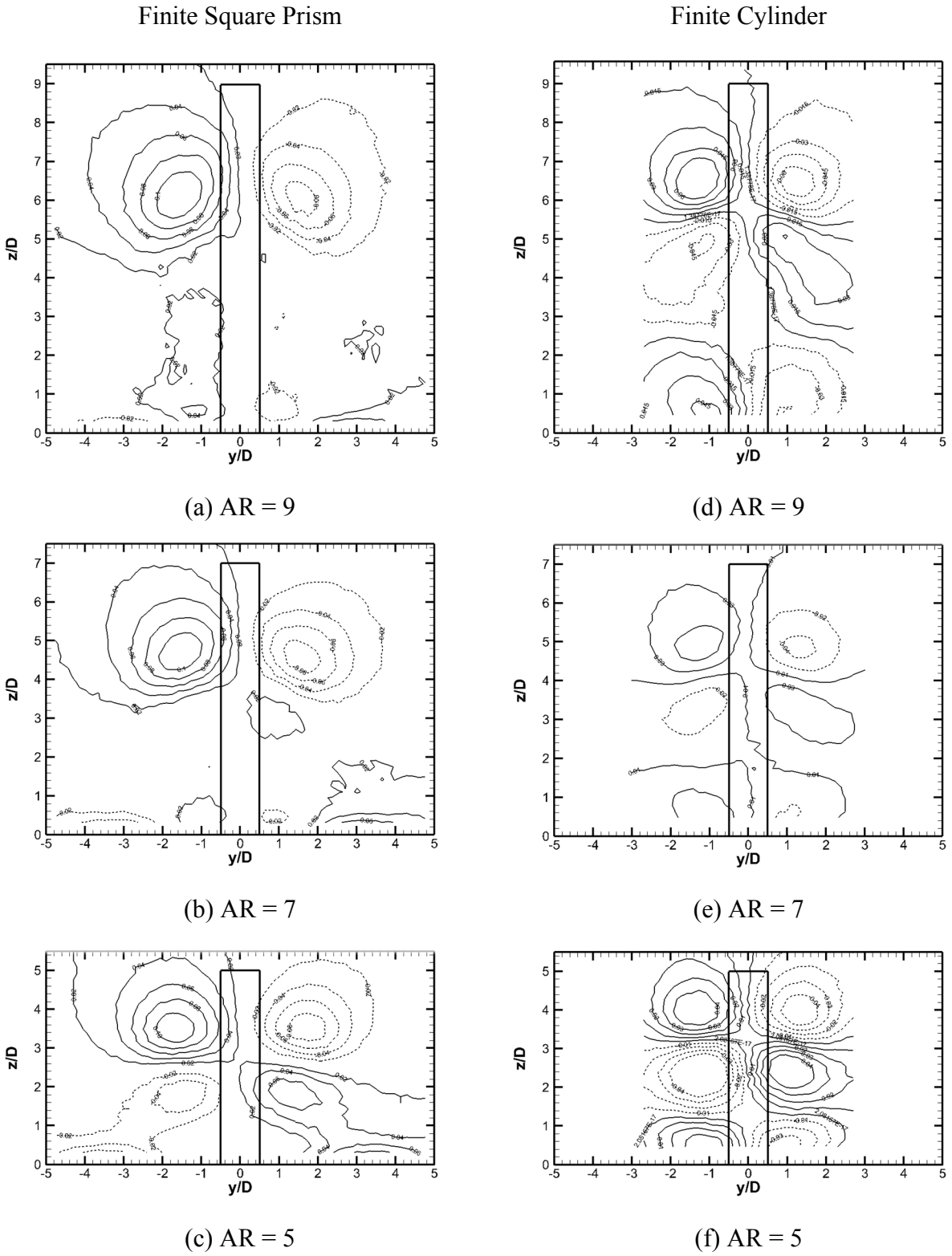

Figure 4.6: Cross-stream mean velocity contours at $x/D = 10$ of the finite square prisms of (a) AR = 9, (b) AR = 7, and (c) AR = 5, and finite cylinders (from Sumner et al. (2004)) of (d) AR = 9, (e) AR = 7, and (f) AR = 5. Solid contour lines represent positive cross-stream velocity (in the $+y$ direction), dashed contour lines represent negative cross-stream velocity (in the $-y$ direction).

Finite Square Prism

Finite Cylinder

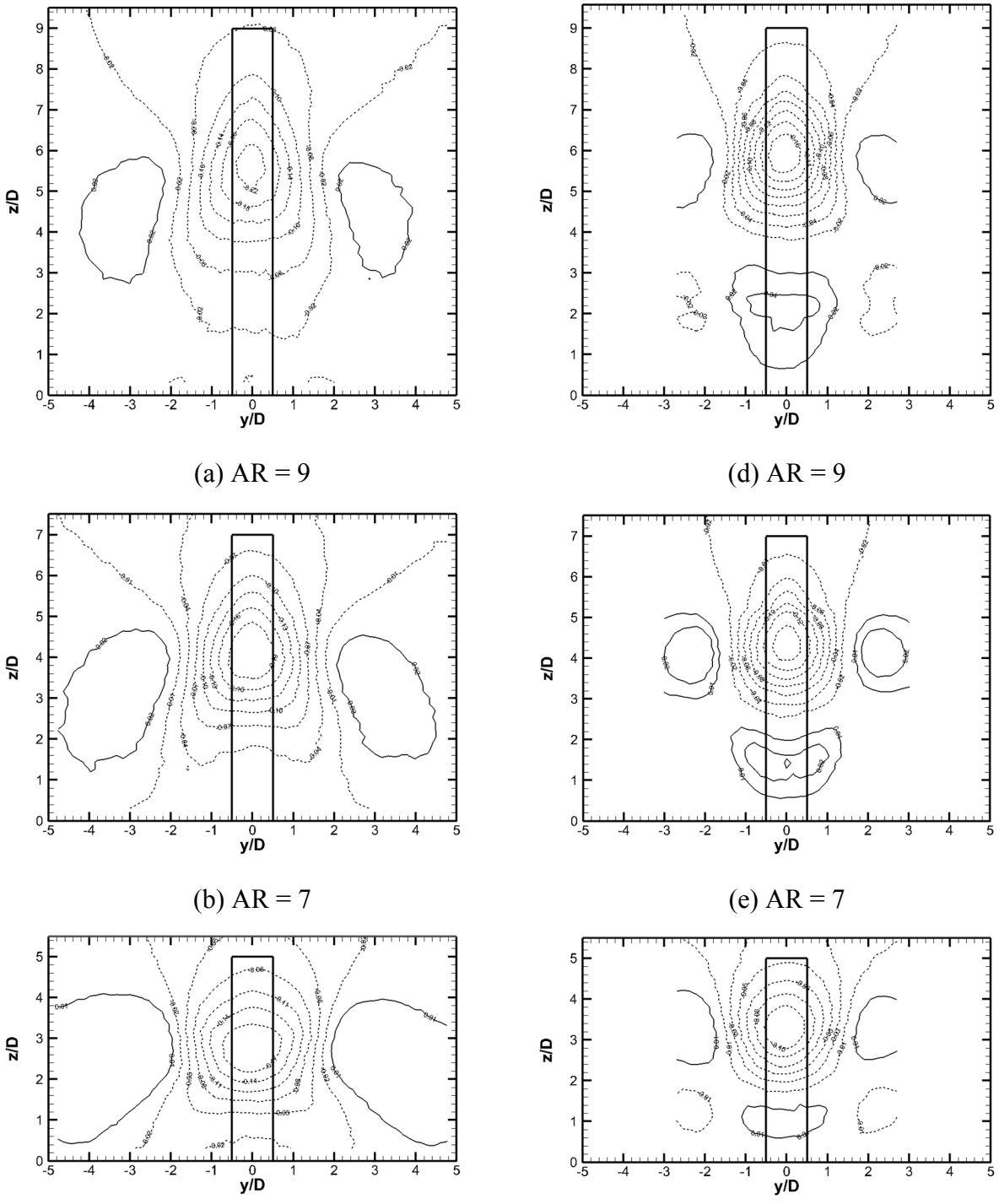

(a) AR = 9

(d) AR = 9

(b) AR = 7

(e) AR = 7

(c) AR = 5

(f) AR = 5

Figure 4.7: Wall-normal mean velocity contours at $x/D = 10$ of the finite square prisms of (a) AR = 9, (b) AR = 7, and (c) AR = 5, and finite cylinders (from Sumner et al. (2004)) of (d) AR = 9, (e) AR = 7, and (f) AR = 5. Solid contour lines represent positive wall-normal velocity (in the $+z$ direction), dashed contour lines represent negative wall-normal velocity (in the $-z$ direction).

CHAPTER 5. EFFECTS OF INCIDENCE ANGLE

5.1 Introduction

In this chapter, the effects of incidence angle are discussed for the finite square prisms oriented at incidence angles ranging from $\alpha = 0°$ to 45°. At $\alpha = 0°$, where the prism face is oriented normal to the approaching flow, flow separation occurs symmetrically from the two vertical leading edges (the upstream corners of the square cross-secton) of the prism. As α is changed, the positions of these two leading edges (or corners) change with respect to the approaching flow. This results in changes in the boundary layers on the sides of the prism, the development of the two separated shear layers, and the wake. The wake becomes asymmetric with the change in incidence angle until symmetry is reacquired at $\alpha = 45°$.

The time-averaged wake velocity measurements at the different incidence angles were taken in two vertical planes, oriented in the streamwise (x-z) and cross-stream (y-z) directions, for surface-mounted finite square prisms of AR = 9, 7 and 5. The experiments were carried out at a Reynolds number of $\mathrm{Re} = 3.7 \times 10^4$ and a relative boundary layer thickness of $\delta/D = 1.5$. In this chapter, the results obtained for AR = 9 are explained in detail, whereas the results for AR = 7 and AR = 5 receive less extensive discussion except where there are significant differences compared to the case of AR = 9.

5.2 Flow in the Vertical Plane Parallel to the Incident Flow (x-z Plane)

The time-averaged wake velocity fields of the finite prism of aspect ratio AR = 9, in the vertical symmetry plane on the centreline of the wind tunnel test section (corresponding to $y/D = 0$), are shown in Figure 5.1. The velocity field is made dimensionless with the freestream velocity, U_∞. For all incidence angles, strong downwash is seen in the upper part of the wake, extending from the region of separated flow above the prism's free end. The downwash eventually reaches the ground plane with no evidence of upwash.

At zero incidence angle ($\alpha = 0°$, Figure 5.1a), the mean recirculation zone extends downstream to a maximum of $x/D = 8.4$ close to the ground plane. When the prism is rotated to $\alpha = 10°$ and 15° (Figures 5.1b,c), there is a small shrinkage in the maximum length of the mean recirculation zone as it now extends only up to $x/D = 6.5$ near the ground plane. From Figure 5.1,

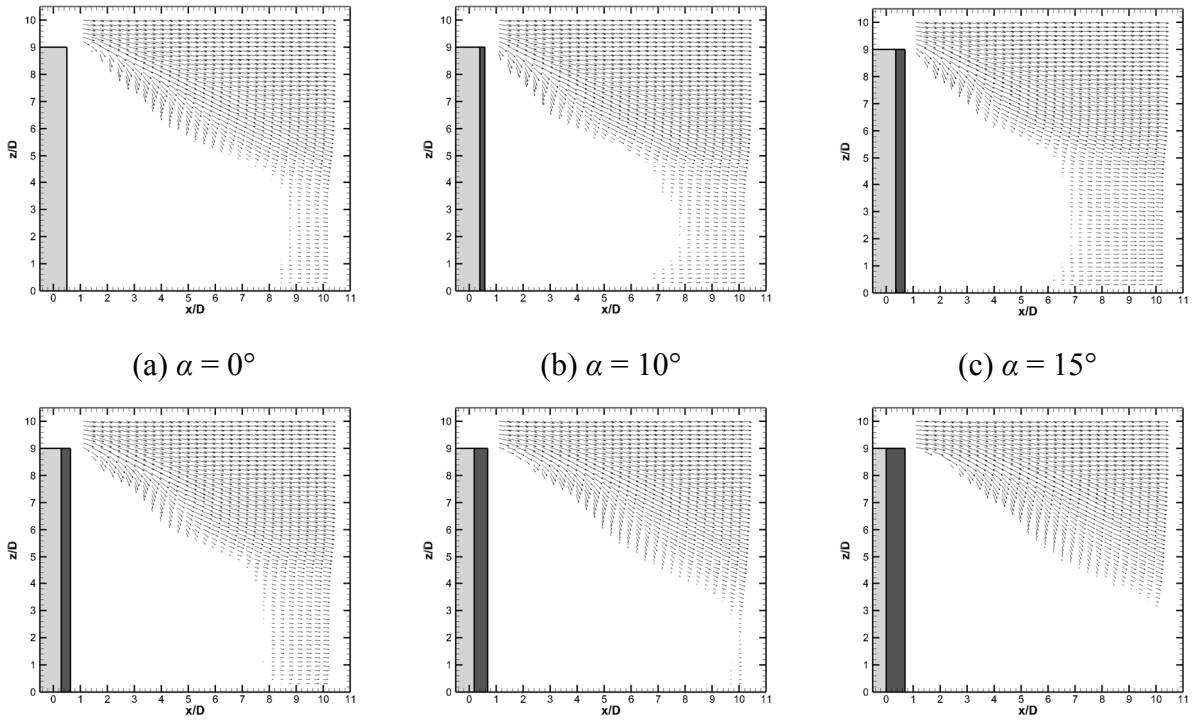

(a) $\alpha = 0°$ (b) $\alpha = 10°$ (c) $\alpha = 15°$

(d) $\alpha = 20°$ (e) $\alpha = 30°$ (f) $\alpha = 45°$

Figure 5.1: Time-averaged velocity field (velocity components u and w) in the vertical plane along the centreline of the wind tunnel ($y/D = 0$) for a finite square prism of AR = 9 for incidence angles ranging from $\alpha = 0°$ to 45°.

it is clear that the shortest recirculation zone appears between 10° and 15°. At $\alpha = 30°$ and $\alpha = 45°$ (Figures 5.1e,f), there is a progressive lengthening of the recirculation zone to $x/D = 9.7$ and $x/D = 10$ near the ground plane, respectively.

Figure 5.2 shows how the maximum length of the recirculation zone depends on the orientation of the square prism. Results are shown for all three aspect ratios. Here, the maximum length of this zone is defined as the maximum streamwise location downstream from the centre of the prism where the streamwise velocity component is zero. With the increase in incidence angle, the recirculation zone shrinks and reaches a minimum value at around $\alpha = 15°$. For AR = 5 and AR = 3, the minimum value lies around $\alpha = 10°$. These incidence angles correspond to the critical incidence angle for the finite prism, where the prism experiences its minimum mean drag coefficient, maximum mean lift coefficient magnitude, and maximum Strouhal number. The different result for AR = 5 and AR = 3 relates to the critical aspect ratio for these experiments, which lies between AR = 5 and AR = 3. For all three aspect ratios, the maximum value for the

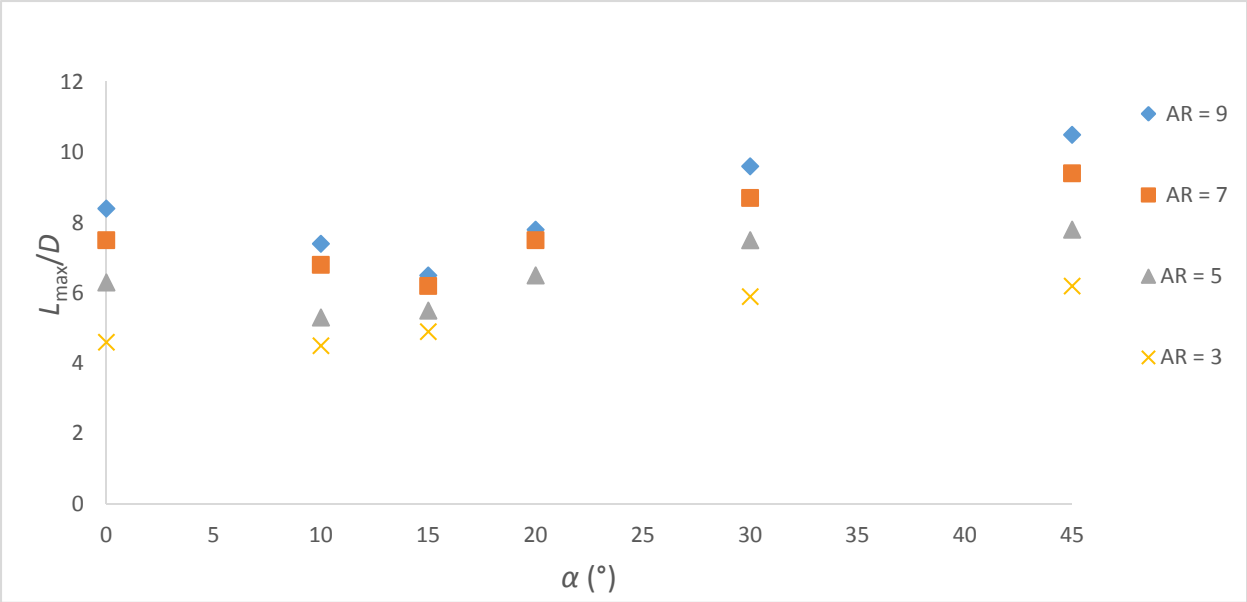

Figure 5.2: Maximum streamwise length of the mean recirculation zone (L_{max}/D) of the finite square prisms for different incidence angles. Finite square prism data for AR = 3 are taken from Ogunremi and Sumner (2015a).

length of recirculation zone is obtained at $\alpha = 45°$. The shapes of the curves in Figure 5.2 closely mirror the behaviour of the mean drag coefficient for the finite square prism shown in Figure 2.17 and discussed by McClean and Sumner (2014).

5.3 Flow in the Vertical Plane Normal to the Incident Flow (*y*-*z* Plane)

Time-averaged cross-stream velocity fields in a vertical plane (*y*-*z*) at $x/D = 10$ for the finite square prism of AR = 9 are shown in Figure 5.3. At zero incidence angle ($\alpha = 0°$) (Figure 5.3a), a symmetric pair of counter-roating vortex structures occur which induce a strong downwash on the wake centreline that reaches the ground plane. As the prism is rotated to $\alpha = 5°$ (Figure 5.3b), the tip vortex pair becomes slightly asymmetric, with the counter-clockwise vortex structure being displaced upwards and the clockwise vortex structure being displaced downwards. This asymmetry becomes stronger as the prism is rotated to $\alpha = 10°$ (Figure 5.3c) and $\alpha = 15°$ (Figure 5.3d). The maximum asymmetry in the tip vortex pair coincides with the critical incidence angle for the prism, which lies between $\alpha = 10°$ and 15° (McClean and Sumner, 2014). When the prism is further rotated to $\alpha = 20°$ and higher (Figures 5.3e,f,g,h), the asymmetry of the recirculating

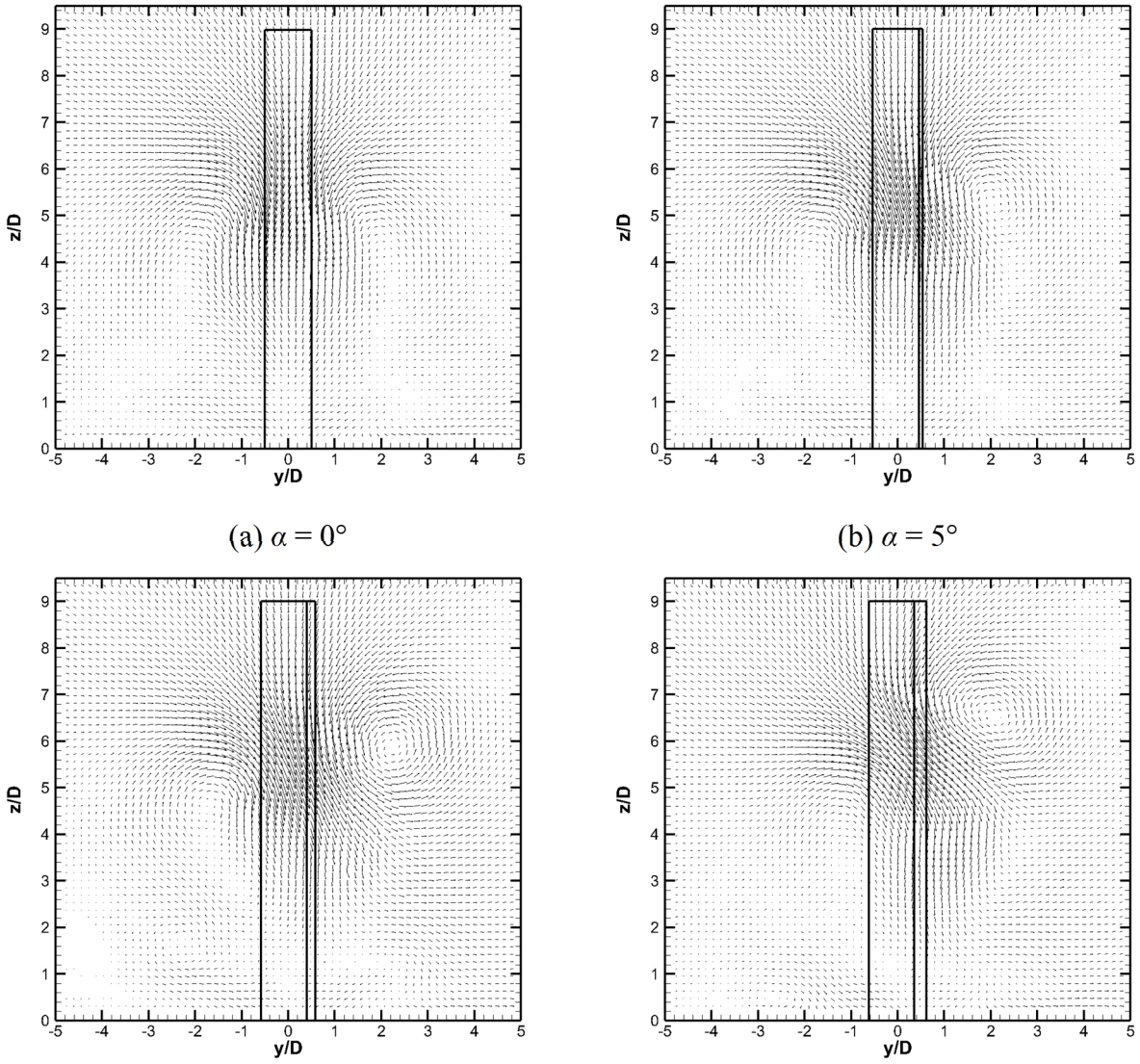

(a) $\alpha = 0°$ (b) $\alpha = 5°$

(c) $\alpha = 10°$ (d) $\alpha = 15°$

Figure 5.3: Time-averaged velocity field (velocity components v and w) in the cross-stream vertical plane at $x/D = 10$ for a finite square prism of AR = 9 for incidence angles ranging from $\alpha = 0°$ to 45°. (Figure continues on the following page.)

flows begins to diminish, until a symmetric arrangement of the tip vortex pair is once again established at $\alpha = 45°$ (Figure 5.3h).

At $\alpha = 45°$ (Figure 5.3h), there is a region near the ground plane where velocity vectors are absent. This absence of velocity vectors means the seven-hole probe was unable to measure the flow, since the local flow angle either exceeded its angular range or the flow was reversing

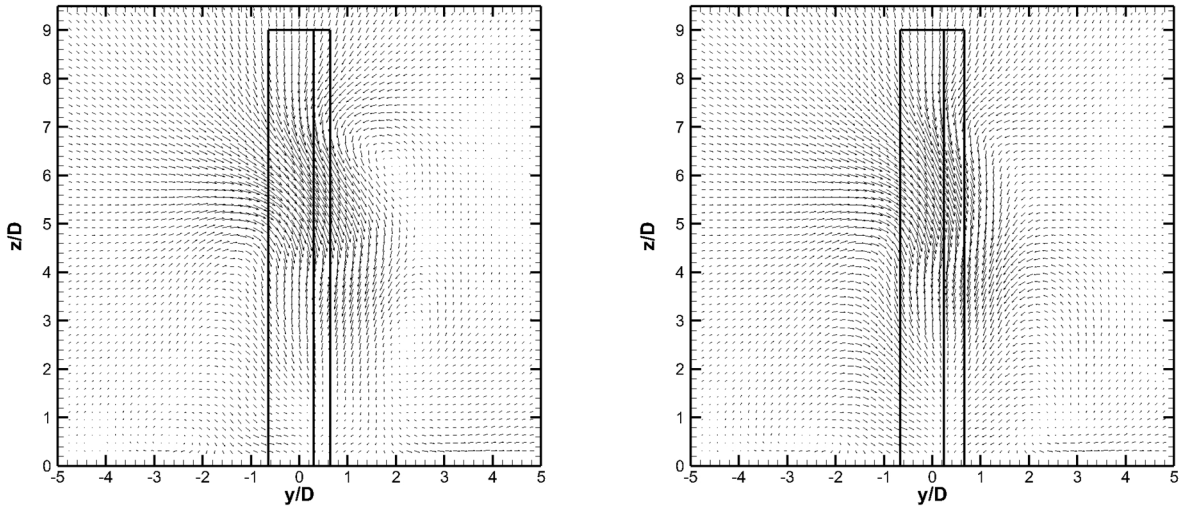

(e) $\alpha = 20°$ (f) $\alpha = 25°$

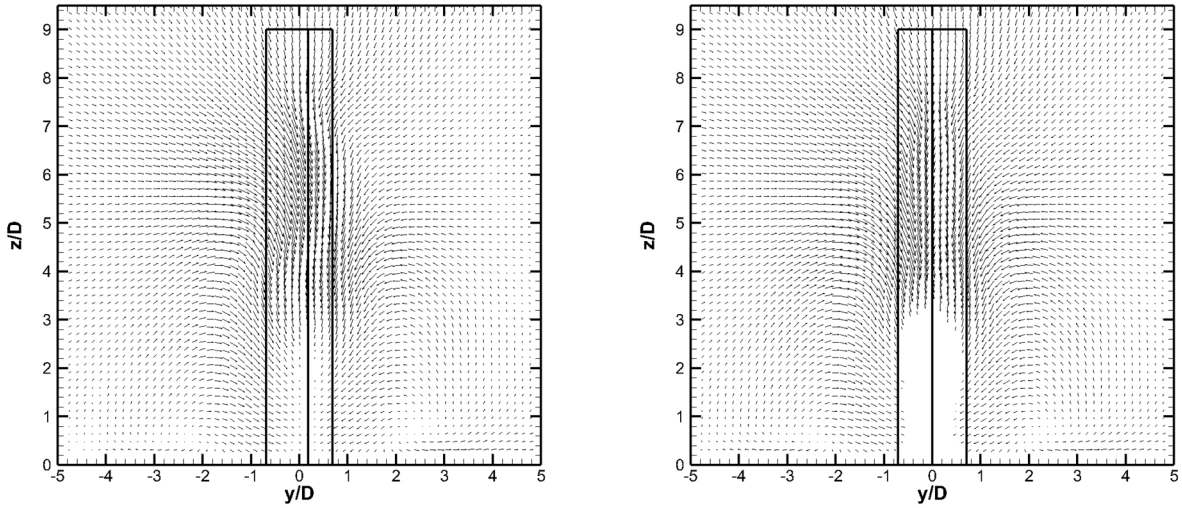

(g) $\alpha = 30°$ (h) $\alpha = 45°$

Figure 5.3 continued.

(Sumner, 2002). In this case, reversing flow was encountered within the mean recirculation zone of the prism.

To better illustrate the tip vortex structures, the mean streamwise vorticity fields at x/D = 10, obtained from the mean velocity vectors in Figure 5.3, are shown in Figure 5.4. The vorticity is expressed in dimensionless form as $\omega_x D/U_\infty$. At α = 0° (Figure 5.4a), a symmetric counter-rotating pair of streamwise vortices, representing the tip vortex pair, is seen in the upper part of the wake. Also, vorticity concentrations are seen close to the ground plane, which represent the

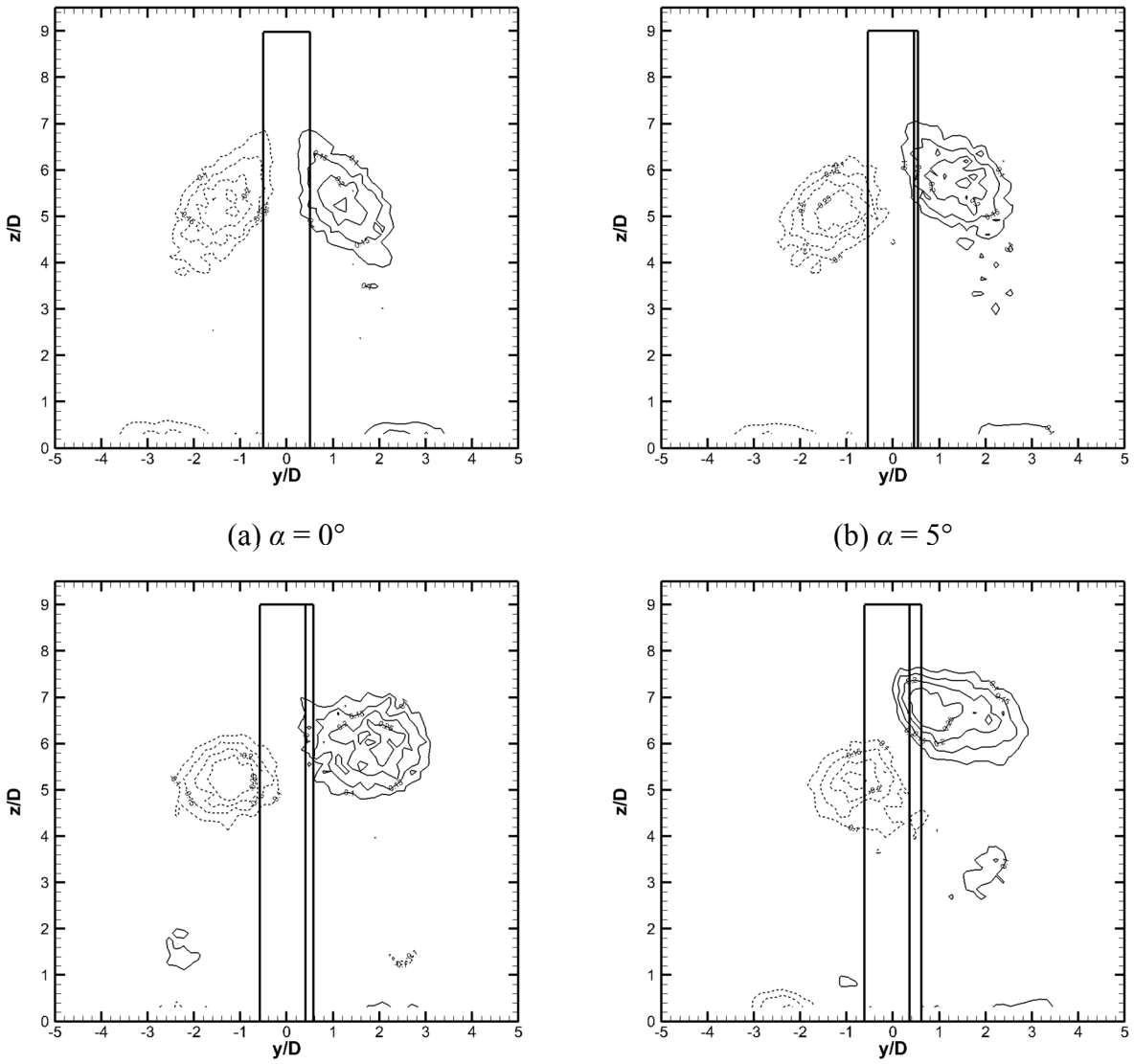

(a) $\alpha = 0°$ (b) $\alpha = 5°$

(c) $\alpha = 10°$ (d) $\alpha = 15°$

Figure 5.4: Time-averaged streamwise vorticity field (contours of $\omega_x D/U_\infty$) in the cross-stream vertical plane at $x/D = 10$ for a finite square prism of AR = 9. Solid lines represent positive (CCW) vorticity, dashed lines represent negative (CW) vorticity. (Figure continues on the following page.)

trailing arms of the horseshoe vortex system orginating upstream of the prism within the ground plane's boundary layer. At $\alpha = 5°$ (Figure 5.4b), the counter-clockwise vortex located on the $+y$ side of the wake moves upward slightly.

Close to the critical incidence angle, between $\alpha = 10°$ (Figure 5.4c) and $\alpha = 15°$ (Figure 5.4d), the CCW tip vortex moves to its highest point above the ground plane, while the CW tip

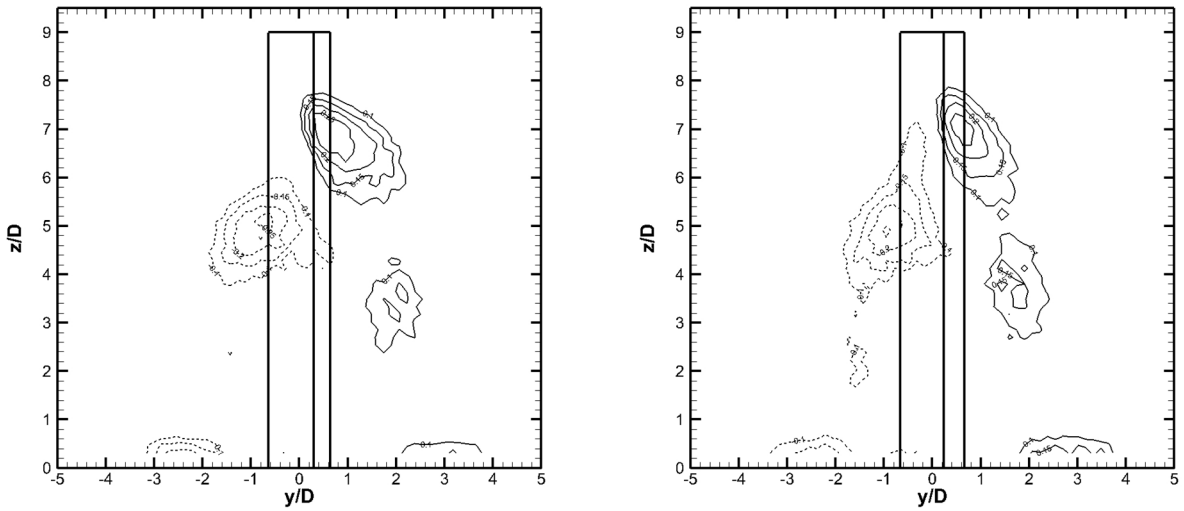

(e) $\alpha = 20°$ (f) $\alpha = 25°$

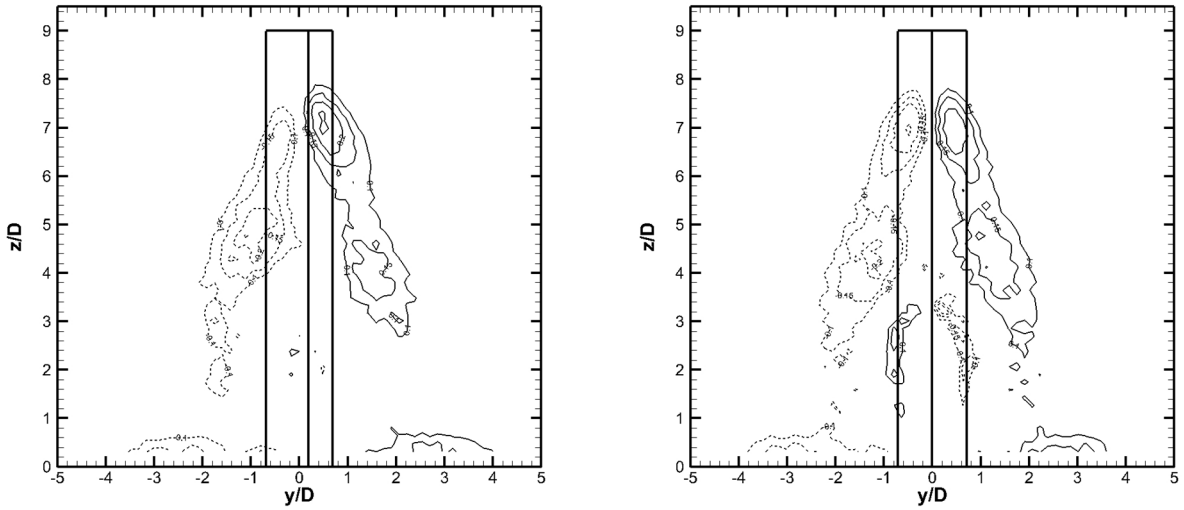

(g) $\alpha = 30°$ (h) $\alpha = 45°$

Figure 5.4 continued.

vortex moves towards the ground plane. In Figure 5.4h, a small pair of counter-rotating pair of vortices behind the prism near the ground plane – these are not real structures but result from the calculation of vorticity at the boundary of the region where the velocity cannot be measured.

Also at $\alpha = 15°$ (Figure 5.4d), it is interesting to note the appearance of second distinct CCW vortex structure on the $+y$ side of the lower half of the wake. With the increase in incidence angle from $\alpha = 20°$ to $45°$ (Figures 5.4e,f,g,h), the second CCW vortex becomes contiguous with main CCW tip vortex. The tip vortices gradually elongate towards the ground plane and for $\alpha =$

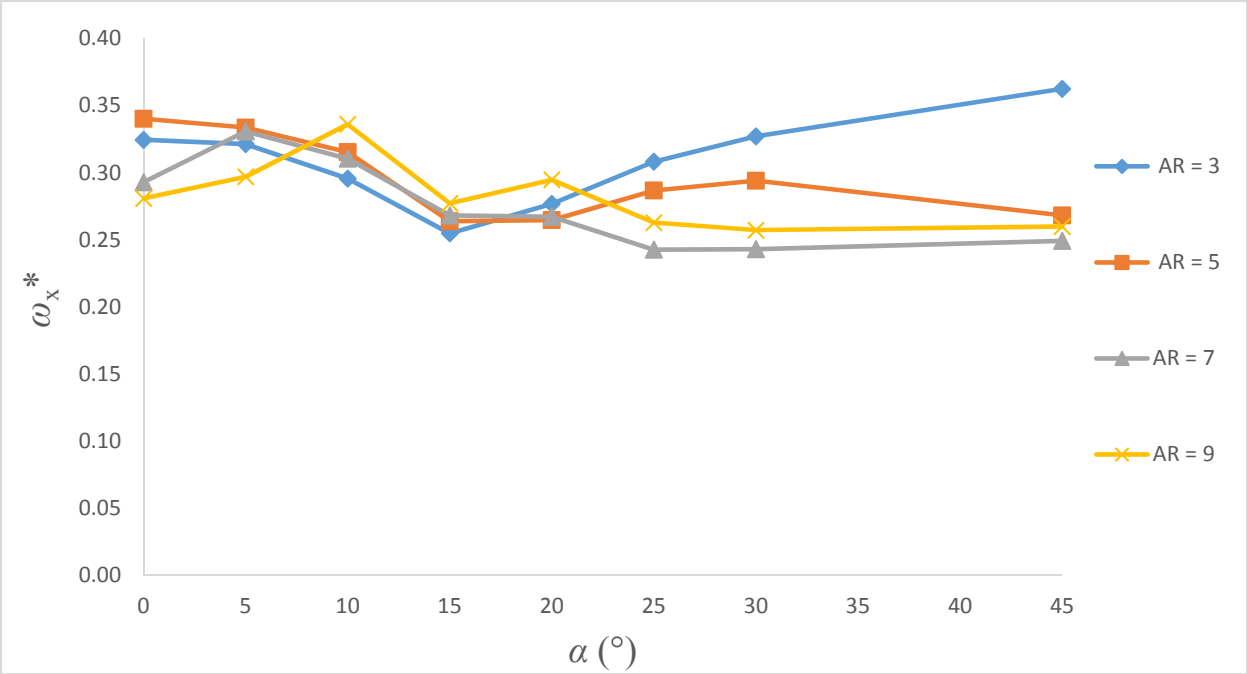

Figure 5.5: Absolute value of minimum CW (most negative) time-averaged streamwise vorticity at $x/D = 10$ for finite square prisms of AR = 3, 5, 7 and 9. Finite square prism data for AR = 3 are taken from Ogunremi and Sumner (2015a).

25° to 45° (Figures 5.4f,g,h) become linked to the vorticity associated with the horseshoe vortex arms.

Figures 5.5 and 5.6 show the variation of minimum and maximum vorticity with incidence angle. The maximum value for CW minimum vorticity (Figure 5.5) is obtained for an incidence angle range α = 0° to 10° (AR = 5, 7 and 9), while for AR =3, the maximum CW vorticity is obtained at α = 45°. The smallest value of minimum CW vorticity lies in the incidence angle range α = 15° to 30° (AR = 3, 5, 7 and 9). The largest value of maximum CCW vorticity data (Figure 5.6) lies in the range of α = 0° to 20° and the smallest value lies in the range α = 10° to 45°.

The minimum value of the streamwise velocity component $(u/U_\infty)_{min}$ in the wake of the finite square prism decreases with aspect ratio for all incidence angles. Figure 5.7 shows the variation of streamwise velocity with incidence angle for finite square prisms of different aspect ratios. The maximum value of $(u/U_\infty)_{min}$ occurs at α = 15° which corresponds to the critical incidence angle for the prism.

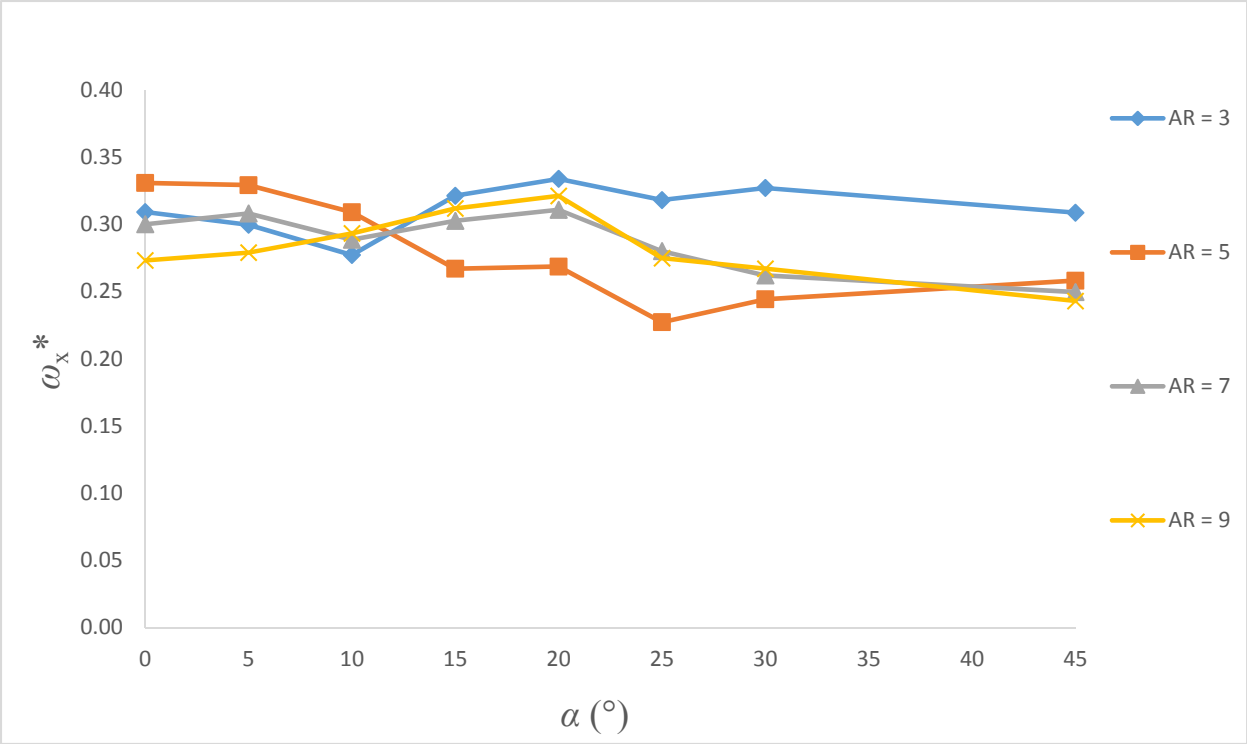

Figure 5.6: Maximum CCW (most positive) time-averaged streamwise vorticity at x/D = 10 for finite square prisms of AR = 3, 5, 7 and 9. Finite square prism data for AR = 3 are taken from Ogunremi and Sumner (2015a).

Contours of the mean streamwise velocity component (u/U_∞) at x/D = 10 are shown in Figure 5.8. These contours can be used to judge the width and vertical extent of the mean wake behind the prism. At α = 0° (Figure 5.8a), the mean wake exhibits a symmetric pattern with a maximum height up to $z = 6D$ above the ground plane and and a width of approximately 5.2D. At α = 5° (Figure 5.8b), small asymmetry is seen in the wake, with a thicker wake region on the +y side of the wake. The wake asymmetry is most prominent near the critical incidence angle, for α = 10° (Figure 5.8c) and α = 15° (Figure 5.8d). At α = 15° (Figure 5.8d), even though the maximum wake height extends to 7D on the +y side of the wake, the width reduces to 4.6D. With a further increase in incidence angle from α = 20° to α = 45° (Figures 5.8e,f,g,h), the asymmetry gradually reduces and the wake reattains a symmetric pattern with a maximum height of 7.4D at α = 45° (Figure 5.8h).

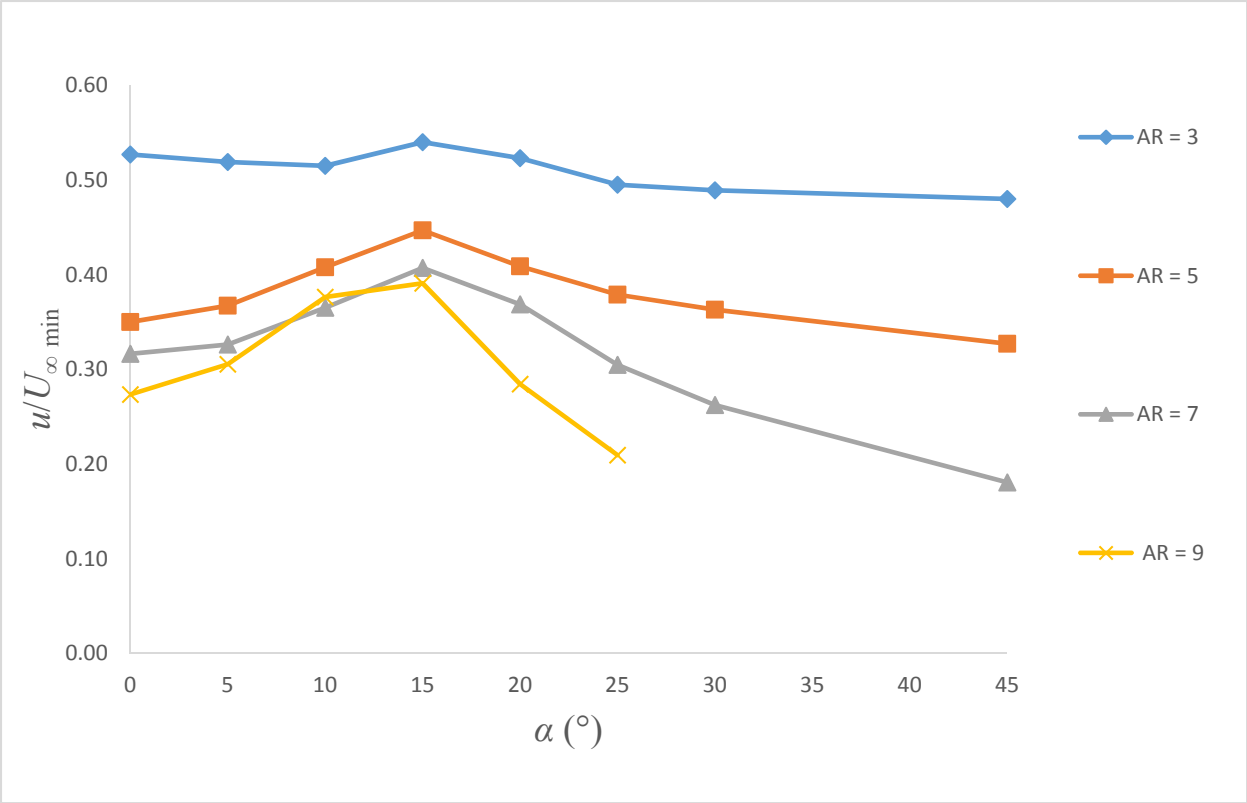

Figure 5.7: Minimum streamwise mean velocity in the wake of the square prisms of AR = 3, 5, 7 and 9, at x/D = 10, for incidence angles ranging from α = 0° to 45°. Finite square prism data for AR = 3 are taken from Ogunremi and Sumner (2015a).

5.3.1 Cross-stream Mean Velocity

Time-averaged cross-stream velocity fields (v/U_∞) in the cross-stream (y-z) plane for the finite square prism of AR = 9 for various incidence angles are shown as contour plots in Figure 5.9. For α = 0° (Figure 5.9a), the flow is entrained towards the wake centerline in the upper part of the wake. A symmetric pattern is obtained at this configuration. With an increase in incidence angle, the flow sweeps across the wake from $-y$ to $+y$, with the strongest sweep of velocity seen for α = 15° (Figure 5.9d). With a further increase in incidence angle to α = 45° (Figure 5.9h), it is observed that entrainment towards the wake centerline, from both sides of the wake, occurs for the entire wake height and the symmetry is regained.

5.3.2 Wall-normal Mean Velocity

Figure 5.10 shows the absolute value of the minimum wall-normal velocity (w/U_∞), or maximum downwash velocity, in the wake of the finite square prisms of AR = 3, 5, 7 and 9 at x/D

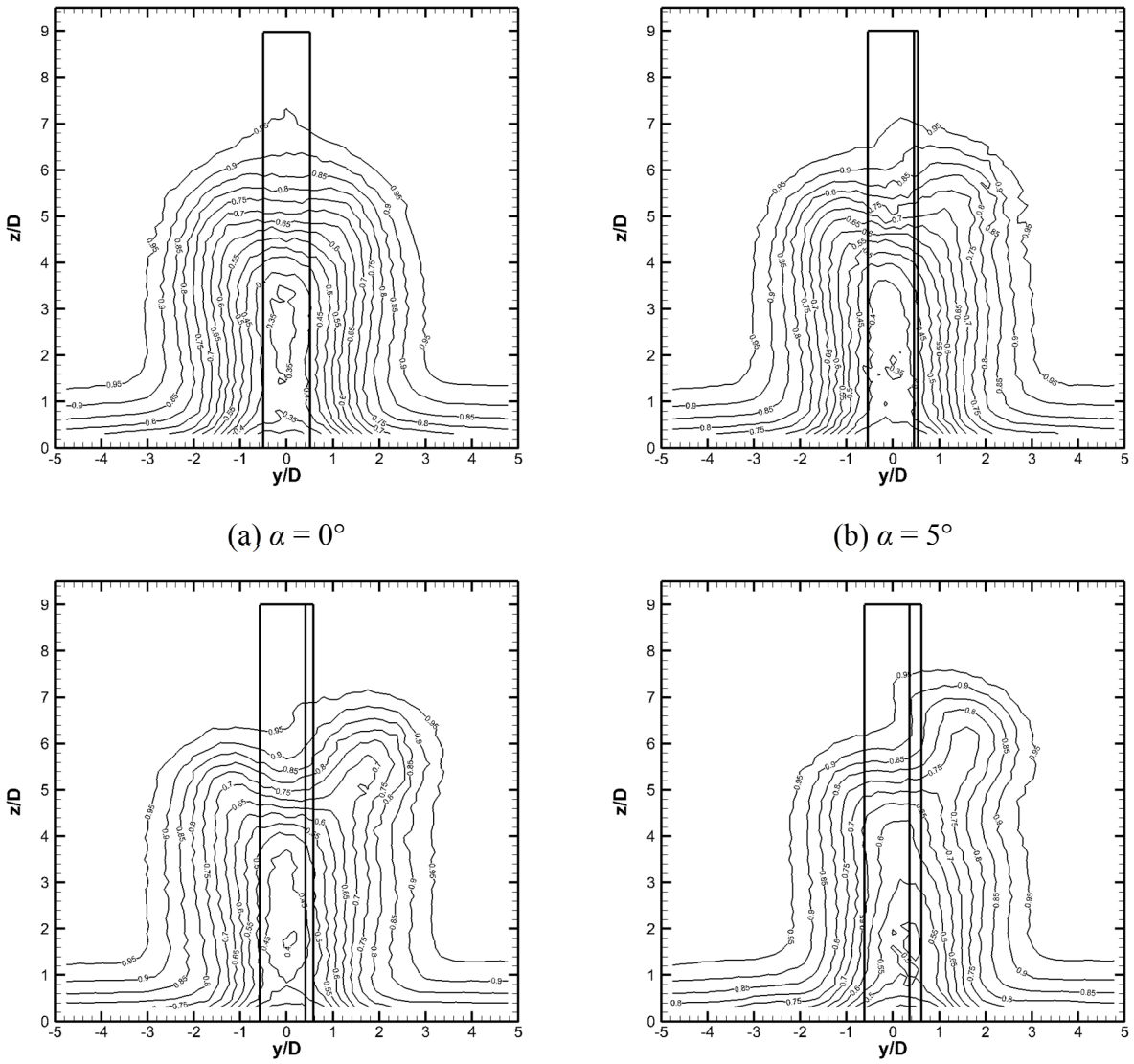

(a) $\alpha = 0°$ (b) $\alpha = 5°$

(c) $\alpha = 10°$ (d) $\alpha = 15°$

Figure 5.8: Streamwise mean velocity contours in the wake of the square prism of AR = 9, at x/D = 10, for incidence angles ranging from $\alpha = 0°$ to 45°. Contour increment of $u/U_\infty = 0.05$. (Figure continues on the following page.)

= 10, for incidence angles ranging from $\alpha = 0°$ to 45°. At $\alpha = 0°$, maximum downwash velocity is obtained for AR = 9 with $w = -0.23U_\infty$ followed by $w = -0.22U_\infty$ for AR = 7, $w = -0.20U_\infty$ for AR = 5 and $w = -0.16U_\infty$ for AR = 3. Also, it is worth mentioning that the rate of decrease of downwash velocity with decrease in aspect ratio increases from AR = 5 to 3.

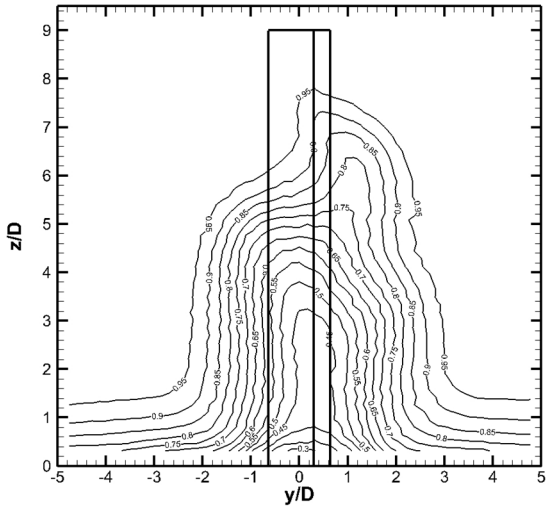

(e) $\alpha = 20°$

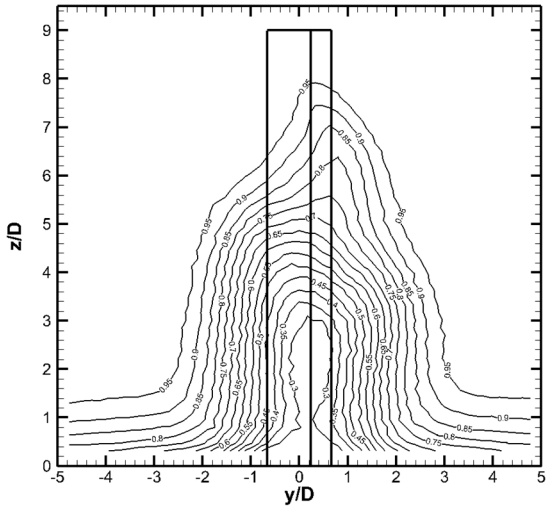

(f) $\alpha = 25°$

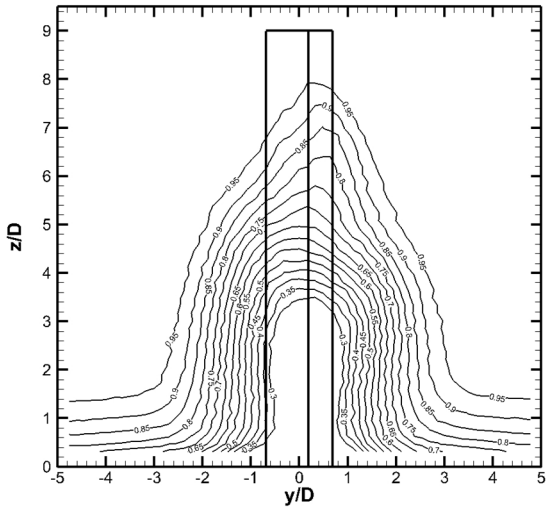

(g) $\alpha = 30°$

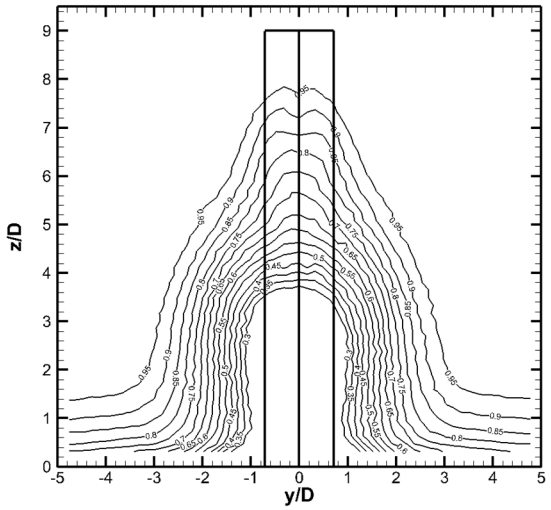

(h) $\alpha = 45°$

Figure 5.8 continued.

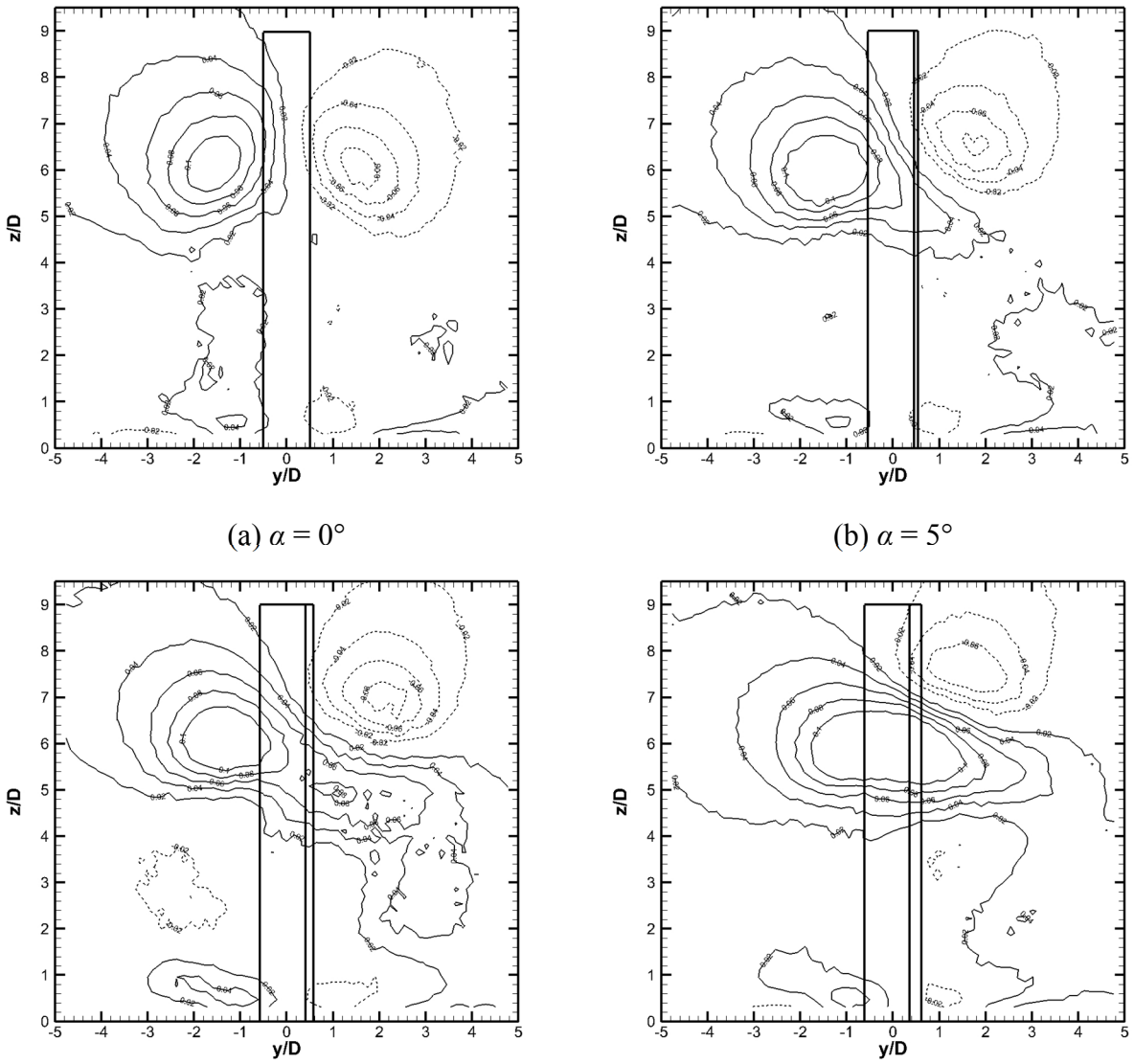

(a) $\alpha = 0°$ (b) $\alpha = 5°$

(c) $\alpha = 10°$ (d) $\alpha = 15°$

Figure 5.9: Cross-stream mean velocity contours in the wake of the square prism of AR = 9, at $x/D = 10$, for incidence angles ranging from $\alpha = 0°$ to 45°. Contour increment of $v/U_\infty = 0.02$. Solid lines represent positive cross-stream velocities, dashed lines represent negative cross-stream velocities. (Figure continues on the following page.)

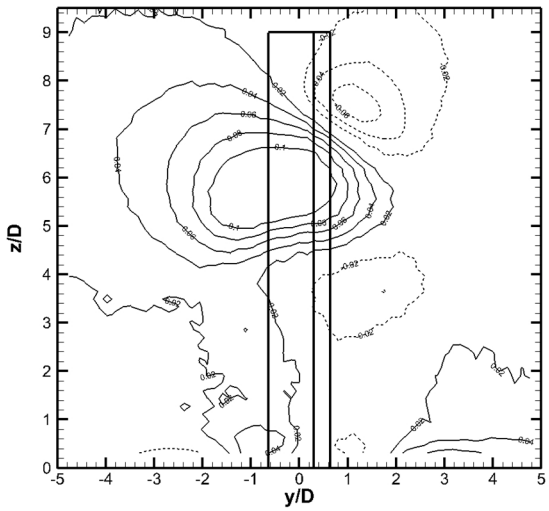

(e) $\alpha = 20°$

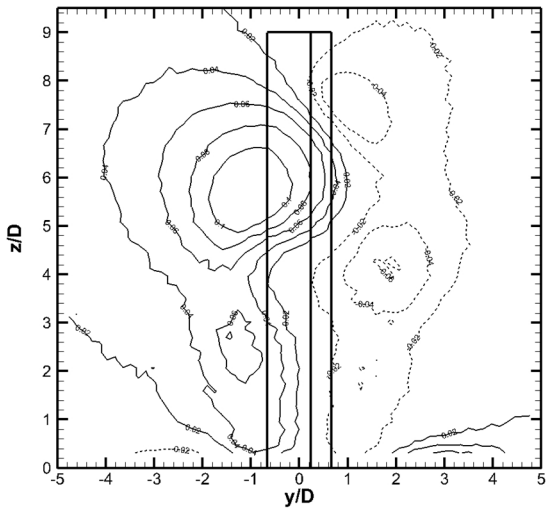

(f) $\alpha = 25°$

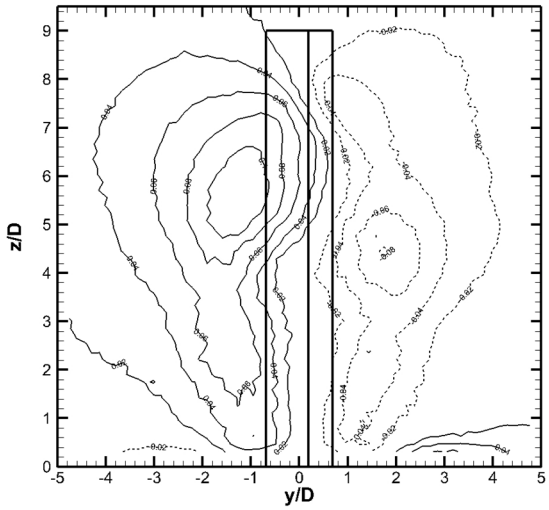

(g) $\alpha = 30°$

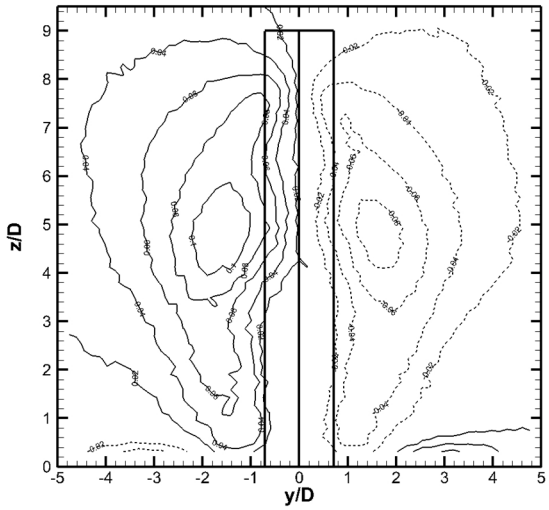

(h) $\alpha = 45°$

Figure 5.9 continued.

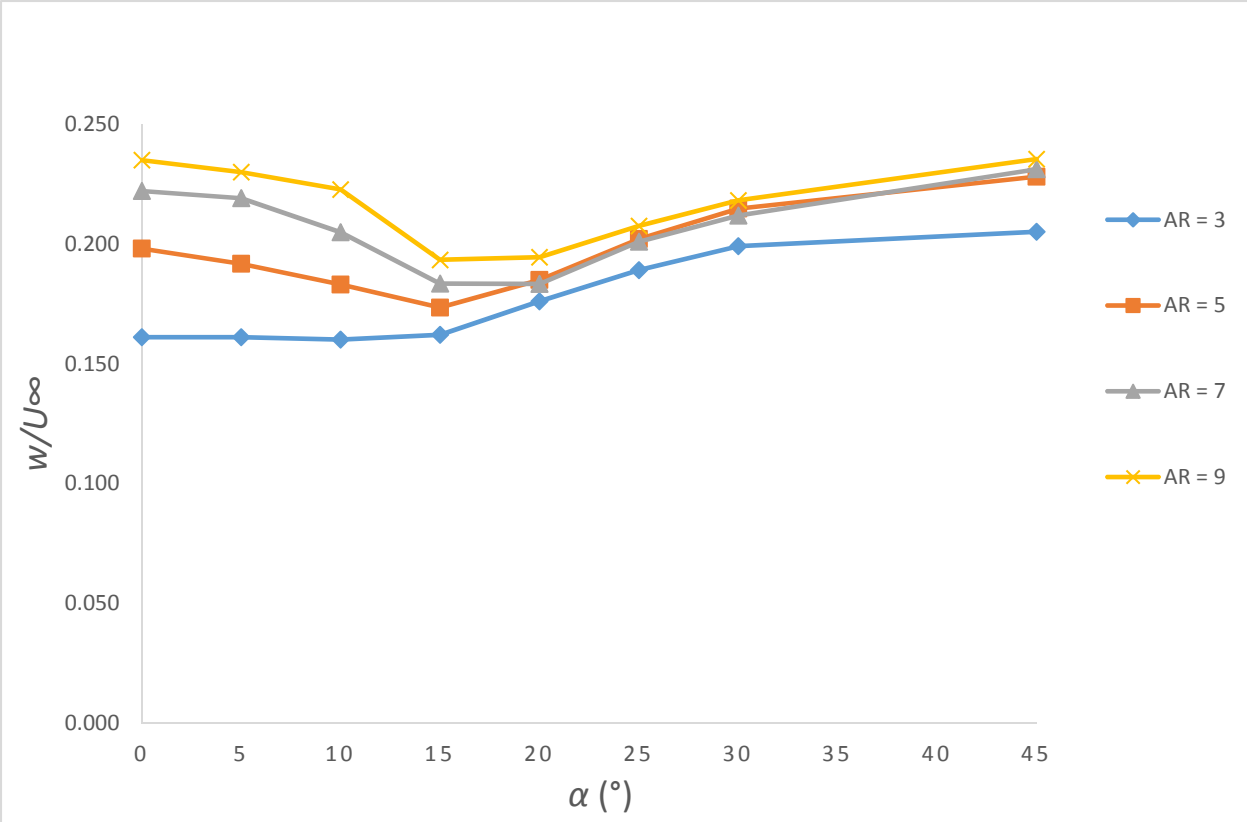

Figure 5.10: Absolute value of the wall-normal mean velocity (or maximum downwash velocity) in the wake of finite square prisms of AR = 3, 5, 7 and 9 at $x/D = 10$, for incidence angles ranging from $\alpha = 0°$ to 45°. Finite square prism data for AR = 3 are taken from Ogunremi and Sumner (2015a).

With the increase in incidence angle, the magnitude of (w/U_∞) reduces and reaches its minimum value at $\alpha = 15°$ (AR = 5, 7 and 9) and then it increases and reaches a maximum value at $\alpha = 45°$. Thus, the minimum downwash velocity is attained for a prism configuration of $\alpha = 15°$ and the maximum downwash velocity is at $\alpha = 45°$. For the AR = 3 prism, the minimum downwash velocity is obtained at $\alpha = 10°$. The different behaviour for AR = 3 prism can be attributed to the fact that it lies below critical aspect ratio for the present experimental conditions.

Time-averaged wall-normal velocity fields (w/U_∞) in the cross-stream (y-z) plane of the finite square prism of AR = 9, for various incidence angles, are shown as contour plots in Figure 5.11. For all incidence angles, there exists strong downwash, which originates from the prism's free end and descends into the wake. Unlike finite circular cylinders, negligible upwash velocity is seen at $x/D = 10$ at all incidence angles. At $\alpha = 0°$ (Figure 5.11 a), there exists a strong downwash velocity on the wake centerline.

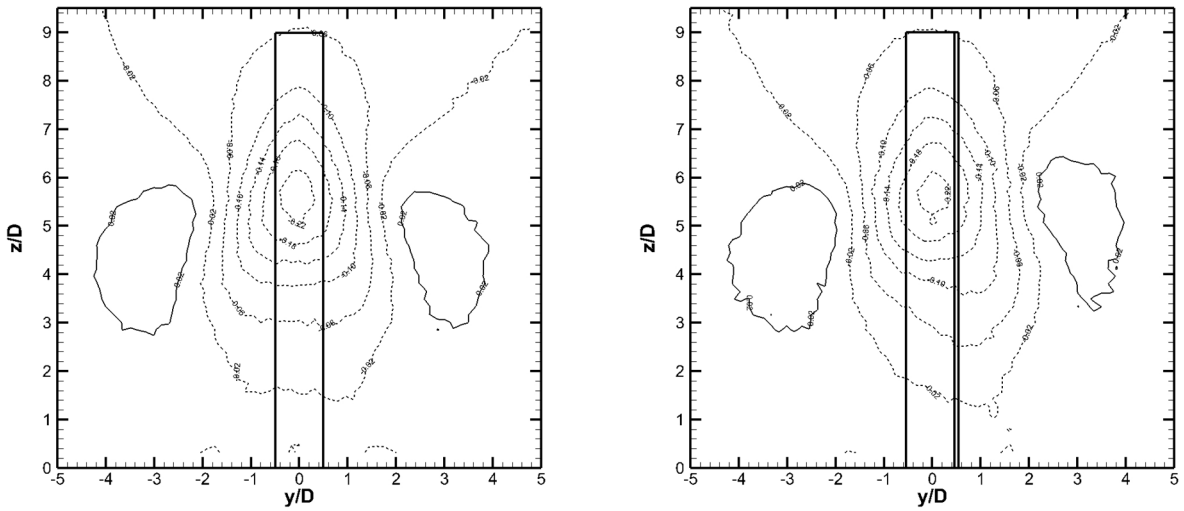

(a) $\alpha = 0°$ (b) $\alpha = 5°$

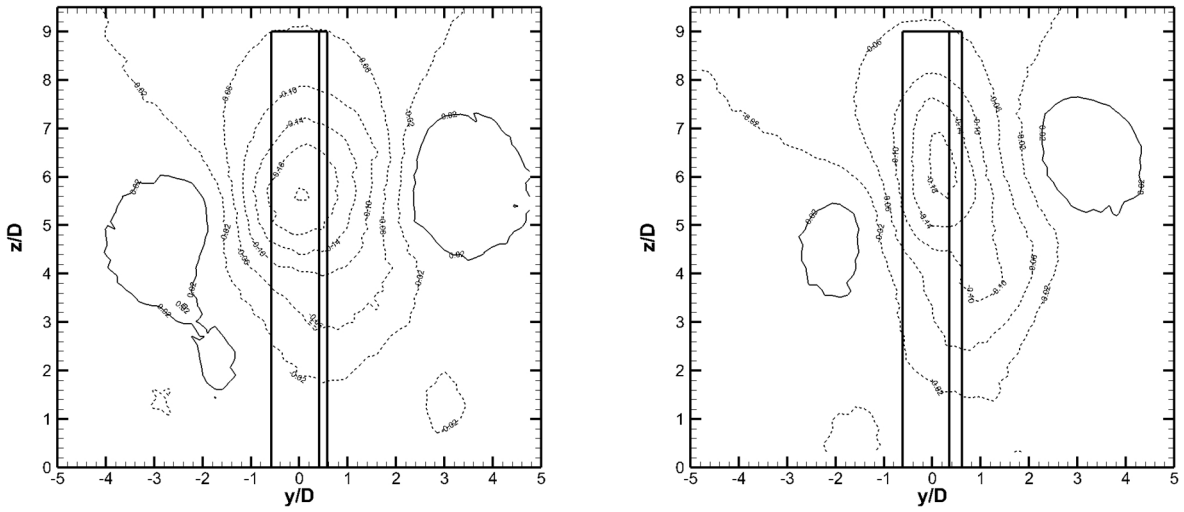

(c) $\alpha = 10°$ (d) $\alpha = 15°$

Figure 5.11: Wall-normal mean velocity contours in the wake of the square prism of AR = 9 at x/D = 10, for incidence angles ranging from α = 0° to 45°. Contour increment of w/U_∞ = 0.04. Dashed lines represent negative (downward) velocity. (Figure continues on the following page.)

When the incidence angle is increased to α = 5° (Figure 5.11b), a slight asymmetry in the wake is formed with the downwash directed slightly towards the thicker side of the wake (+y direction). With a further increase in incidence angle, the asymmetry increases further reaching the maximum at α = 15° and α = 20° (Figures 5.11d,e). Beyond α = 25°, the wake reduces its

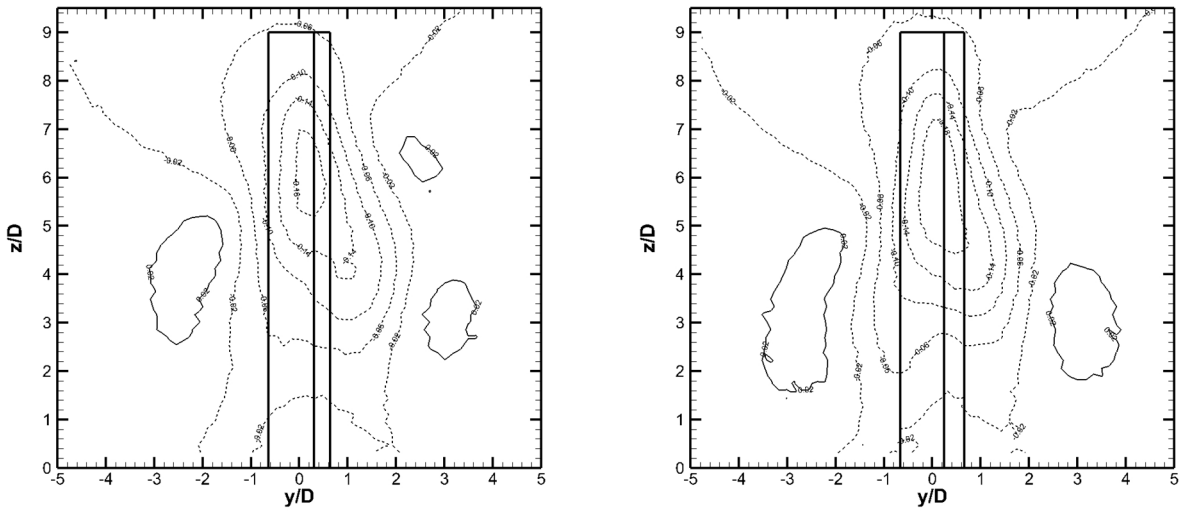

(e) $\alpha = 20°$

(f) $\alpha = 25°$

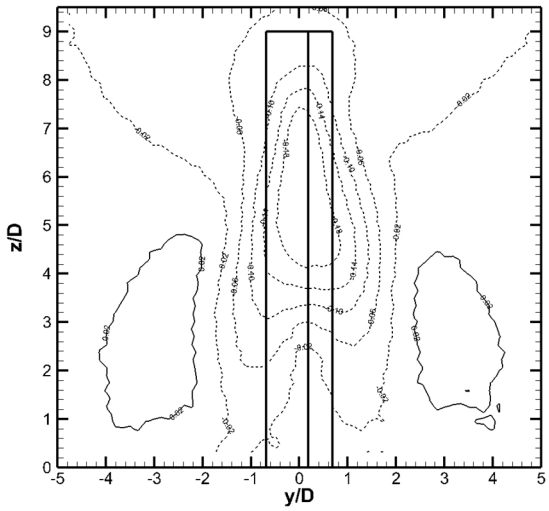

(g) $\alpha = 30°$

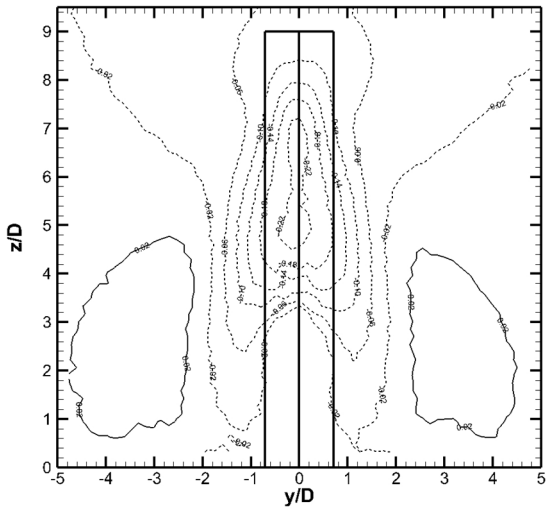

(h) $\alpha = 45°$

Figure 5.11 continued.

asymmetry and regains a symmetrical pattern at α = 45° (Figure 5.11h). Also, the downwash reaches towards the ground plane at α = 45° (Figure 5.11 h).

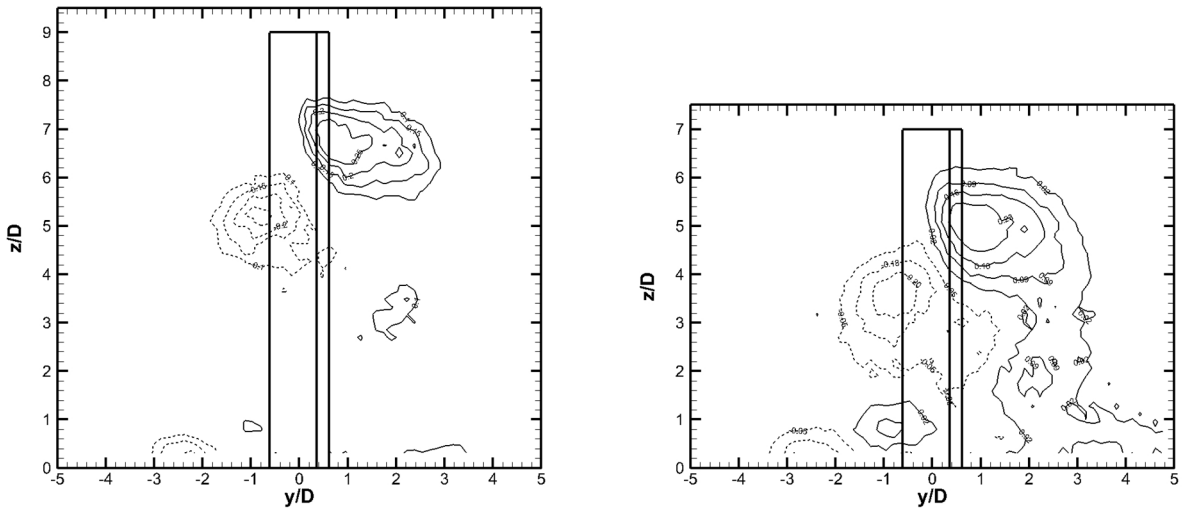

(a) AR = 9, α = 15° (b) AR = 7, α = 15°

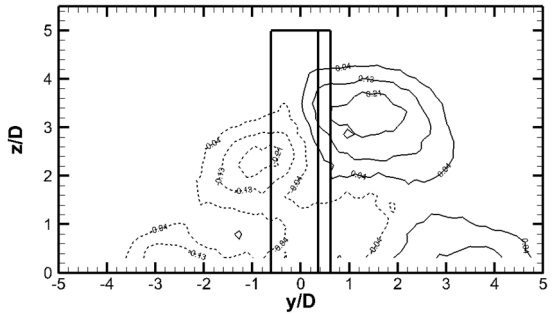

(c) AR = 5, α = 15°

Figure 5.12: Time-averaged streamwise vorticity field (contours of $\omega_x D/U_\infty$) in the cross-stream vertical plane at x/D = 10 for finite square prisms of (a) AR = 9, (b) AR = 7 and (c) AR = 5, at α = 15° (close to the critical incidence angle). Solid lines represent positive (CCW) vorticity, dashed lines represent negative (CW) vorticity.

5.4 Finite Square Prisms of AR = 7 and AR = 5

The effect of prism orientation on the flow over a finite square prism was also studied for prisms of aspect ratios AR = 7 and AR = 5. Similar to the prism of AR = 9, which has been discussed in detail in the previous sections, the incidence angle of the prisms of AR = 7 and AR = 5 was also varied from α = 0° to α = 45°. The behaviour of these two prisms was similar to that of AR = 9, with a critical incidence angle of around α = 15°. Given the similarity of the flow fields, only some limited comparisons are made here.

Figure 5.12 shows the time-averaged streamwise vorticity field at an incidence angle of α = 15°, at x/D = 10, for the three finite prisms (of AR = 9, 7 and 5). This orientation is close to the critical incidence angle for these prisms. For all three aspect ratios, the counter-clockwise tip vortex (on the +y side of the wake) shifts to a position higher than that of the clockwise tip vortex (on the –y side of the wake), and the mean wake has its highest asymmetry. The horseshoe vortices appear to be evident for all three prisms. For the prism of AR = 7 (Figure 5.12b), however, there is a second, weak concentration of counterclockwise vorticity on the +y side of the wake (centred at an elevation of approximately z/D = 2), that appears to link the tip vortex and the horseshoe vortex. For the prism of AR = 5 (Figure 5.12c), there is instead a concentration of clockwise vorticity on the wake centreline just above then ground plane, which is contiguous with the clockwise tip vortex on the –y side of the wake.

Figure 5.13 shows the time-averaged streamwise vorticity field for the finite square prisms of AR = 9, 7 and 5 at the α = 45° orientation, where flow symmetry is once again attained. The streamwise vortex structures are now more oval and angular in shape. The vorticity concentrations that denote the tip vortices for AR = 9 and 7 (Figures 5.13a,b) seem to show two distinct structures with the same sense of rotation. At lower aspect ratios of AR = 7 and AR = 5 (Figures 5.13b,c), the tip vortices merge with the trailing arms of the horseshoe vortex.

Figures 5.14 and 5.15 show the time-averaged velocity vector field for the finite square prisms of AR = 9, 7 and 5 at α = 15° and α = 45°, in the vertical x-z plane. A strong downwash is seen for all prisms. For both orientations, the recirculation zone shortens as the aspect ratio is reduced. It was clearly identified in the present experiments that the maximum length of recirculation zone (L_{max}/D) appears to reach its minimum value near α = 15° configuration (Figure 5.14), which is close to the critical incidence angle. The maximum length of the recirculation zone was found to occur at the α = 45° orientation (Figure 5.15).

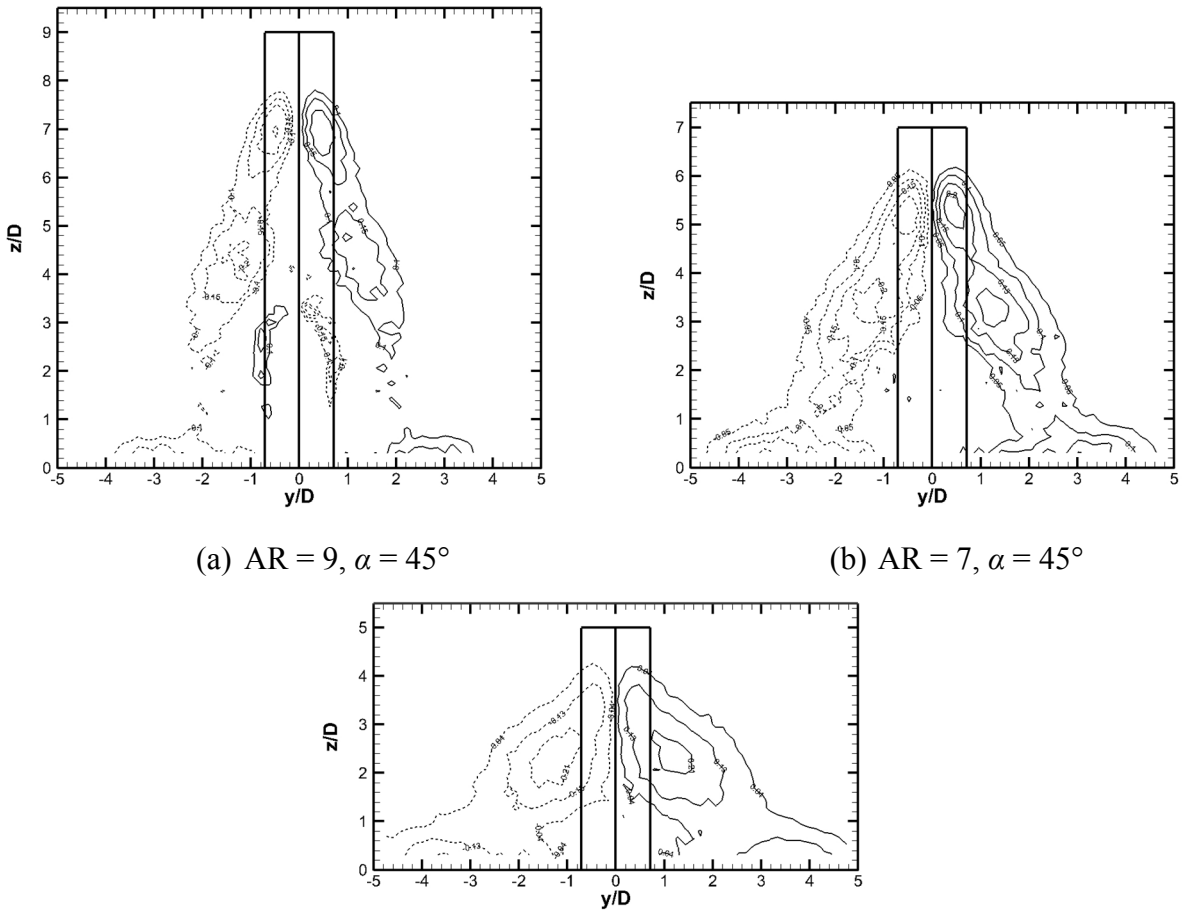

(a) AR = 9, α = 45°

(b) AR = 7, α = 45°

(c) AR = 5, α = 45°

Figure 5.13: Time-averaged streamwise vorticity field (contours of $\omega_x D/U_\infty$) in the cross-stream vertical plane at x/D = 10 for finite square prisms of (a) AR = 9, (b) AR = 7 and (c) AR = 5, at α = 45°. Solid lines represent positive (CCW) vorticity, dashed lines represent negative (CW) vorticity.

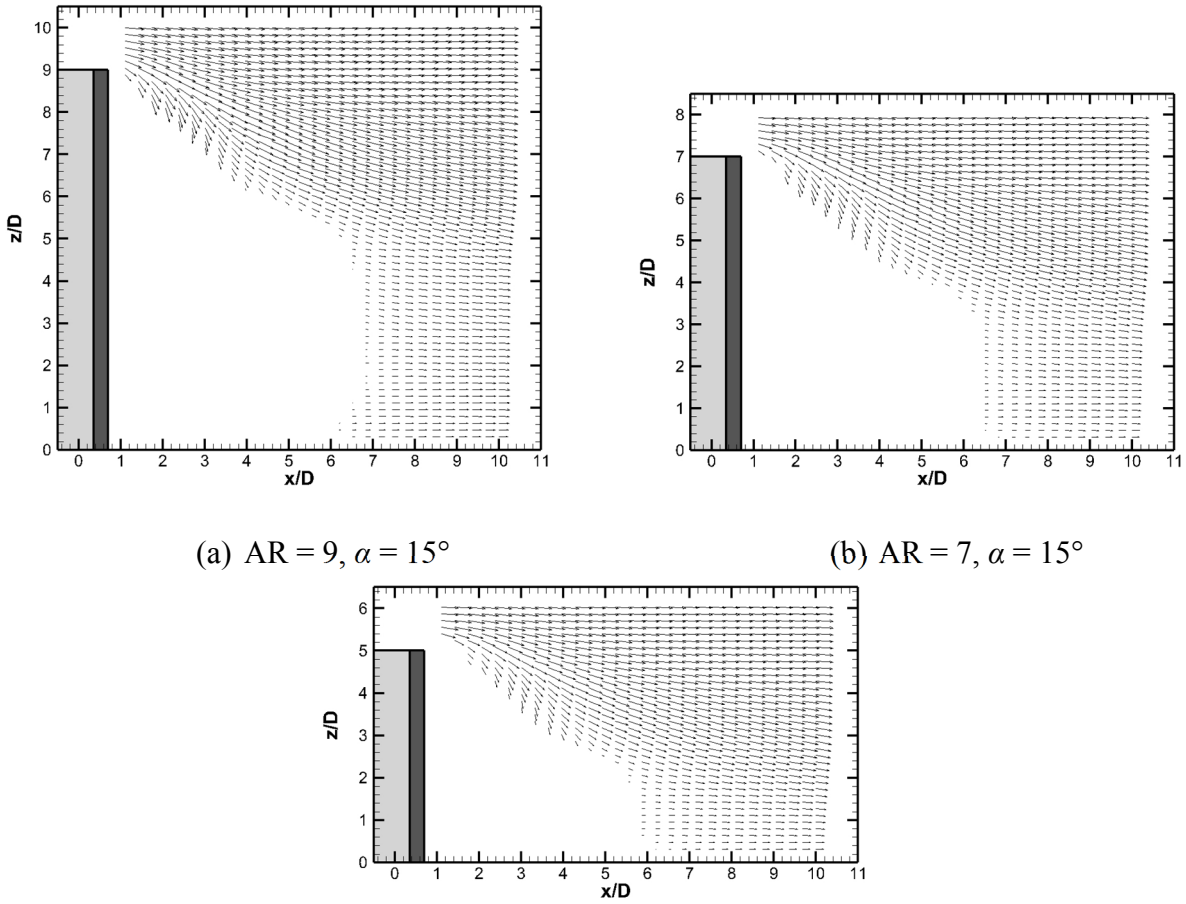

(a) AR = 9, α = 15° (b) AR = 7, α = 15°

(c) AR = 5, α = 15°

Figure 5.14: Time-averaged velocity field (velocity components u and w) along the wind tunnel centreline (y/D = 0) for finite square prisms of (a) AR = 9, (b) AR = 7 and (c) AR = 5 at α = 15° (close to the critical incidence angle).

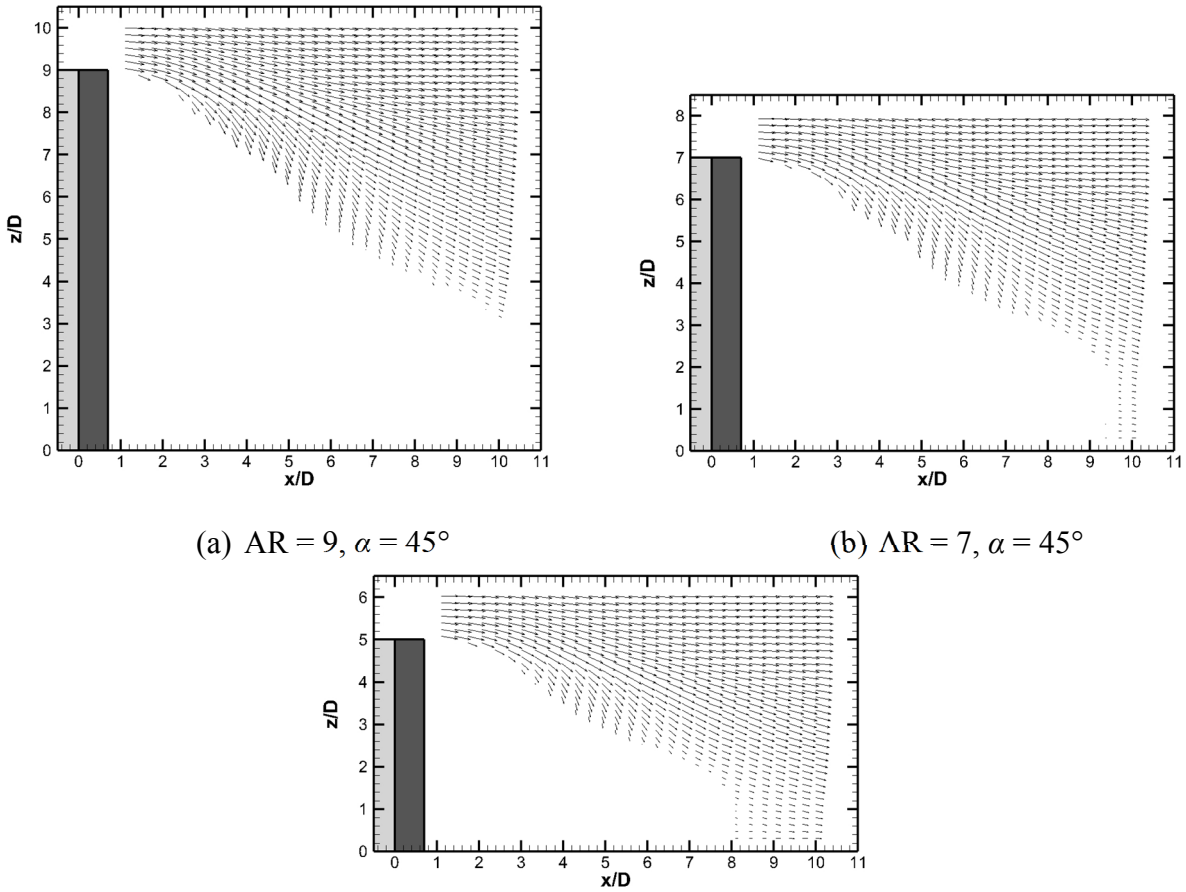

(a) AR = 9, α = 45°

(b) AR = 7, α = 45°

(c) AR = 5, α = 45°

Figure 5.15: Time-averaged velocity field (velocity components *u* and *w*) along the wind tunnel centreline (y/D = 0) for finite square prisms of (a) AR = 9, (b) AR = 7 and (c) AR = 5 at α = 45°.

CHAPTER 6. CONCLUSIONS AND RECOMMENDATIONS

6.1 Conclusions

The aim of the present research was to study the effect of incidence angle and aspect ratio on the mean wake of surface-mounted finite-height square prisms, including the mean recirculation zone behind the prism and the mean streamwise vortex structures. For the present study, the flow around finite square prisms of AR = 9, 7 and 5 has been studied for a range of incidence angles from $\alpha = 0°$ to 45°. The Reynolds number, based on the width of the prism, was $Re = 3.7\times10^4$, and the relative thickness of the boundary layer on the ground plane, at the location of the prism, was $\delta/D = 1.5$. Time-averaged velocity measurements in the wake were taken using a seven-hole pressure probe. The data obtained were compared with the earlier results obtained by Ogunremi and Sumner (2015a) for a finite square prism of AR = 3 (for $Re = 3.7\times10^4$ and $\delta/D = 1.5$), McClean and Sumner (2014) for finite square prisms of AR = 11, 9, 7, 5, and 3 (for $Re = 7.3\times10^4$ and $\delta/D = 1.5$), and Sumner et al. (2004) for a finite cylinder (for $Re = 6\times10^4$ and $\delta/D = 2.6$). The wake measurements were carried out within two vertical planes: a vertical x-z plane located on the centerline of the wind tunnel ($y/D = 0$), and a vertical y-z plane located at $x/D = 10$.

Based on the research results, and considering the objectives of the research (Section 1.2), several conclusions were obtained.

The first objective of the research was to measure the mean velocity field in vertical planes (normal to and parallel to the main flow direction) in the wake of finite square prisms of aspect ratios AR = 9, 7 and 5, for incidence angles from $\alpha = 0°$ to 45°. Using a seven-hole pressure probe as the measurement instrument, this objective was completed, with the results presented in Chapters 4 and 5. The research presented in the thesis was one of the first systematic studies of the mean wake behind a surface-mounted finite square prism where the combined effects of aspect ratio and incidence angle were considered. As such, it contributes new information on the flow around surface-mounted finite-height bluff bodies.

The second objective of the research was to investigate the effects of incidence angle (α) and aspect ratio (AR) on the mean wake, including the mean recirculation zone and the mean streamwise vortex structures. Several conclusions arise from this objective and research:

- With an increase in aspect ratio, the maximum recirculation zone length of a square prism increases from 4.6D (AR = 3) to 8.4D (AR = 9) at $\alpha = 0°$. But it is worth mentioning that the magnitude of increase with aspect ratio reduces with a move to higher aspect ratio, i.e. 1.7D between AR = 3 and 5, 1.2D between AR = 5 and 7 and 0.9D between AR = 7 and 9. The maximum magnitude between AR = 3 and 5 is due to the fact that the critical aspect ratio of the prism lies between 3 and 5 for the present experimental conditions (McClean and Sumner, 2014; Ogunremi and Sumner, 2015a).
- A symmetric counter-rotating pair of streamwise vortices, representing the tip vortices, is seen in the upper part of the wake at $x/D = 10$ for all aspect ratios at an incidence angle of $\alpha = 0°$. The centres of the tip vortices are observed to be near the mid-height of the prism at $\alpha = 0°$. Thus, the location of the vortex centre is a function of the aspect ratio of the prism and is approximately equal to 0.56H.
- Smaller streamwise vorticity concentrations are seen at the outer edges of the wake close to the ground plane, which represent the trailing arms of the horseshoe vortex system originating upstream from the prism within the boundary layer. The centres of the horseshoe vortex pairs move closer towards the prism with the increase in aspect ratio from AR = 5 to 9.
- At $\alpha = 0°$, the maximum width of the wake increases with a reduction in AR, increasing from approximately 5.2D for AR = 9, to 6D for AR = 7, and to 6.8D for AR = 5.
- The length of the recirculation zone decreases when moving from the ground plane to the free end of the square prism. This indicates that the effect of downwash is maximum near the free end of the prism and reduces when moving towards the ground plane.
- For the square prism of AR = 9, the velocity field shows stronger downwash behind the square prism and below the free end height compared to the prisms of AR = 7 and 5. The downwash weakens along the axis of the prism towards the ground plane and the remaining flow is directed towards the downstream direction.

- The streamwise velocity component $(u/U_\infty)_{min}$ in the wake region shows a maximum value for AR = 3 and a minimum value for AR = 9. This is consistent with published mean drag coefficient data.
- As α is varied from 0° to 45°, the mean wake shifts in the direction of rotation of the prism, opposite to the direction of the mean lift force, with the counterclockwise tip vortex moving higher above the ground plane while the clockwise tip vortex moves closer to the ground plane. The asymmetry in the mean wake is most pronounced at the critical incidence angle, which was between α = 10° and 15° in the experiments. When the prism is further rotated to α = 20° and higher, the asymmetry of the recirculating flow begins to diminish, until a symmetric arrangement of the tip vortex pair is once again established at α = 45°.
- The tip vortices gradually elongate towards the ground plane and for α = 25° to 45° and become linked to the vorticity associated with the horseshoe vortex arms.
- With the increase in incidence angle, the maximum length of the recirculation zone decreases initially and reaches a minimum value at critical incidence angle and then increases with increase in α and reaches maximum at α = 45°.
- The smallest value of the streamwise velocity component $(u/U_\infty)_{min}$ in the wake at x/D = 10 of the finite square prism decreases with aspect ratio for all incidence angles. With the increase in incidence angle, the magnitude of (w/U_∞) reduces and reaches its minimum value at α = 15° and then it increases and reaches a maximum value at α = 45°. Thus, the minimum downwash velocity is attained for a prism configuration of α = 15° and maximum downwash velocity at α = 45°. For the AR = 3 prism (Ogunremi and Sumner, 2015a), the minimum downwash velocity is obtained at α = 10°. The different behaviour for AR = 3 prism can be attributed to the fact that it lies below the critical aspect ratio for the present experimental conditions.

The third objective of the research was to compare the mean wake of a finite square prism with that of a finite cylinder, using finite-cylinder results from the literature. From the research results, it was concluded that:

- The maximum recirculation zone length for a finite square prism is much higher than that of a finite cylinder, for bodies of similar aspect ratio.

- The base vortex structures are nearly absent at $x/D = 10$ for the square prism. The base vortex structures are responsible for the upwash flow, and the present experiments clearly identify that there is no significant upwash for the finite square prism at $x/D = 10$. This contrasts with similar wake measurements for a finite cylinder, by Sumner et al. (2004), which showed the presence of the streamwise base vortices at $x/D = 10$ as well as upwash close to the ground plane.
- The trailing arms of the horseshoe vortices, which were identified in the wake of the finite square prisms at $x/D = 10$, were not seen in the finite cylinder data obtained by Sumner et al. (2004). The increased "bluffness" of the finite square prism, with the flat surfaces, sharp edges and well-defined separation points, is responsible for a larger and stronger horseshoe vortex system, compared to the finite cylinder.

The fourth objective of the research was to identify the mean wake flow pattern associated with the critical incidence angle of the finite square prism.

- The maximum asymmetry in the tip vortex pair coincides with the critical incidence angle for the prism, which lies between $\alpha = 10°$ and 15° (McClean and Sumner, 2014). Close to the critical incidence angle, between $\alpha = 10°$ and $\alpha = 15°$, the CCW tip vortex moves to its highest point above the ground plane, while the CW tip vortex moves towards the ground plane.
- The critical incidence angle, which was known to correspond to the minimum value of mean drag coefficient, maximum magnitude of the mean lift coefficient, and maximum value of the Strouhal number (McClean and Sumner, 2014), is also found to correspond with the smallest magnitude of the mean downwash velocity component (w/U_∞), the largest value of the minimum mean streamwise velocity component $(u/U_\infty)_{min}$, the maximum value of positive (counterclockwise) mean streamwise vorticity within the wake, and the minimum value of L_{max}/D.

6.2 Recommendations for Future Work

The present research was carried out to study the mean wake of a surface-mounted finite-height square prism and how it is influenced by changes in incidence angle and aspect ratio. However, only certain parameters are changed in the present research while others remained

unchanged throughout the experiments. For future work, the following recommendations should be taken into consideration:

- All the present experiments were carried out at a single boundary layer thickness of δ/D = 1.5. The effect of boundary layer thickness on the wake, especially for prisms at non-zero incidence angles, is still not well understood. Systematically varying the boundary layer thickness, while keeping other parameters constant, could reveal more details on the boundary layer effects for this class of bluff bodies.
- Measurements in the vertical planes on the centreline of the wind tunnel could not be made too close to the prism, to protect the probe from accidental damage, and to avoid regions of reversing flow where the probe could not be operated. A more efficient way to carry out measurements close to the prism, such as PIV, could be adopted in future. There have been few, if any, studies of the flow around surface-mounted finite-height prisms at non-zero incidence angles that have used the PIV technique.
- The present experiments were carried out at a single Reynolds number of Re = 3.7×10^4. Although Reynolds number effects for square prisms are relatively small compared to cylinders, conducting experiments at lower and higher Reynolds numbers could reveal some Reynolds number effects on the flow behaviour.
- For the current study, prisms of aspect ratio AR = 9, 7 and 5 were considered. The effect of incidence angle and aspect ratio on prisms of lower aspect ratio, such as AR < 3 or AR > 9, need to be studied, since there are relatively few studies in the literature. Some preliminary results were recently published for finite square prisms of AR = 1 and AR = 0.5, using similar experimental conditions as the present thesis research, which showed distinct wake behaviour as the incidence angle was changed (Sumner et al., 2016).
- Due to time limitations, the number of measurement planes and their locations had to be limited. The vertical x-z plane measurements were taken only on the wind tunnel centreline (y/D = 0). Considering more vertical planes on either side of the wake centreline could reveal more details about the flow. The vertical cross-stream y-z plane measurements were taken only at x/D =10. Additional measurement planes at different values of x/D would reveal the streamwise development of the mean wake. Some measurements were also made in a horizontal (x-y) plane at the mid-height position (z/H = 0.5) for selected aspect ratios and incidence angles. However, the results did not provide too much information,

and due to time limitations they were not continued or reported in the thesis. Nonetheless, additional horizontal planes could be considered, perhaps closer to the free end or upper part of the wake.

- To better understand what happens at the critical incidence angle, the incidence angle settings could be more refined, i.e. taken using smaller increments of α, in the range of $10° < \alpha < 30°$).

REFERENCES

Adaramola, M.S., Sumner, D., Bergstrom, D.J., 2010. Effect of velocity ratio on the streamwise vortex structures in the wake of a stack. Journal of Fluids and Structures 26, 1-18.

Baines, W.D., 1963. Wind effects on buildings and structures. Proceedings of the International Conference on Wind Effects on Buildings and Structures, June 26-28, 1963, National Physical Laboratory, Teddington, Middlesex, UK.

Barlow, J B., Rae, W.H., Jr., Pope, A., 1999. Low-Speed Wind Tunnel Testing, 3rd edition, New York: Wiley.

Bourgeois, J.A., Sattari, P., Martinuzzi, R.J., 2011. Alternate half-loop shedding in the turbulent wake of a finite surface-mounted square cylinder with a thin boundary layer. Physics of Fluids 23, 095101 (15 pp.).

Bourgeois, J.A., Sattari, P., Martinuzzi, R.J., 2012. Coherent vortical and straining structures in the finite wall-mounted square cylinder wake. International Journal of Heat and Fluid Flow 35, 130-140.

Bryer, D.W., Pankhurst, R.C., 1971. Pressure-probe methods for determining wind speed and flow direction. London, UK: Her Majesty's Stationery Office.

Datametrics, 1982a. Instruction Manual. Type 600 Barocel Pressure Sensor. Datametrics-Dresser Industries, Inc., Wilmington, MA, USA.

Datametrics, 1982b. Instruction Manual. Type 590 Barocel Pressure Sensor. Datametrics-Dresser Industries, Inc., Wilmington, MA, USA.

Dutta, S., Muralidhar, K., Panigrahi, P.K., 2003. Influence of the orientation of a square cylinder on the wake properties. Experiments in Fluids 34, 16-23.

Dutta, S., Panigrahi, P.K., Muralidhar, K., 2004. "Effect of orientation on the wake of a square cylinder at low Reynolds numbers. Indian Journal of Engineering & Materials Sciences 11, 447-459.

Dutta, S., Panigrahi, P.K., Muralidhar, K., 2008. Experimental investigation of flow past a square cylinder at an angle of incidence. Journal of Engineering Mechanics 134, 788-803.

Einian, M., Bergstrom, D.J., Sumner, D., 2009. Large eddy simulation of flow over a finite square cylinder. 6th International Symposium on Turbulence, Heat and Mass Transfer (THMT09), September 14-18, 2009, Rome, Italy.

Einian, M., Bergstrom, D. J., Sumner, D., 2010. Numerical simulation of the flow around a surface-mounted finite square cylinder. 7th International Symposium on Fluid-Structure Interactions, Flow-Sound Interactions, and Flow-Induced Vibration and Noise: ASME FEDSM-ICNNM, Volume 3, Parts A and B, FEDSM-ICNMM Paper 2010-30394, Montreal, Quebec, Canada, 1–5 Aug. 2010, pp. 103-110.

Einian, M., Bergstrom, D. J., Sumner, D., 2011. The effect of subgrid-scale model on prediction of flow around a surface-mounted finite square cylinder. Journal of Physics: Conference Series, Vol. 318, No. 4, 2011, Paper 042027.

El Hassan, M, Bourgeois, J., Martinuzzi, R., 2015. Boundary layer effect on the vortex shedding of wall‐mounted rectangular cylinder. Experiments in Fluids 56: 33 (19 pp.)

Figliola, R.S., Beasley, D.E., 2011. Theory and design for mechanical measurements, 5th edition. Hoboken, NJ; John Wiley & Sons, Inc.

Holmes, J.D., 2007. Wind Loading of Structures, 2nd Edition. London: Taylor & Francis.

Hosseini, Z., Bourgeois, J.A., Martinuzzi, R.J., 2013. Large-scale structures in dipole and quadrupole wakes of a wall-mounted finite rectangular cylinder. Experiments in Fluids 54, 1595, 16 pp.

Hu, J.C., Zhou, Y., Dalton, C., 2006. Effects of corner radius on the near wake of a square prism. Experiments in Fluids 40, 106-118.

Huang, R.F., Lin, B.H., Yen, S.C., 2010. Time-averaged topological flow patterns and their influence on vortex shedding of a square cylinder in crossflow at incidence. Journal of Fluids and Structures 26, 406-429.

Igarashi, T., 1984. Characteristics of the flow around a square prism. Bulletin of the JSME 27, 1858-1865.

Knisely, C.W., 1990. Strouhal numbers of rectangular cylinders at incidence: a review and new data. Journal of Fluids and Structures 4, 371-393.

Kurtulus, D.F., Scarano, F., David, L., 2007. Unsteady forces estimation on a square cylinder by TR-PIV. Experiments in Fluids 42, 185-96.

Lee, S., 1998. Numerical study of wake structure behind a square cylinder at high Reynolds number. Wind and Structures 1, 127-144.

Lindquist, C., Vieira, E.D.R., 2010. Flow around square cylinders in several attack angles. Proceedings of ENCIT 2010: 13th Brazilian Congress of Thermal Sciences and Engineering. December 5-10, 2010, Uberlandia, MG, Brazil.

Luo, S.C., Chew, Y.T., Ng, Y.T., 2003. Characteristics of square cylinder wake transition flows. Physics of Fluids 15, 2549-2559.

Lyn, D.A., Einav, S., Rodi, W., Park, J.H., 1995. A laser-Doppler velocimetry study of ensemble-averaged characteristics of the turbulent near wake of a square cylinder. Journal of Fluid Mechanics 304, 285-319.

McClean, J.F., Sumner, D., 2014. An experimental investigation of aspect ratio and incidence angle effects for the flow around surface-mounted finite-height square prisms. Transactions of the ASME: Journal of Fluids Engineering 136, 1-10.

Norberg, C., 1993. Flow around rectangular cylinders: pressure forces and wake frequencies. Journal of Wind Engineering and Industrial Aerodynamics 49, 187-196.

Obasaju, E.D., 1979. On the effects of end plates on the mean forces on square sectional cylinders. Journal of Industrial Aerodynamics 5, 179-186.

Obasaju, E.D., 1983. An investigation of the effects of incidence on the flow around a square section cylinder. The Aeronautical Quarterly 34, 243-259.

Ogunremi, A., Sumner, D., 2015a. On the effects of incidence angle on the mean wake of a surface-mounted finite-height square prism. ASME-JSME-KSME Joint Fluids Engineering Conference 2015 (AJK2015-FED), July 26-31, 2015, Seoul, Korea, Paper. No. AJK2015-15011.

Ogunremi, A.R., Sumner, D., 2015b. The effect of a splitter plate on the flow around a finite prism. Journal of Fluids and Structures 59, 1-21.

Oka, S., Ishihara, T., 2009. Numerical study of aerodynamic characteristics of a square prism in a uniform flow. Journal of Wind Engineering and Industrial Aerodynamics 97, 548-559.

Okuda, Y., Taniike, Y., 1993. Conical vortices over side face of a three-dimensional square prism. Journal of Wind Engineering and Industrial Aerodynamics 50, 163-172.

Ozgoren, M. 2006. Flow structure in the downstream of square and circular cylinders," Flow Measurement and Instrumentation 17, 225-235.

Rostamy, N., 2012, Fundamental studies of the wake structure for surface-mounted finite-height cylinders and prisms. Ph.D. Thesis, Department of Mechanical Engineering, University of Saskatchewan.

Rostamy, N., McClean, J.F., Sumner, D., Bergstrom, D.J., Bugg, J.D., 2012. Local flow field of a surface-mounted finite square prism. 7th International Colloquium on Bluff Body Aerodynamics and Applications (BBAA7), Shanghai, China, September 2-6, 2012.

Saha, A.K., Muralidhar, K., Biswas, C. 2000. Experimental study of flow past a square cylinder at high Reynolds numbers. Experiments in Fluids 29, 553-563.

Sakamoto, H., Arie, M., 1983. Vortex shedding from a rectangular prism and a circular cylinder placed vertically in a turbulent boundary layer. Journal of Fluid Mechanics 126, 147-165.

Sakamoto, H., 1985. Aerodynamic forces acting on a rectangular prism placed vertically in a turbulent boundary layer. Journal of Wind Engineering and Industrial Aerodynamics 18, 131-151.

Sakamoto, H., Oiwake, S., 1984. Fluctuating forces on a rectangular prism and a circular cylinder placed vertically in a turbulent boundary layer. Transactions of the ASME: Journal of Fluids Engineering 106, 160-166.

Sarode, R. S., Gai, S. L., Ramesh, C.K., 1981. Flow around circular and square-section models of finite height in a turbulent shear flow. Journal of Wind Engineering and Industrial Aerodynamics 8, 223-230.

Sattari, P., Bourgeois, J.A., Martinuzzi, R.J., 2010. Turbulent wake of surface-mounted finite aspect ratio bluff bodies: effect of aspect ratio and cross section shape. ASME 3rd Joint US-European Fluids Engineering Division Summer Meeting, Montreal, Canada, Aug. 1-5, 2010, ASME Paper No. FEDSM-ICNMM2010-30811.

Sattari, P., Bourgeois, J.A., Martinuzzi, R.J., 2012. On the vortex dynamics in the wake of a finite surface-mounted square cylinder. Experiments in Fluids 52, 1149-1167.

Sau, A., Hwang, R.R., Sheu, T.W.H., Yang, W.C., 2003. Interaction of trailing vortices in the wake of a wall-mounted rectangular cylinder. Physical Review E 68, 1-15.

Scanivalve, 2014. Model ZOC17 Temperature Compensated Electronic Pressure Scanning Module, Data Sheet No. G447. Scanivalve Corporation, Liberty Lake, WA, USA.

Sohankar, A., Norberg, C., Davidson, L., 1997. Numerical simulation of unsteady low Reynolds number flow around rectangular cylinders at incidence. Journal of Wind Engineering and Industrial Aerodynamics 69-71, 189-201.

Sohankar, A., C. Norberg, L. Davisdon, 1998. Low-Reynolds number flow around a square cylinder at incidence; Study of blockage, onset of vortex shedding and outlet boundary condition. International Journal for Numerical Methods in Fluids, 26, pp. 39-56.

Sumner, D., 2002. A comparison of data-reduction methods for a seven-hole probe. Transactions of the ASME: Journal of Fluids Engineering 124, 523-527.

Sumner, D., Heseltine, J.L., Dansereau, O.J.P., 2004. Wake structure of a finite circular cylinder of small aspect ratio. Experiments in Fluids 37, 720-730.

Sumner, D., Unnikrishnan, S., Teng, M., Beitel, A., Das, A., Fulton, M., 2016. The mean wake of low-aspect-ratio surface-mounted finite-height square prisms and the effects of incidence angle. 8th International Colloquium on Bluff Body Aerodynamics and Applications, June 7-11, 2016, Boston, USA, Paper No. 065, 10 pp.

van Oudheusden, B.W., Scarano, F., Hinsberg, N.P., Roosenboom, E.W.M., 2008. Quantitative visualization of the flow around a square-section cylinder at incidence. Experiments in Fluids 96, 913-922.

van Oudheusden, B.W., Scarano, F., van Hinsberg, N.P., Watt, D.W., 2005. Phase-resolved characterization of vortex shedding in the near wake of a square-section cylinder at incidence. Experiments in Fluids 39, 86-98.

Wang, H.F., Cao, H.L., Zhou, Y., 2014. POD analysis of a finite-length cylinder near wake. Experiments in Fluids 55, 1790 (15 pp.).

Wang, H.F., Zhou, Y., 2009. The finite-length square cylinder near wake. Journal of Fluid Mechanics 638, 453-490.

White, F.M., 2003. Fluid Mechanics, 5th Edition, McGraw-Hill, New York.

Yen, S.C., Yang, C.W., 2011. Flow patterns and vortex shedding behavior behind a square cylinder. Journal of Wind Engineering and Industrial Aerodynamics 99, 868-878.

Yen, S.C., Yang, C.W., 2012. Characteristics flow field behind a square-cylinder using upstream mesh fences. Transactions of the ASME: Journal of Fluids Engineering 134, 1-9.

APPENDIX. PERMISSIONS

ELSEVIER LICENSE
TERMS AND CONDITIONS

Aug 18, 2016

This Agreement between Sanjith Unnikrishnan ("You") and Elsevier ("Elsevier") consists of your license details and the terms and conditions provided by Elsevier and Copyright Clearance Center.

License Number	3932100919736
License date	Aug 18, 2016
Licensed Content Publisher	Elsevier
Licensed Content Publication	Journal of Wind Engineering and Industrial Aerodynamics
Licensed Content Title	Numerical study of aerodynamic characteristics of a square prism in a uniform flow
Licensed Content Author	Shinichi Oka,Takeshi Ishihara
Licensed Content Date	December 2009
Licensed Content Volume Number	97
Licensed Content Issue Number	11-12
Licensed Content Pages	12
Start Page	548
End Page	559
Type of Use	reuse in a thesis/dissertation
Portion	figures/tables/illustrations
Number of figures/tables/illustrations	1
Format	both print and electronic
Are you the author of this Elsevier article?	No
Will you be translating?	No

Order reference number	
Original figure numbers	Figure 6
Title of your thesis/dissertation	An experimental investigation of aspect ratio and incidence angle effects on the mean wake of a surface-mounted finite-height square prism
Expected completion date	Aug 2016
Estimated size (number of pages)	98
Elsevier VAT number	GB 494 6272 12
Requestor Location	Sanjith Unnikrishnan University of Saskatchewan Department of Mechanical Engineering 57 Campus Drive Saskatoon, SK S7N 5A9 Canada Attn: Sanjith Unnikrishnan
Total	0.00 CAD

ELSEVIER LICENSE
TERMS AND CONDITIONS

Aug 18, 2016

This Agreement between Sanjith Unnikrishnan ("You") and Elsevier ("Elsevier") consists of your license details and the terms and conditions provided by Elsevier and Copyright Clearance Center.

License Number	3932101357717
License date	Aug 18, 2016
Licensed Content Publisher	Elsevier
Licensed Content Publication	Journal of Fluids and Structures
Licensed Content Title	Time-averaged topological flow patterns and their influence on vortex shedding of a square cylinder in crossflow at incidence
Licensed Content Author	R.F. Huang,B.H. Lin,S.C. Yen
Licensed Content Date	April 2010
Licensed Content Volume Number	26
Licensed Content Issue Number	3
Licensed Content Pages	24
Start Page	406
End Page	429
Type of Use	reuse in a thesis/dissertation
Intended publisher of new work	other
Portion	figures/tables/illustrations
Number of figures/tables/illustrations	2
Format	both print and electronic
Are you the author of this Elsevier article?	No
Will you be translating?	No

Order reference number	
Original figure numbers	Figures 9 and 12
Title of your thesis/dissertation	An experimental investigation of aspect ratio and incidence angle effects on the mean wake of a surface-mounted finite-height square prism
Expected completion date	Aug 2016
Estimated size (number of pages)	98
Elsevier VAT number	GB 494 6272 12
Requestor Location	Sanjith Unnikrishnan University of Saskatchewan Department of Mechanical Engineering 57 Campus Drive Saskatoon, SK S7N 5A9 Canada Attn: Sanjith Unnikrishnan
Total	0.00 USD

AIP PUBLISHING LLC LICENSE
TERMS AND CONDITIONS

Aug 18, 2016

This Agreement between Sanjith Unnikrishnan ("You") and AIP Publishing LLC ("AIP Publishing LLC") consists of your license details and the terms and conditions provided by AIP Publishing LLC and Copyright Clearance Center.

License Number	3932110677271
License date	Aug 18, 2016
Licensed Content Publisher	AIP Publishing LLC
Licensed Content Publication	Physics of Fluids
Licensed Content Title	Alternating half-loop shedding in the turbulent wake of a finite surface-mounted square cylinder with a thin boundary layer
Licensed Content Author	J. A. Bourgeois,P. Sattari,R. J. Martinuzzi
Licensed Content Date	Sep 6, 2011
Licensed Content Volume Number	23
Licensed Content Issue Number	9
Type of Use	Thesis/Dissertation
Requestor type	Student
Format	Print and electronic
Portion	Figure/Table
Number of figures/tables	3
Title of your thesis / dissertation	An experimental investigation of aspect ratio and incidence angle effects on the mean wake of a surface-mounted finite-height square prism
Expected completion date	Aug 2016
Estimated size (number of pages)	98

Requestor Location	Sanjith Unnikrishnan University of Saskatchewan Department of Mechanical Engineering 57 Campus Drive Saskatoon, SK S7N 5A9 Canada Attn: Sanjith Unnikrishnan
Billing Type	Invoice
Billing Address	Sanjith Unnikrishnan University of Saskatchewan Department of Mechanical Engineering 57 Campus Drive Saskatoon, SK S7N 5A9 Canada Attn: Sanjith Unnikrishnan
Total	0.00 USD

Permissions Requests

If you would like to reproduce or translate a chapter, journal article, text extract, figures or audio extract from a Cambridge publication, you will need to submit a 'Permissions Request Form'.

Cambridge University Press grants permission freely for the reproduction in another work of a short prose extract (less than 400 words), a single figure or a single table in which it holds rights (see the important caveat in the Notes below). In such cases a request for permission need not be submitted, but the reproduced material must be accompanied by a full citation of the original source.

Note also that Cambridge University Press may not be able to grant permission for the use of all the material it publishes. In particular, illustrations, tables, poetry or other extensive quotations included in Cambridge publications may have been reproduced by Cambridge with the permission of another rights holder. Always check the caption or citation to ensure that Cambridge is the rights holder before proceeding.

When submitting your form, please select the appropriate office:

CAMBRIDGE

All requests from publishers, institutions or users based worldwide, excluding USA, Canada, Mexico, Australia and New Zealand.

NEW YORK

All requests from publishers, institutions or users based in the USA, Canada or Mexico.

MELBOURNE

All requests from publishers, institutions or users based in Australia or New Zealand.